DIRECT THREE DIMENSIONAL OBSERVATION OF THE MICROSTRUCTURE AND CHEMISTRY OF C_3S HYDRATION

By

QINANG HU

Bachelor of Science
China University of Mining and Technology (Beijing)
Beijing
2009

Master of Science
Oklahoma State University
Stillwater, Oklahoma
2011

Submitted to the Faculty of the
Graduate College of the
Oklahoma State University
in partial fulfillment of
the requirements for
the Degree of
DOCTOR OF PHILOSOPHY
December, 2015

DIRECT THREE DIMENSIONAL OBSERVATION OF THE MICROSTRUCTURE AND CHEMISTRY OF C_3S HYDRATION

Dissertation Approved:

Matthew Tyler Ley

Bruce Russell

Julie Hartell

Jay Hanan

ACKNOWLEDGEMENTS

I would like to thank parents, Pan Jing and Hu Tie, for they could let me go and leave home for ten years since I started my undergraduate in Beijing. I would like to thank my uncle Li Zhaofeng and my aunt Pan Qing for their help and inspiration to make my study in the U.S. finally happen. I would also like to thank Plato and Socrates for their wisdoms from two thousand years ago that enlighten me to study engineering and science. I would like to thank Dr. Tyler Ley for giving my first opportunity to work with him. The knowledge I have learned during these years are own to him. His passion and dedication set an example for me to always want to try harder and keep making things better. I will be forever grateful to you. I would like to Dr. Jay Hanan for teaching me X-ray microscopies, XRD and Micro-CT, which turn out to be the starting point of my PhD research. I would like to thank Dr. Bruce Russell for sharing his professional knowledge, which I always admire. I would also like to thank Dr. Julie Hartell for agreeing to serve on my committee and for being a friend to encourage me to keep going on my research.

I would like to thank Mohammed Aboustait, Masoud Moradian and Dr. Kim Taehwan for joining me on my experiment trips to Argonne and Xradia and for their willingness to share all the hardships with me during those days. Amir Hajibabaee, mehdi khanzadeh, Ghazal Sokhansefat: it was a pleasure to work with all of you on my research.

Name: QINANG HU

Date of Degree: DECEMBER 2015

Title of Study: DIRECT THREE DIMENSIONAL OBSERVATION OF THE MICROSTRUCTURE AND CHEMISTRY OF C_3S HYDRATION

Major Field: CIVIL ENGINEERING

Abstract: Although portland cement has been used for over a hundred years as the binder in concrete, the basic mechanism of hydration is still not well understood. Progress has been halted for the fact that it is challenging for most current experimental techniques to give direct observation of the hydration process in-situ and provide quantitative measurement on the microstructure and chemistry at the nano-length scale. Recent advances of nano scale X-ray imaging make nano-tomography and nano-X-ray fluorescence reality. The nano-scale X-ray beams in these techniques allow the sample to be imaged nondestructively and provide a high transmission of signal that penetrate through both sample materials and a possible solution environment, which could make themselves in-situ techniques. Moreover, these techniques can be combined to enrich both datasets to become a more powerful technique. In this dissertation, the applications of both techniques have been established from micron lab scale experiment to nano-synchrotron investigation for studying cementitious materials. The progresses have been shown from first application on 3D chemical characterization of fly ash particles at the nanoscale to later updated versions of in-situ experiments for studying cement hydration, which allow quantitative measurements on 3D structure, chemistry and mass density of hydration products at different hydration periods. These unprecedented discoveries could lead to a breakthrough for both nanoscale analysis of any material and cement hydration research.

TABLE OF CONTENTS

Chapter Page

Chapter Page

LIST OF TABLES

Table Page

LIST OF FIGURES

Figure Page

Figure Page

Figure Page

CHAPTER I

INTRODUCTION

1.1 Introduction

Portland cement is the most important ingredient to the most commonly used construction materials in the world, concrete. In 2012, the US used 76.7 million tons of Portland cement [1]. The production of this material causes 15 % total industrial energy consumption and 5 % global CO2 emission [2]. Any improvements on the usage or understanding of this material could bring significant economic and environmental impacts on society.

Portland cement is not a new material. Since it was invented by Joseph Aspdin of Leeds in the early 19th century, it has been used for over 150 years. However, the basic mechanisms of the reaction of cement and water or hydration are not well understood. Typically, when Portland Cement first gets mixed with water, the initial reaction quickly occur and force a lot of ions into solution. After a few minutes, the reaction rates slow and change what many call a "hibernation state" for several hours. This stage is called the induction period, which is important for the practical reason that the induction period allows time for concrete to be transported and formed into a desired shape. Later, the rate of reaction becomes more activated again and the concrete stiffens and gains strength. Despite many studies of this hydration process, there is still wide spread debates on the basic mechanisms. The obscurity of these mechanisms, on one hand, is attributed to the complexity of the process, which involves not only microstructural evolutions, such as morphological modifications of the solution environment, such as ion transportation and

nucleation. On the other hand, many of the key features can only be observed at a sub-micron length scale. This has been a challenging task for most analytical techniques.

Recent advances of a synchrotron X-rays nano-probe allowed nano-computerized tomography (nCT) and nano-X-rays fluorescence (nXRF) to become a reality. The X-ray computed tomography technique is commonly used in medical science to image internal organs of a human body. This technique uses X-ray images from multiple angles to generate a 3D structural dataset called a tomograph. X-ray fluorescence uses focused X-rays beam to illuminate the sample to make the materials to emit characteristic X-rays from the photo electric effect to determine what elements are present.

Improvement on nanoscale resolution makes nCT and nXRF capable to investigate mechanisms of cement hydration. First as non-destructive techniques, nCT and nXRF can be used to image a sample without causing damage to the microstructure. This allows the sample to be imaged before and after different hydration stages and leads to direct in-situ observations of the changes at different time stages. Second, full 3D volumetric data generated from nCT can turn those observations into quantitative measurements such as the amount of volume change and the amount of reaction product. These values can be measured from bulk analysis by measuring the mass of the sample but challenging for other imaging techniques since they are not able to quantify the amount of material that is present. Finally, by combining nCT and nXRF this can enrich both datasets to become a much more powerful technique than either technique used separately. This could lead to a breakthrough for both nano scale analyses of any material and is especially helpful for cement hydration research.

1.2 Research objectives

The main tasks of this research were to:

- Develop a method of combining lab scale micro-CT with electron microprobe analysis (EPMA) to analyze a fly ash particle to generate a 3D chemical map with micron scale resolution.

- Improve the 3D chemical imaging technique from micron-scale resolution to reach nano-scale level by combining synchrotron nCT and nXRF, which could generate the 3D chemical distribution of a single fly ash particle with nanoscale resolution.

- Modify this nanoscale technique to become an in-situ method that allows direct observations on the microstructural and chemical behavior of cement hydration.

- Use this technique to further understand the initial reactions that occur in solution.

1.3 Overview of dissertation

In this dissertation, work is presented that contributes to a number of bulleted items above

- The second chapter demonstrates a data fusion technique called Tomography assisted chemical correlation (TACCo), which gives both chemical and 3D structural information at 1 micron per pixel resolution. This is the first time that this has been accomplished.

- In the third chapter the TACCo technique gets upgraded to nanoscale resolution, which combines synchrotron nCT and nXRF to generate 3D chemical map of a single fly ash. This has been named nTACCo. Again this is the first time that this measurement has been accomplished.

- In the fourth chapter, nCT, and nXRF is applied to image the samples of a small collection of triclinic C_3S particles for the first seven hours in 15 mmol lime solution. nCT gives microstructural changes at different hydration period. The chemical composition of the hydration product is identified by nXRF.

- In the fifth chapter, several individual C_3S particles are investigated by nTACCo after reaction of 2.5 hours in 15 mmol lime solution. The observations show not only the changes of the microstructure, but also the modification of the chemistry and density of the material. These results

provide new insights on the dissolution and formation of early age hydration products and their role in the induction period.

- Appendix A, supplementary information for the second chapter, provides detailed information of the scan settings and data processing in order to image a fly ash particle using TACCo.

- Appendix B, supplementary information for the fourth chapter, gives the results from many bulk characterization techniques of the C_3S powder. Additional datasets of the replicate scans and samples are also included in this section.

- Appendix C, supplementary information for the fifth chapter, gives the details of the 3D image registration technique. The density distributions of the constituents analyzed by nTACCo are given. Additional nCT datasets for single particle analysis are also given

The research presented in this dissertation is based on the work performed by the author at Oklahoma State University and Argonne National laboratory.

CHAPTER II

3D CHEMICAL SEGMENTATION OF FLY ASH PARTICLES WITH X-RAY COMPUTED TOMOGRAPHY AND ELECTRON PROBE MICROANALYSIS

Abstract

A novel data fusion technique is presented that combines X-ray computed tomography (CT) and electron probe microanalysis to investigate fly ash particles. The technique is called Tomography Assisted Chemical Correlation (TACCo). This technique fuses 2D compositional data with 3D X-ray CT data. The method produces 3D constituent and microstructure maps. Results and observations are presented that show the power of the technique for data visualization as well as quantitative analysis.

Keywords: X-ray computed tomography, electron probe microanalysis, data fusion, segmentation

2.1 Introduction

Fly ash is a waste product gathered from the emissions of coal fired power plants. It is estimated that the worldwide production is over 600 million metric tons [3]. Currently only 40% of this material is used in other processes and the remaining ashes material is placed in special landfills.

Fly ash is made up of crystalline and amorphous phases containing predominantly Al, Si, Ca and Fe [4-7]. The particles are generally spherical with diameters ranging from less than 1 μm to more than 1 mm [3-4,7]. Trace deposits of metals such as arsenic, cesium, lead, selenium, cadmium, and zirconium have been found within these materials [8-10]. Fly ash is commonly used as a low cost construction binder for stabilization of soil, a partial replacement of Portland cement in a concrete mixture, and the predominate binder in a geopolymer concrete [3,11].

Despite the widespread use of this material, there are still a number of important unanswered questions. Some of these include the concern that heavy metals can be leached from the fly ash in solutions. Past research has also shown that fly ash in concrete mixtures has the ability to improve the strength, reduce the permeability, improve the rheology of fresh concrete mixtures, and provide resistance to a number of common durability problems. Fly ash can either act as a supplementary binder or through a secondary pozzolanic reaction with the alkaline pore solution and calcium hydroxide depending on the properties of the fly ash. Substitution levels for Portland cement in a concrete mixture are commonly limited to 20% by mass. This limit is imposed because fly ash is not a manufactured material and therefore not all sources have the same performance in concrete. If this material was better understood then the usage levels could be increased.

This paper presents a new analytical technique that uses a combination of electron probe microanalysis (EPMA) and micro X-ray computed tomography (μCT) to produce 3D maps of the microstructure and distribution of chemical constituents within complex particles. This

methodology has been named Tomography Assisted Chemical Correlation or TACCo by the authors. This technique has the ability to identify different constituent phases and map their 3D location. While the work focuses on applying this technique to fly ash, TACCo applies to any material that can be investigated with both X-ray tomography and a scanning electron beam.

High flux electron beams are commonly used for elemental analysis of materials. An incident electron beam with sufficient energy will cause an atom to emit a characteristic photon through the photoelectric effect [12]. This information can be used to create detailed compositional maps of the surface of materials through the use of energy dispersive X-ray spectrometers [12-15]. To obtain reliable data with the technique a sample must be polished, conductive (or coated in conductive carbon), and analyzed in a high vacuum. While this technique, known as EPMA, is widely used, it has several challenges as it can damage the sample at high probe currents (i.e. > 100 nA), only allows observations of the composition in the first few micrometers to be made, and must be examined in a high vacuum environment [12-13].

It is common in the medical sciences to use X-ray computed tomography (CT) to non-destructively image the internal structure of organisms. This technique uses a series of X-ray radiographs at small angles of rotation that are coupled to produce a 3D model [16-18]. While this technique does not provide direct compositional information about the irradiated materials it does provide clues about compositional consistency. In the CT scan, solid materials with different mass absorption coefficients and densities will appear to have different gray values. However this data does not provide a priori compositional information.

A new generation of tomography techniques is being used that allows the user to enter any domain and find the spatial resolution of unique chemical constituents by combining μCT with information from X-ray Fluorescence. These investigations have been found to require days to gain the data that is needed [19-21]. Furthermore, this technique is limited to 3D models at

roughly 30 microns. The required investigation time for the TACCo analysis can be on the order of hours and produces 3D maps at the resolution size of the parent μCT and EPMA with the current best resolution at 10s of nm [22-23]. Furthermore, once the data has been fused between the μCT and EPMA, then one can continue to only use the μCT for 3D constituent information.

The ability to characterize fly ash at an intimate scale provides new tools to understand, extend, and improve its usage. Specific needs to characterize the elemental makeup, the reactivity, and the location of these constituents within a particle will improve the use. This can have significant impacts on the economy, durability, strength, rheology, and sustainability of modern concretes. The majority of previous work has focused on the measurement of bulk properties of fly ash [24-27]. A few others have tried to characterize fly ash in more depth [7,25,28-29].

These needs to characterize complex powders are not just common to the investigation of fly ash but are common to the study of catalysts, pharmaceuticals, ceramics, contaminated soils, coal, zeolites, asteroids, geologic materials, biomaterials, and others. While these materials have been investigated by either μCT or EPMA no previous publication has successfully fused this data. The presented methods could be useful for any material that can be analyzed by both μCT and EPMA

2.2 Methods

A graphical summary of the methods used is shown in Fig 2.1.

2.2.1 Sample Description and Preparation

This paper investigates three fly ash particles from a single source. The fly ash is classified as ASTM C 618 class C [24]. The results from the bulk XRF analysis is given in Table 2.1. Particles with diameters larger than 200 μm were used, as they were easy to handle and provided a sufficient area to provide a large compositional and μCT data set. The methods described can

be used for any size particle as long as the analytical technique provides adequate resolution. Work on smaller particles will be included in future publications.

A plastic cylinder mold that is open on the top and bottom is filled with a low viscosity epoxy. The epoxy was chosen as it is easy to polish, has a low X-ray attenuation coefficient, and shows minimal outgassing in a vacuum. Before the epoxy hardened, a fly ash particle was placed on the surface of the freshly mixed epoxy and allowed to sink to the bottom. The specimen was then left for a day to harden. A drawing of the specimen is shown in Fig 2.1a.

2.2.2 Micro Computed Tomography

After the particle is embedded in epoxy it was then investigated with a laboratory SkyScan 1172 μCT scanner. A parametric study is summarized in the supplementary information that was completed to find the setting that provides the highest quality images. A summary of the scan and reconstruction settings can be found in Table 2.2. With these settings, 4000 pixels x 4000 pixel radiographs were captured. This allowed tomography models to be reconstructed with a 1.05 μm voxel size. All reconstruction was completed with the SkyScan software NRecon. Both Drishti and Amira software packages were used for 3D visualizations [30,31].

It was important for this work to use the same instrument and reconstruction settings for all subsequent measurement techniques so that quantitative comparisons could be made. An example cross section can be found in Fig. 1e and a histogram of the gray scale values observed is shown in Fig 2.2.

2.2.3 Electron Probe Microanalysis

After investigating the sample with μCT, the epoxy cylinder is then polished with diamond pastes and the exposed a flat cross section was studied by EMPA as shown in Fig 2.1b. The details of the instrument setting is given in Table 2.2 and discussed in supplementary information. The

initial output from this analysis is a backscatter image and a series of elemental images, derived based on raw elemental counts. Examples of the resulting images can be seen in Fig 2.3 for particle 1C. While this information is useful, it is more advantageous to summarize the information by finding compositionally distinct combinations of these elements. An unsupervised clustering analysis known as ISO Means to identify compositionally distinct areas (details given in Appendix A).

This classification scheme has dual purposes; first, it seeks to separate out the constituents of highest compositional variance so that a comparison can be made to the μCT data; second, it allows an estimate of the compositional variance to be determined. The results from this segmentation can be seen in Fig 2.1c and 2.3.

2.2.4 Fusing Electron Probe Microanalysis and micro Computed Tomography Datasets

A novel software algorithm was created that uses the EPMA data to find the matching plane in the 3D tomography data. This algorithm solves a 14 degree of freedom (DOF) optimization problem that finds the location, rotation angle, scaling, and determines the topology of the polished surface of the sample by using eight different localized plains to match the datasets. A reconstruction of the polishing plane is shown in Fig 2.1d and the matching plane is shown in Fig 2.1e. The matches are determined by comparing binary images from the EPMA and μCT data sets and minimizing their difference. Fig 2.1f shows the result of an overlay for a typical sample.

2.2.5 Segmentation of the micro Computed Tomography Data

The correlation between μCT and EPMA now provides the user with guidance on which gray scale values in the μCT correspond to the chemical constituents in the fly ash. Now that the data has been fused, a comparison can be made between the gray scale values of each constituent

phase and their frequency. This allows the range of gray scale values to be determined for each constituent.

To help resolve the overlap between the materials, the mean and standard deviation was determined of each constituent for the cross section, and then these values were projected onto the gray value versus frequency plot for the entire particle. The constituent with the highest frequency was examined first. If there was a constituent with gray values adjacent to the high frequency material, then the limit of that phase was taken as one standard deviation away from the mean in the direction of the overlap. If there was no adjacent constituent phase then, two standard deviations away from the mean was used as the limit. The two standard deviation limit was only used when establishing the boundary between the matrix phases and the high absorption phases. This process was completed for each of the phases in their order of appearance. In some cases, there was significant overlap between the minor phases. These areas of high overlap ranges were defined as a mixture.

Particle 1C contained the most voids of the particles investigated and so was used to determine the limits of the gas phase. This established limit was then used for the other particles. Because of the consistent instrument and reconstruction settings used, a standard value for all of the particles was used.

2.2.6 Analysis of 3D Constituent Data

After establishing the segmentation ranges for each constituent this data can be used to create 3D data sets. An example for Particle 1C is shown in Fig 2.4 with a quarter of the particle removed. This 3D data can be used to find the quantity and distribution of these constituents within a particle. This information is important as not all constituents have the same chemical reactivity or solubility. This means that a particle may be a more effective binder if key phases are concentrated near the surface.

A novel software algorithm was authored that analytically peels the particle into 1 μm layers or shells of uniform thickness that are parallel to the particles outside surface. The details of this algorithm are given in the supplementary information. For each of these layers, the percentage of each constituent is found as well as the distance from the centroid. Since fly ash particles are largely spherical, data can be produced that shows the concentration of these constituents with depth from the surface. Because of border averaging and phase contrasts, the first 8 μm of the data was not included. Methods to better characterize this surface data will be investigated in future work.

2.3 Results

2.3.1 Micro-Computed Tomography

A graph of the number of voxels for a particle at each gray scale is shown in Fig 2.2 for sample 1C. As discussed previously, the gray scale value measured is an indication of the density and the mass absorption coefficient of the constituent material. The initial peak in the histogram corresponds to the gas found in the voids. The peak at gray value 255 is a high absorption material associated with metals. Two peaks near gray values of 50 and 100 can also be seen. This suggests that there are at least three major constituent phases that make up the particle. Some constituent peaks show some overlap, this can be complicated by the presence of minor phases or density irregularity within each phase. These naturally complex materials are a good test for the TACCo method to elucidate what phases can be separated.

2.3.2 Electron Probe Microanalysis

The images derived from the EPMA data for Particle 1C are shown in Fig 2.3. The back scatter, maps of the primary elements, and then the results of the chemical segmentation are given. A color has been given to each unique phase. The details of chemical phases are given in the

supplementary information. A ternary diagram for calcium, silicon, and aluminum is plotted in Fig 2.5. The ternary diagram shows that nine different chemical constituents were identified.

The red and green constituents were found to be the major constituents in each particle investigated. In all three particles the red phase was found to be made up of approximately 20% calcium, silicon, and oxygen with aluminum and iron at 10% and trace amounts of magnesium. In all three green phases they were almost entirely silicon and oxygen. While small concentrations of other elements are found in each constituent, the standard deviation was found to be the magnitude as the mean for the element and so not statistically significant. This suggests that some of these elements may be present but are not a fundamental element in that constituent.

2.3.3 Data Fusion

An overlay of the EPMA and μCT is shown in Fig 2.1f. At each pixel the gray value and the corresponding constituent phase is recorded and the number of observations at each gray value is plotted in Fig 2.6. The top plot shows the total number of observed pixels at each gray value for the different constituent phases from the overlay of the cross sections from the EPMA and μCT. The color of each line is indicated by the corresponding color from the EPMA segmented image. Also the mean is shown by a solid line and the standard deviation is shown as a dashed line. For the red phase two standard deviations is also shown towards the high absorption material as a line with finer dashes.

The lower plot of Fig 2.6 shows the voxel distribution. The x-axis of these two plots is aligned and the mean and standard deviation have been extended so that these values can be compared in both plots. Again, the line colors correspond to the labels of the constituents from the EPMA analysis.

The segmentation decisions are based on the scheme mentioned previously. A summary of the means and standard deviations is given in Table 2.3 for particle and phase. After establishing the limits for each phase the results are given in Table 2.4.

2.3.4 3D Data Analysis

Fig 2.4 shows the segmented 3D data set for Particle 1C. Colors in this image have been changed to improve the data presentation. The gray, purple, dark gray and black correspond to the red, green, mixture and high absorption constituent phases respectively. The peel algorithm is then used to find the distribution of the phases within Particle 1C. Results are shown in Fig 2.7. In this plot the y-axis shows the percentage of the constituent present versus the depth from the outside surface. Since fly ash particles are spherical in nature, these thicknesses go from the particle surface towards the center. This data shows how the constituent concentrations change over the particle diameter.

2.4 Discussion

Micro computed tomography is a powerful nondestructive 3D analysis technique that is widely used in the medical sciences. The gray values from these measurements are an indication of the mass absorption and density of the material. It is not currently possible to directly use these gray values to indicate the chemistry of a material unless it is a very simple sample. For example in Fig 2.2 it is possible to determine that gas, a high absorption, and at least two other constituents exist but it is challenging to determine their limits for gray scale segmentation. Also it is not possible to determine the compositional makeup of these constituents. The TACCo technique is able to overcome these limitations and allow for a more thorough segmentation from μCT data.

2.4.1 Repeatability of the Method

TACCo was used on three different particles from the same source of fly ash. The data in Table 2.3 and Fig 2.5 show that the compositional makeup for the red and green phase was consistent. Consistency was also found in the fused data sets, as the mean and standard deviation of these constituents as shown in Table 2.3 were similar for both the red and green constituent. The fusion data for the other constituents did not match, but this is expected as they are unique compositional phases. Finally, the ranges given in Table 2.4 for the final segmentation of the particles were also similar. In Particle 1C, it was possible to determine a range of gray values for the green phase. However, this was not possible for the others, because there was too much overlap of the in the minor phases. Further segmenting these minor phases will be examined in future work.

2.4.2 Compositional Makeup of Fly Ash

The EPMA data allows powerful observations of the compositional makeup of these complex fly ash particles. While differences in the minor constituents were observed, the red and green constituents were found in each of the three particles investigated and consist of over 90% of the cross sections investigated with the EPMA as outlined in Table 2.3. The red constituent was the most prevalent observed in the particles as it was never less than 45% of the volume of a particle and regularly greater than 75% of the volume.

2.4.3 Chemical Consistency with Depth

A strength of TACCo is that it can observe the compositional consistency over the depth as shown in Fig 2.7. This information about the uniformity is helpful to understand the chemical reactivity of the particle with depth. Of the three particles investigated, Particle 2C was found to be consistent in all constituents over the depth. The other particles were found to change with their depth as described below.

Particle 1C had the greatest volume of gas. The gas increased with depth and the red and green constituent decreased. The green constituent decreased until about 75 μm from the surface and then stayed approximately constant. The mixture stayed at a constant concentration in the particle. The high absorption constituent showed increased concentrations at 35 μm and 120 μm from the surface. This seems to be unique to this particle.

In Particle 4C a high concentration of the mixture was observed at the surface and then decreased with depth. As the mixture decreased, the red and gas phase increased until 20 μm from the surface. After 20 μm the red phase stayed constant as the mixture continued to decrease and the gas increased. The high absorption phase was found to increase from the surface until 90 μm and then decrease.

2.4.4 Potential applications of TACCo technique

In this work a calibration was needed to fuse the EPMA and μCT data. After this calibration has been established on a number of particles then, these same gray values ranges can be used for future particles. This will allow subsequent similar particles to be compositionally investigated only using μCT. This allows a larger number of particles to be scanned simultaneously, segmented by gray scale, and then subsequently investigated with the peel algorithm. With the present equipment, an 8 mm high scan can be performed with a 1 μm resolution in the same sample chamber, and since there are no size constraints to this method, hundreds of particles can be scanned at once. This technique now becomes an outstanding tool for many applications where a large number of particles need to be rapidly characterized.

After establishing the composition associated with an absorption range it is also possible to create a 3D chemical map of a complex particle and then subject it to a solution and then create a new 3D chemical map to determine the changes to the particle. Since the μCT technique is nondestructive it is possible to continue to use the same sample and image subsequent changes.

Because the initial gray value is known then so would the compositional content. Any changes to the volume, density, or compositional consistency can also be imaged. This creates a 5D set of observations to be made. This includes changes in spatial location, compositional consistency, and time. These observations can provide critical in situ measurements of how complex materials react in different solutions.

2.5 Conclusions

This paper has presented a new analytical technique, Tomography Assisted Chemical Correlation (TACCo). TACCo was shown to create 3D chemical maps of complicated materials by combining EPMA and μCT on the same sample. By fusing this data, a calibration is made that helps guide the segmentation of the μCT data to produce 3D constituent maps of the microstructure. From the particles investigated, the following statements can be made:

- The technique was demonstrated to perform consistently on three different fly ash particles from the same source.
- The technique found that there were two unique constituents that made up over 50% of the volume of the particles. Minor phases in the particles were observed as well.
- The segmentation range for these repeated constituents were similar between particles.
- 3D chemical models were created for the fly ash particles.
- The subsequent analysis of these 3D models showed that while there was similarity between the constituents in each, the chemical distribution with depth differed.

TACCo is unique because it has the ability to create detailed 3D chemical maps of materials regardless of whether they are crystalline or amorphous. As X-ray techniques continue to improve the resolution and capabilities of TACCo also improves. With existing laboratory

instrumentation, the data produced is already useful and has the ability to give great insight into important materials.

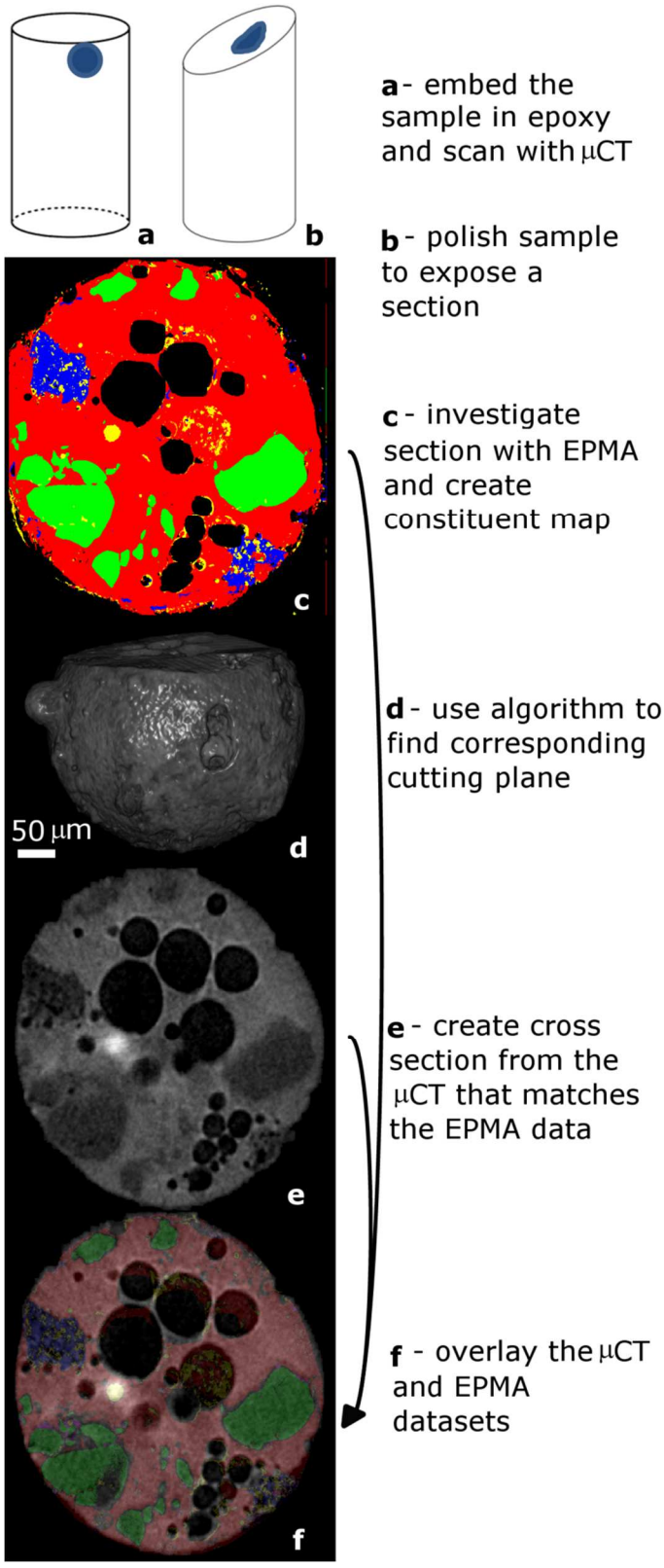

Figure 2.1 – An overview of the processes used for fusing the EPMA and μCT data sets.

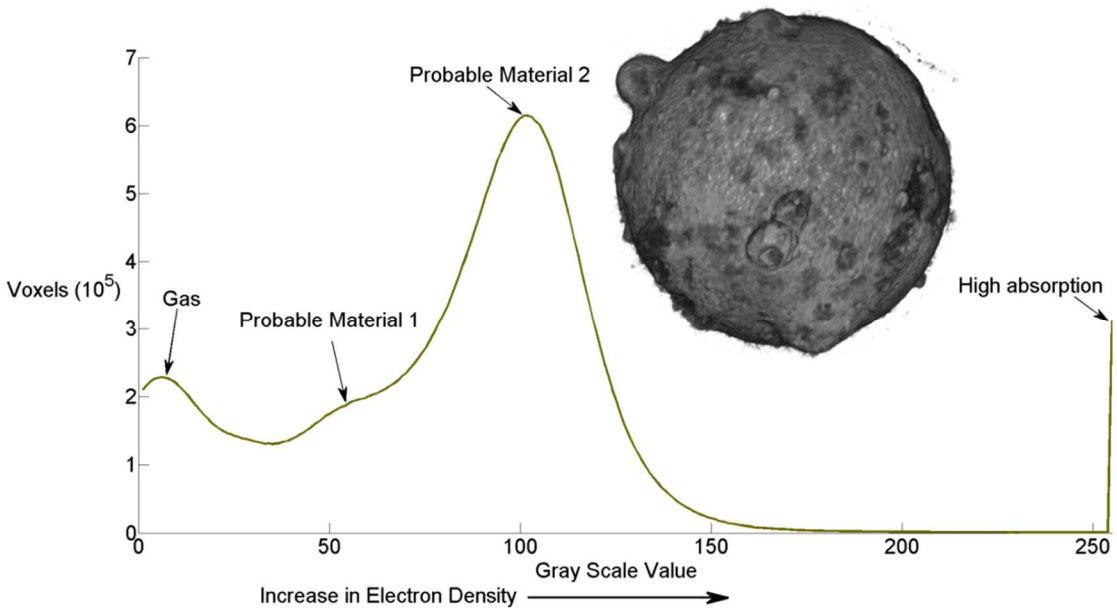

Figure 2.2 – The number of voxels at different gray scale values from the 3D μCT data set for Particle 1C.

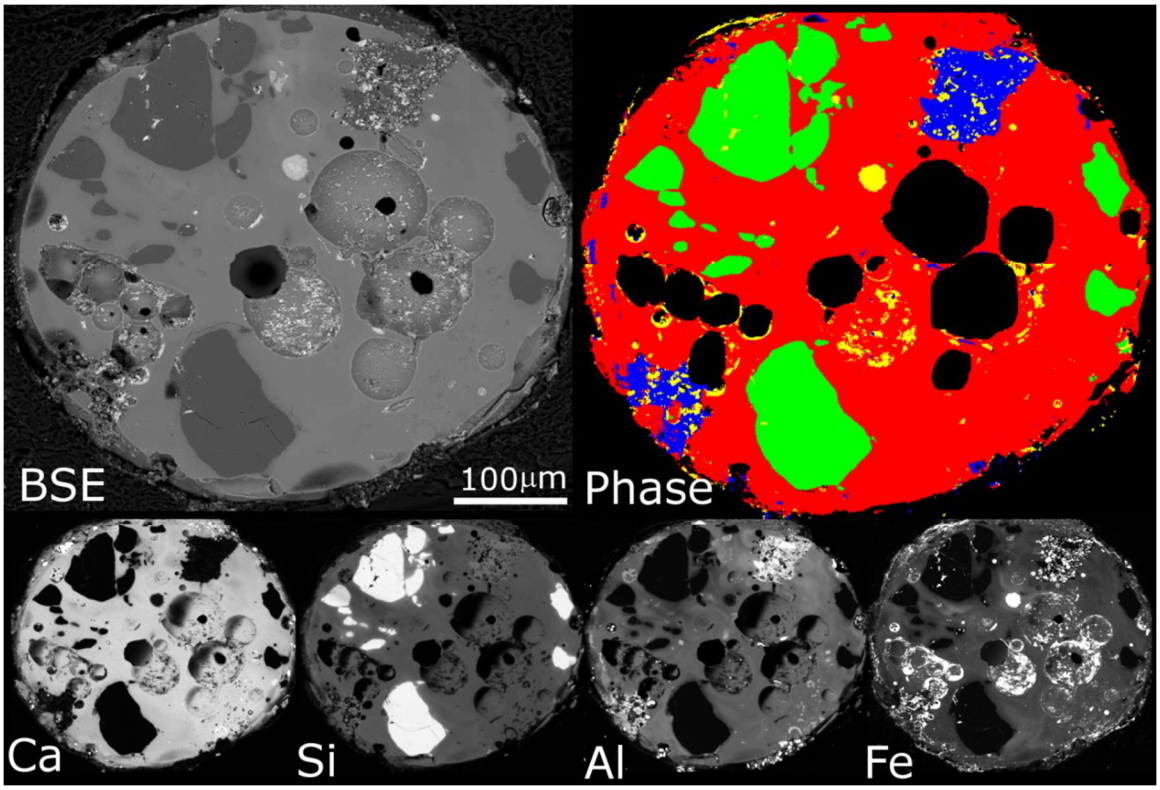

Fig 2.3 – The gray scale images shows the backscatter and elemental maps from EPMA for particle 1C. The segmented constituent phase analysis used in TACCo is shown in the upper right.

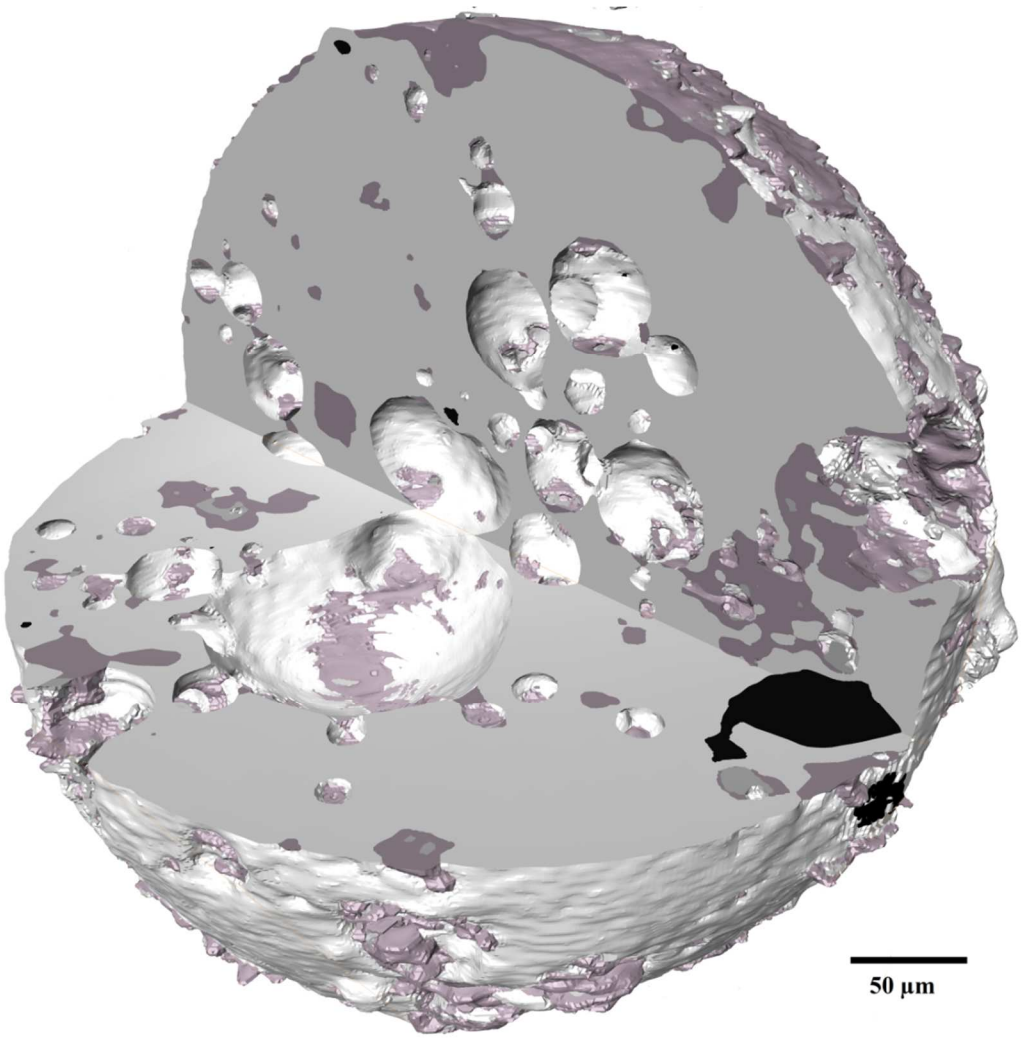

Fig 2.4 – A 3D model of the segmented µCT data. One quadrant of the material has been removed so that it is easier to view the distribution of constituents within the particle.

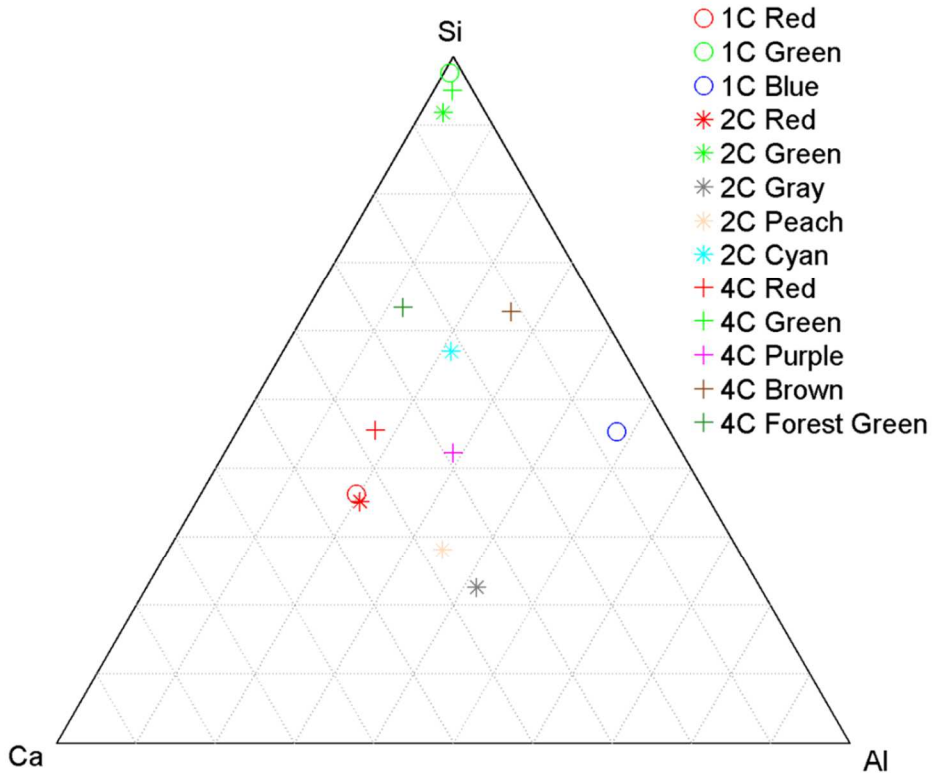

Fig 2.5 – A ternary diagram for the Si, Ca and Al composition for different unique constituents.

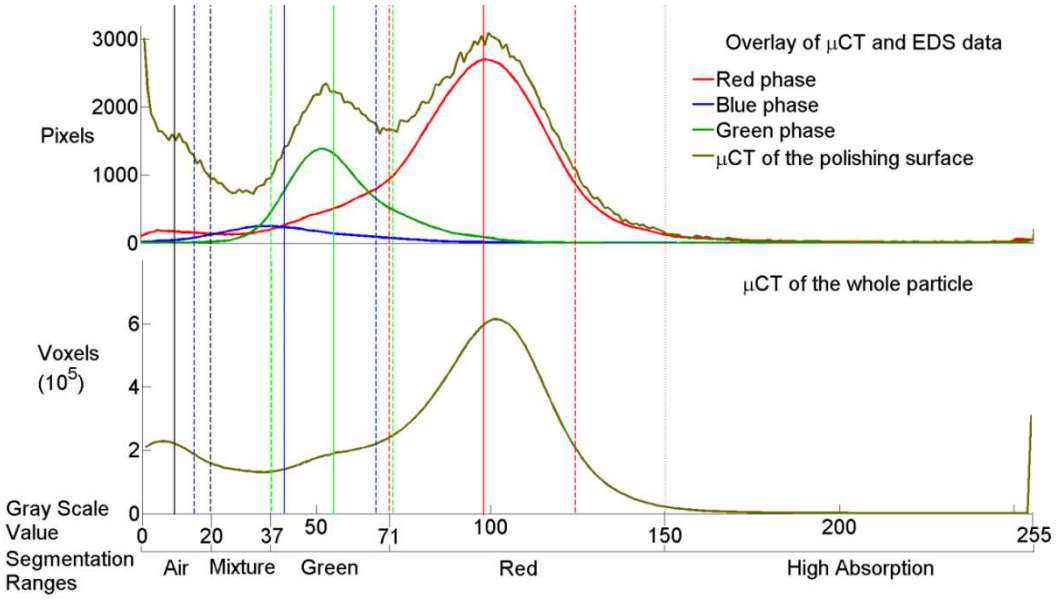

Fig 2.6 – A comparison of the EPMA and μCT data. The top plot shows the number of pixels versus the gray scale value from the data sets. The mean is shown as a solid line and the standard deviation as a dashed line. The bottom plot shows the number of voxels versus gray scale for the entire particle with the projected mean and standard deviations.

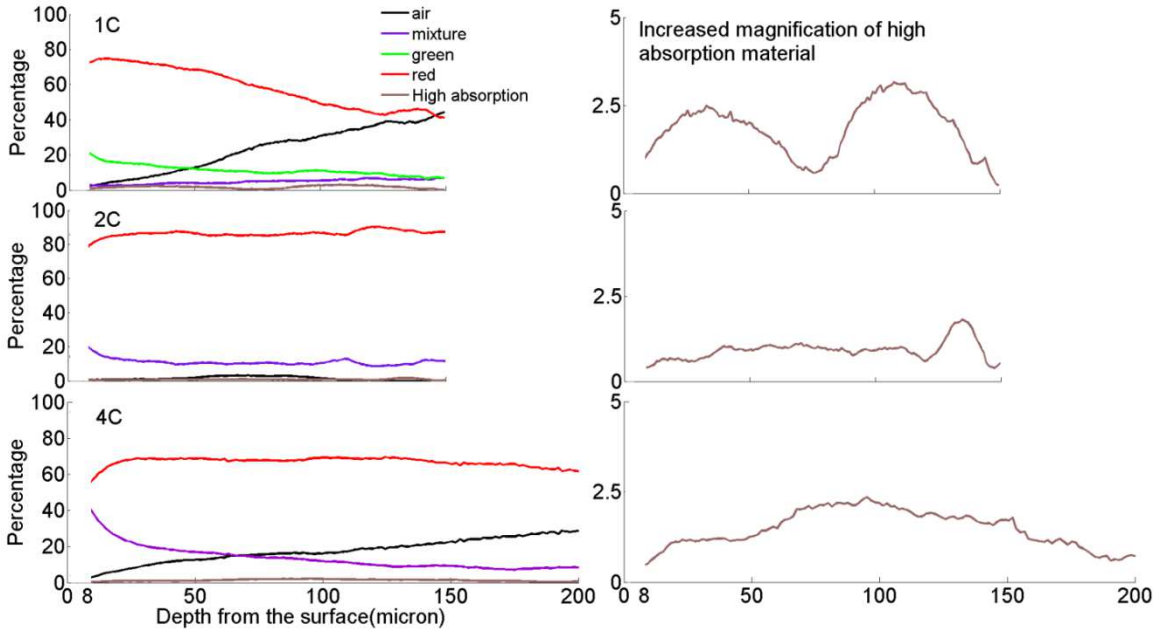

Fig 2.7 – A plot of the percentage of each of the segmented phase within the 3D particle versus the distance from the centroid of the particle.

Table 2.1 – A powder XRF analysis for the fly ash investigated in this study.

SiO_2	36.21
Al_2O_3	19.94
Fe_2O_3	6.67
CaO	23.96
MgO	5.17
Na_2O	1.67
K_2O	0.52
TiO_2	1.44
MnO_2	0.03
P_2O_5	1.44
SrO	0.38
BaO	0.69
SO_3	1.44
L.O.I	0.15
Moisture	0.04
$SiO_2+Al_2O_3+Fe_2O_3$	63.12
ASTM C 618 classification	C

Table 2.2 – Scan settings from the μCT.

Parameter		Setting
Source Voltage		29 kev
Image Pixel Size		1.05 um
Filter		Al (0.5mm thickness)
Rotation Step		0.3 deg
Number of Frames Averaging		4
Dynamic range	Low	0
	High	0.73
Beam Hardening Correction		30%

Table 2.3 – Summary of the mean and standard deviations of all the phases.

Phases		Particle name		
		1C	2C	4C
Red	Mean	98	103	99
	1σ	27	21	18
Green	Mean	55	76	63
	1σ	17	24	28
Air	Mean	10	10	10
	1σ	10	10	10
Blue	Mean	41		
	1σ	26		
Cyan	Mean		87	
	1σ		23	
Peach	Mean		109	
	1σ		24	
Brown	Mean			60
	1σ			34

Table 2.4 – Summary of segmentation ranges for three particles.

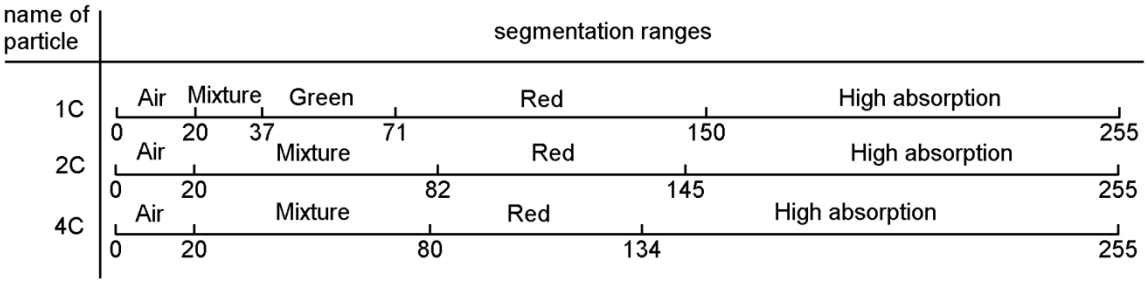

CHAPTER III

COMBINED THREE-DIMENSIONAL STRUCTURE AND CHEMISTRY IMAGING WITH NANOSCALE RESOLUTION

Abstract

While there is great interest to characterize and modify materials at the nano scale, progress has been slow because few techniques allow for critical observations at this length scale. This work presents a data fusion technique that combines synchrotron-based X-ray nano computed tomography (nCT) and nano x-ray fluorescence (nXRF) to non-destructively investigate complex nanoscale materials and provide combined three-dimensional (3D) renderings of microstructure and chemistry. The technique has been named nano Tomography Assisted Chemical Correlation (nTACCo) and is demonstrated on fly ash particles with nanoscale chemical inhomogeneities. Our findings show that nTACCo is capable of providing the concentration and location of eight different nano inclusions within a particle. This work also provides direct observations of reactivity and chemical distribution of fly ash. This ability to combine 3D structure and chemistry at a nano scale will provide unprecedented tools for nano science in material science, biology, chemistry, and medical science.

Keywords: nTACCo, X-ray computed tomography, X-ray fluorescence, data fusion, fly ash

3.1 Introduction

3.1.1 Background

Progress has been halted in a number of research fields because direct investigation of three dimensional (3D) nanostructure and chemistry are very difficult to achieve [32,33]. A number of fields could benefit from this ability including corrosion,[34-36] battery design,[37-40] green cements,[3,41-42] , porous materials,[43,44] cancer research,[45] and interactions between tissue and prosthetics[46,47]. In each of these fields there are critical mechanisms involving changes in the structure and chemistry at the nano scale that are unknown.

A powerful method to study these applications is X-ray radiation produced at bright light sources.[48] X-rays offer high penetration power and great chemical sensitivity. Unique synchrotron based techniques including nano X-ray diffraction, fluorescence, and tomography have been developed at the hard X-ray nanoprobe beamline, which is operated in partnership between the Advanced Photon Source (APS) and the Center for Nanoscale Materials (CNM) at Argonne National Laboratory. These techniques in their current capability are able to image length scales of roughly 15 nm, and even smaller scales will be possible in the future[22,49-51].

A new analytical technique is presented that combines nXRF and nCT to quickly and efficiently produce 3D maps of the microstructure and distribution of chemical constituents within fly ash particles. This methodology has been named nano Tomography Assisted Chemical Correlation or nTACCo. This technique has been demonstrated with fly ash, a complex material with paramount importance for the production of the next generation of green cements [3,52,12]. Trace deposits of metals such as arsenic, cesium, lead, selenium, cadmium, and zirconium have been found within these materials and have made them controversial as the metals pose a threat to the environment, if not handled correctly [3,12,13,23,42]. This paper presents for the first time a 3D combined chemical and microstructure map at the nm length scale that was obtained non-

destructively and is the latest evolution of fusing imaging and microanalysis measurements [53,54].

3.1.2 Nano-Computed Tomography

X-ray computed tomography (CT) is commonly used in the medical sciences to non-destructively image the internal structure of organisms. This technique combines a series of X-ray radiographs at small angles of rotation to produce a 3D tomograph [16-18]. Typically the technique is used to investigate volumes larger than a micron^3. This is common for laboratory or synchrotron micro-CT (mCT). With mCT, useful contrast can be found between materials with different mass absorption coefficients and density. These differences can be used to determine the spatial distribution of material constituents by looking at the different X-ray intensities transmitted [54,55].

However, when CT is used at the nanoscale the number of atoms interacting with the beam is much smaller. This means that the difference in the X-ray absorption of the constituent matter is also much smaller [36]. Because of this it is challenging to use these techniques to determine the difference between two materials unless there is a great difference between their mass absorption coefficients or electron density. Nevertheless, three-dimensional structural investigations have recently become possible at the nanoscale. For example, the first three-dimensional view of the pore structure of an aluminosilicate geopolymer gel has been reported, which has the potential to improve the strength and reduce the permeability of concretes based on this class of binders [23]. Others have had to use dyes, nano contrast agents, or Atomic Layer Deposition in order to image their samples [56,57]. Although structural information is obtained, a detailed knowledge about the distribution of different unique constituents cannot be extracted unless assisted chemical analysis techniques have been applied, which could involve sample modification, or the

knowledge of constituents composition has been well established for those manufactured materials [54].

3.1.3 Nano X-ray Fluorescence

Nano X-ray fluorescence (nXRF) can provide elemental maps with detection below a part per million (ppm) level. In this technique a primary X-ray beam illuminates a sample and an energy dispersive detector is used to measure the fluorescence X-rays leaving the sample. Each chemical element will emit fluorescence radiation at characteristic energies. By rastering the primary X-ray beam over the sample it is possible to create 2D maps of materials.

Notwithstanding its undisputable success, the technique is hindered by two major factors: 1) the X-ray beam will penetrate into the material and cause X-ray fluorescence along its path, making it challenging to directly render depth-dependent information; 2) X-ray fluorescence is self-absorbed in the sample before it can reach the detector, which, depending on the severity, complicates adequate quantification of the signal. Both effects make it difficult to determine the distribution of the elements through the depth of the sample. Other work has translated the focus of the X-ray beam at different points of a sample to learn more about the spatial distribution of elements within a specimen [49,58,59]. However, this approach is very time consuming and limited to the depth-of-view of the focusing optics. X-ray fluorescence tomography has recently become available [60-62]. However, this technique is limited to lower-resolution X-ray fluorescence microscopy, since it requires high efficiency X-ray optics. The high-resolution focusing optics used in nanoprobes exhibit inherently low efficiency. Consequently, dwell times are relatively high, which prohibits the acquisition of many 2D maps of the sample. For example, an X-ray fluorescence tomography scan with a voxel resolution of 30 nm would require about 1800 maps taken at angles between 0 and 180 degree. In conclusion, the lack of 3D information from nXRF is a current limitation of the method.

3.1.4 Fly ash

Currently, there is a need to better understand the composition and microstructure of complex materials. Fly ash is a waste product from the combustion of coal during power generation. These materials are typically landfilled if other applications are not found. The particles are generally spherical with diameters ranging from less than 1 μm to more than 1 mm [3,4,7]. Fly ash is commonly used as a low cost construction binder for stabilization of soil, a partial replacement of Portland cement in a concrete mixture, and the predominate binder in a geopolymer concrete [3,12]. By using this material within other binders it is thought that these metals are bound within the hydration products and not available for leaching. However, this is not well understood. If a better understanding of the location and concentration of these metals could be found then this might better guide the usage of these materials

Previous research on fly ash has primarily focused on the measurement of bulk properties [24-27]. Only a few others have tried to characterize fly ash in more depth [7,27,28,54]. With nTACCo, the ability to characterize fly ash at an intimate scale provides new tools to understand, extend, and improve its usage. Furthermore, this technique can be applied to any complex material where greater understanding of the structure and chemistry is needed.

3.2 Method and experiment

3.2.1 Overview of the Technique

Nanoscale x-ray fluorescence and tomography are extremely valuable as they can provide quantitative observations at critical length scales. However, both techniques have obvious limitations. The nTACCo technique combines both techniques in order to overcome these limitations. The nTACCo technique is designed to use a small number of nXRF projections in combination with microstructure from nCT to get a 3D distribution of chemistry and microstructure. Fig 3.3 shows an overview of the method. The sample is shown with regions that

have high chemical concentrations of calcium. Several 2D projections are shown from nXRF analysis at four different angles. Each angle gives a map of the constituent on that projection orientation. For each angle investigated, the pixel on the projection corresponds to a fiber passing through the sample from the X-ray source. These individual 2D projections can be used to provide detailed information about the boundary, location, and size of this area of high concentration. This information is then combined with the nCT data so that this unique chemical information can be combined with the microstructural information. This ultimately creates a 3D map of the particle that combines the microstructure and the unique constituents in the sample.

3.2.2 Sample preparation

The sample investigated was a single 16 μm diameter ASTM C618 Class C fly ash particle [24]. The bulk chemistry information of the source of fly ash powder is given in Table 3.1. The powder was dispersed in isopropyl alcohol and sonicated in order to isolate a single particle. The tungsten needle tip was bent to make it easier to place the fly ash particle. The needle was covered with two part epoxy and then a single particle was placed on the tip of the needle. Next a suspension was made of ethanol and 200 nm gold balls. This was sprayed on the sample leaving a few gold balls. The sample was exposed to 1 M NaOH for six hours before scanning in order to cause the particle to react.

3.2.3 Nano-Computed Tomography

The particle was investigated with nCT at sector 26 of the Advanced Photon Source at Argonne National Laboratory. A thorough overview of the capabilities of this instrument is provided in Winarski et al. [22,49]. Rendering was completed with Drisht [30]. The overview of nCT data is given in Fig 3.1. The detailed scanning and reconstruction settings are given in Table 3.2.

For the full-field imaging and nanotomography monochromatic X-rays are steered onto a gold-coated elliptically shaped glass capillary which focuses the X-rays onto the sample. The

condenser's position in space (x-y-z-tip-tilt) is adjusted in software and positioned according to the incident X-ray energy. The condenser optic is also mounted on a piezoelectric driven stage which is scanned in x and z over the period of acquisition to uniformly illuminate the sample plane. Additionally a diffuser consisting of cellulose fibers mounted in a rotating assembly upstream of the condenser is used to randomize structure in the X-ray beam supplied by the beamline. There are two condensers in the instrument, one for absorption contrast imaging and one for phase contrast imaging, both designed to focus x-rays over the energy range of 8-10 keV. The condensers are matched in numerical aperture to the objective zone plate in order to fully illuminate the optic. A central beam stop is located at the downstream end of the condenser to block straight through beam (X-rays not reflected by the capillary) and together with the condenser provide a hollow cone of X-ray illumination to the sample plane. An order sorting aperture (150 μm diameter platinum-iridium alloy pinhole) is positioned between this cone of illumination and the sample to block any X-rays that may have traveled around the outside of the condenser.

The sample rotates on a precision rotation stage. Errors in the radial and vertical motion of the rotation stage are monitored with a series of capacitance micrometers which can measure positional variations as small as 3 nm. An x-z stack of piezoelectric driven positioners is mounted above the rotation stage in order to align the sample (or a region of interest within the sample) onto the axis of rotation.

Due to the fine length scale, any imperfections in the gears of the automated stage, eccentric sample mounting, and small thermal changes can cause significant movement during the scan. A laser system is used to track these movements and compensate. But even so, the rotation center was shifting during the scan. In order to combine the individual radiographs for a tomograph, the rotation center of all the images must be aligned. To ease the reconstruction a gold particle on the

sample is chosen and kept in present of every radiograph. The gold particle was used as the reference point for aligning the rotation center and to validate the combination of nTACCo.

3.2.4 Nano X-ray Fluorescence

After completing nCT the same particle was investigated with nXRF. Emitted characteristic X-ray fluorescence radiation is detected with a four-element silicon drift energy dispersive detector (Vortex ME4) [22]. A Fresnel zone plate (objective zone plate) is located downstream of the sample at a fixed focal length for a given incident X-ray energy. The objective zone plate diffracts the X-ray beam that has passed through and around the sample plane and focuses a magnified image of the sample plane onto a high-resolution X-ray detector system. The X-rays are focused onto a specially polished thallium doped cesium iodide (CsI-Th) crystal which converts the X-rays to visible light which is detected by a coupled microscope objective and CCD imaging camera. Scanning of the focusing zone plate provides high-resolution maps of the elemental distribution of the samples. Fluorescence data have been analyzed using the software package MAPS [64]. The data is displayed in their normalized intensity ranges, and their actual intensity ranges are given in Table 3.3. Fitting and quantification of the fluorescence data was carried out with thin film standards (National Bureau of Standards, Standard Reference Material 1832 and 1833). The elemental maps results from different orientation are given in Fig 3.2. The detailed settings of the scans are given in Table 3.2.

3.2.5 Data fusion

Despite the nCT and nXRF analysis being completed without moving the sample from the stage, the correlations between the orientations were not trivial. A technique was developed that would scale and align the data. This makes the technique more versatile as both detectors do not have to be in the same instrument. An overview of the method is shown in Fig 3.3. An example of combining this data is shown together with fibers from four orientations in Fig 3.4.

A new data set was created to transform the 3D tomograph model into an emulated 2D projection so that the investigation angles of the nXRF and nCT could be directly compared. To create a tomographic projection each slice from the 3D tomography was translated into lines or 1D profiles. The 1D profile from each slice was then combined to create a 2D map. Therefore, each pixel in the tomographic projection corresponded to a volume of voxels on a projection fiber from 3D tomography. This pixel was then given a gray value based on the average gray value of the voxels on the projection fiber. After creating this data set, then comparisons were made between the nXRF and nCT data sets.

The particle border is primarily used for the alignment of the two techniques. Due to the low contrast in nCT, the gray value is challenging to use for determining the particle border. However, entropy as the textural image feature was found to be a better choice for this purpose. The entropy value of one pixel is calculated based on its neighbor 7 by 7 pixels and it can be calculated by equation (1).

$$S = \sum_{i=0}^{255} -P(i) \cdot \ln\big(P(i)\big) \qquad (1)$$

As the image depth is 8 bit, the possible gray value i in equation (1) is from 0 to 255. The probability of a gray value $P(i)$ is as the number of pixels has gray value i divided by the total pixels inside the neighborhood pixels. In the nXRF maps a uniform distributed elemental can be used to determine the border of the particle. The zinc maps were chosen to be segmented for the border of the particle as it was uniformly present in the fly ash.

After the corresponding boundaries were found, the nXRF data was resized and shifted so that it could be overlayed on the tomographic projection. This was done for each of the nXRF projections and a comparison was made between the nCT tomographs to find the orientations with the best match. Now the models share the same coordinate system. The elemental maps were then overlayed as shown in Fig 3.3 behind the tomographic projection. The location of the

high concentration areas can then be determined on the tomographic projection. This was repeated for the other three rotation angles used in the nXRF analysis and a result from the 2D projection is shown in Fig 3.4.

3.3 Results

One typical radiograph image of a fly ash particle is shown in Fig 3.1a. The gray value of each pixel in the image is associated with the remaining intensity of the X-ray beam after passing through the sample. The reduction of intensity is caused by X-ray absorption of the material. The material constituents in the spherical particle have a X-ray absorption that is different than the air surrounding the particle. This is the reason for the features of the particle having a different gray value. The texture patterns in the particle show the complex interior microstructure, such as a network of fractures or pore system. These same structures can be seen in the tomographic slice shown in Fig 3.1b. The complex interior structure of the particle can clearly be seen. In addition gold fiducial markers can be clearly seen because of their high contrast. Several bright areas are caused by X-ray phase contrast enhanced by sharp edges in the sample. The size of each pixel in each slice is approximately 15 nm by 15 nm. By stacking all the slices together, a 3D model of the structure of the particle can be created as shown in Fig 3.1c. Movies have been included in the supplementary section showing the complete data sets for Fig 3.1a, 3.1b, and 3.1c.

Four nXRF maps are shown in Fig 3.2 for four different angles with a step size of 150 nm/pixel. For each element, the map shows the concentration of that element by a common intensity scale. Red shows the highest values and black the lowest. Their detailed intensity ranges can be found in the supplementary information. A downstream ion chamber (ds_ic) measures the x-ray flux passing through the sample. This map represents the transmission at each pixel and is similar to a nCT radiograph. The nXRF data were used to find areas of high elemental concentration. These

high concentration areas represent materials with a different chemistry then the bulk of the particle. They can be isolated in the elemental maps by thresholding the data to a concentration level above the background. Work in this paper focused on imaging areas of high concentration of Au, Al, K, Ti, Cr, Fe, and Ca. Lighter elements such as Si and S exhibit shadow effects in their maps. Shadowing is caused by the absorption of the fluorescence X-rays by the materials of the particle before they can reach the detector. This effect can be corrected by using two detectors or a larger number of observation angles.

The projection fibers of high Au and Ca areas from different orientations are shown to intersect at the white regions in the tomography data, as shown in Fig 3.4. The original slices are shown for comparison. The area in the overlap region for the Ca data does not correlate with a distinct feature in the nCT slice. This highlights the limitation of nCT to observe unique chemistry in these materials. However, the overlap region for high Au areas closely corresponds to high X-ray absorption areas in the nCT data. By combing all the high concentrations areas from fused images together, a 3D model of the high concentration areas was created with the same coordinate system as the tomography. In Fig 3.5, the 3D model of the high concentrations for Au, Ca, Fe, K, Ti and Cr have been labeled with different colors and their average gray value and chemical compositions are given in Table 3.4. Several cross sections have also been shown so that greater spatial information can be obtained. A movie of the 3D model has also been included in the supplementary information.

3.4 Discussion

The elemental information from nXRF analysis was combined with microstructure information from nCT for the first time to create a 3D chemical map at the nano scale. A strength of nTACCo is that it can be completed in about three hours of instrument time and one hour of analysis time. Furthermore, the 3D data provides ppm chemical concentrations at a 150 nm scale and is

nondestructive to the sample. These are significant advantages over previous 3D chemical mapping methods as they are very lengthy or destroy the sample during their investigation. Because the sample is not destroyed during analysis, this lends itself to experiments that explore simultaneous chemical and microstructure changes of the sample in solutions, under load, or at different temperatures. This technique can be used for many complex samples, but is especially helpful to investigate materials with complex internal microstructure and non-homogenous chemistry.

As one example, the results from this technique are helpful to understand the reactivity of fly ash that has been placed in a reactive media. The technique clearly shows the inhomogeneity of the particle and the spatial relationships of the constituents. The constituents near the surface of the particle generally have a greater opportunity to react with a dissolving solution than the constituents in the depths of the particle. A number of high Ca regions were found close to the surface of the particle. This means that this high Ca region could be important to the early chemical reactions that take place. This data also shows that high concentrations of Fe are not near the surface and would be less likely to react.

The 3D structure model from nCT can give further insight on the interior changes in the material from a dissolving fluid. As shown in Fig 3.1b, the inner microstructure shows a series of cracks and pores in the particle. This network would give solution direct access to the inside of the particle and therefore allow internal constituents to react. Based on other imaging of these particles it is hypothesized that certain constituents have dissolved at a faster rate than others. When these constituents dissolve they leave behind these voids in the particle. This is an important finding for fly ash, as the existing dissolution models have focused on uniform dissolution from the outside of the particle [29,63].

The average gray values for the different constituents shown in Table 3.4 suggest that the average gray values of all constituents are very similar except for the Au areas. This means that the nCT technique by itself is not able to distinguish between these constituents. As mentioned before, due to the small amount of atoms that interact with the X-ray beam, the contrast between different constituents in nCT is generally too low to segment them unless they have a significant difference in mass absorption coefficient. This means that many unique constituents will not be observed with this technique. However, by having the chemistry information from nXRF, these unique phases inside the tomography can be identified.

To validate the accuracy of the technique the Au fiduciary markers were used. These gold nanoparticles were placed on the surface of the sample at the beginning of the experiment and Au was not found within the fly ash. Therefore these Au areas in the nXRF correspond to the gold balls. Because of the high mass absorption coefficient of this constituent they can be easily visualized in nCT data. As shown in Fig 3.4, the high absorption or white regions in the nCT data correspond to the same locations of the overlap of the Au fibers from four orientations of the nXRF data. This suggests that this technique was able to accurately map this area of high concentration.

The spatial accuracy of the technique is controlled by the lowest resolution between nXRF and nCT. Since the step size of nXRF is 150 nm/pixel compared with the 15 nm/pixel for nCT, in the current study the fusion resolution is limited by the nXRF. It is possible to obtain nXRF data with a step size of 30 nm/pixel. This would further increase the accuracy of the method. Results will be presented in future work.

Since the high concentration areas are identified by using the intersection of four orientations, it is likely that this technique will underestimate the areas of unique chemistry. Improved details could be found if a larger number of angles were investigated with nXRF. One possible

extension of the method is to use the nTACCo to tell the user which area of the particle has a unique chemistry and then rely on clues from the nCT to complete the segmentation. For example it may be possible to use a unique image texture, shape, or gray value to further segment the data.

It should be noted that the segmentation of element maps is an important step in the sensitivity of this technique. If a high concentration area was not identified in all orientations then it will be excluded from the final 3D model. For the high Fe area in the particle some details were lost in the 3D model because of the complex geometry and slender features of the constituent.

3.5 Conclusion

Following conclusions can be drawn from this paper.

- The 3D structure information from nCT and 2D chemical information from nXRF was combined with a novel data fusion technique called nTACCo. This is the first time that a 3D combined chemical and microstructure map at the 150 nm length scale was created in only a few hours.

- The technique was validated through the use of Au fiduciary markers.

- The technique was able to create 3D segmented maps of six constituents that would not have been determined by only using the nCT technique because of low X-ray absorption contrast.

- The 3D results from this technique show that the dissolution of this fly ash particle occurred throughout the volume and not just at the surface. These internal channels are likely caused by localized rapid dissolution.

This combination of nCT and nXRF allows a new generation of imaging techniques to be created for investigations of nanoscale materials. Since this technique is non-destructive, it lends itself to

changes in these materials under different actions over time. Although this work was done at a synchrotron nanoprobe facility, the technique can be extended to laboratory scale equipment with increased imaging time.

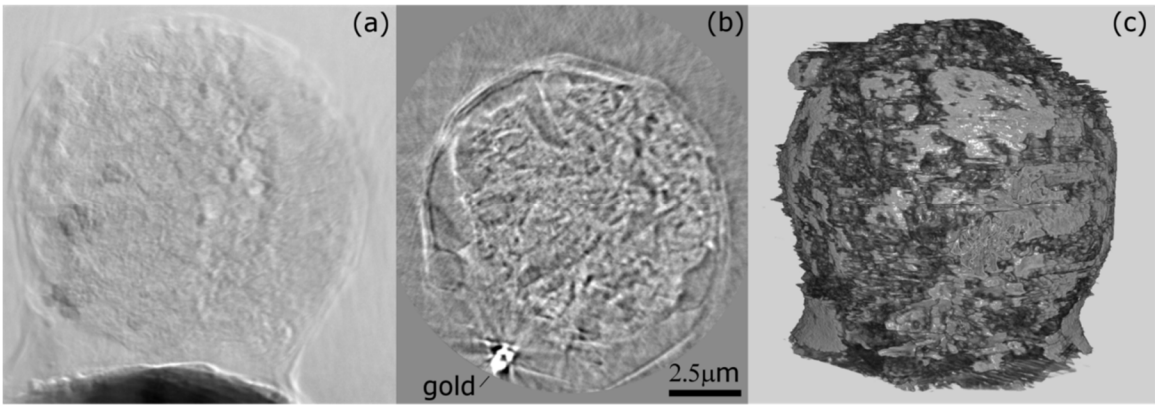

Fig 3.1 – Overview of nCT data. Panel a shows a typical radiograph. Panel b shows a typical tomography slice and panel c a 3D rendering of the particle.

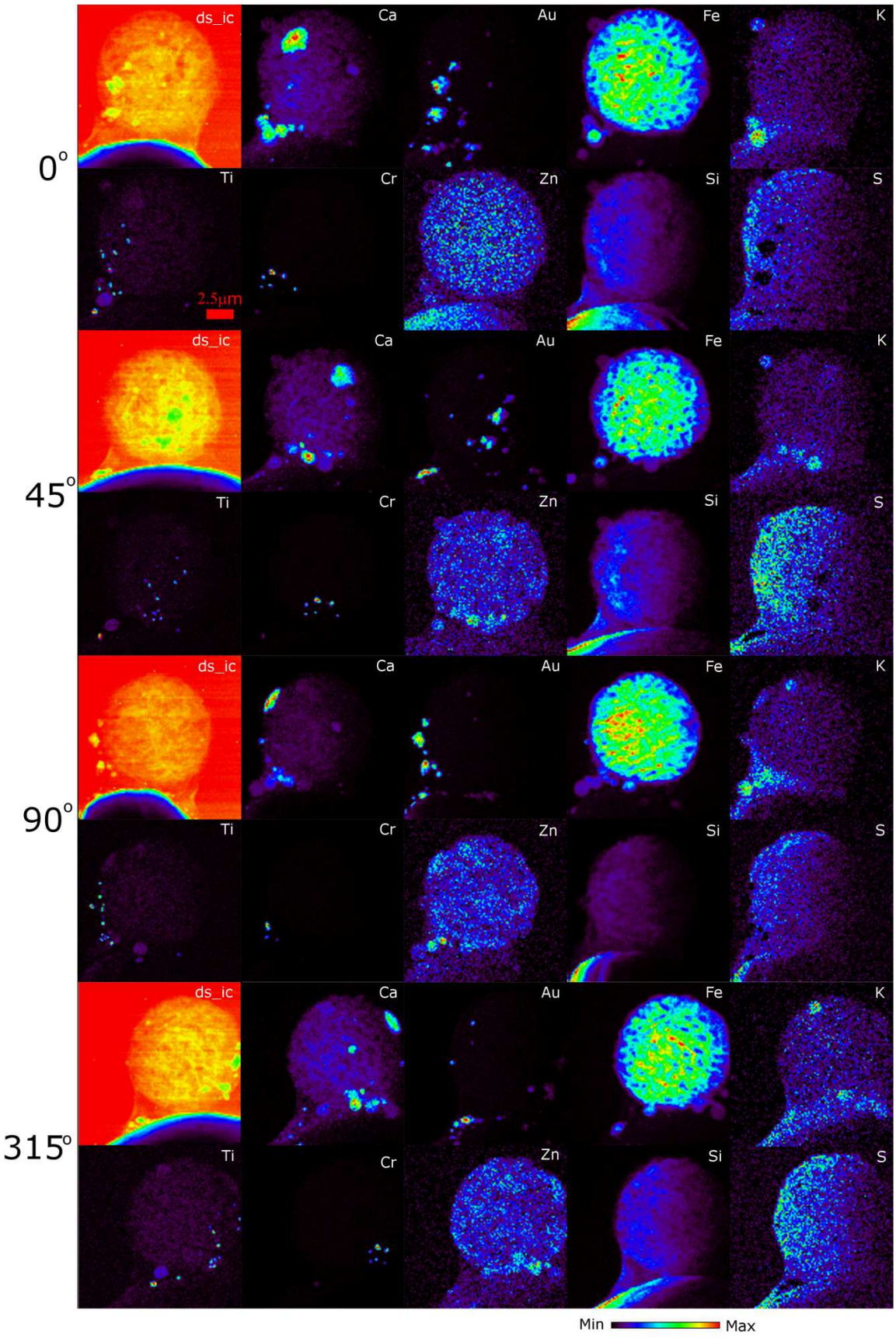
0°
45°
90°
315°
ds_ic
Ca
Au
Fe
K
Ti
Cr
Zn
Si
S
2.5µm
Min
Max

Fig 3.2 – Element maps from nXRF at orientations of 0^{o}, 45^{o} ,90^{o}, and 315^{o}

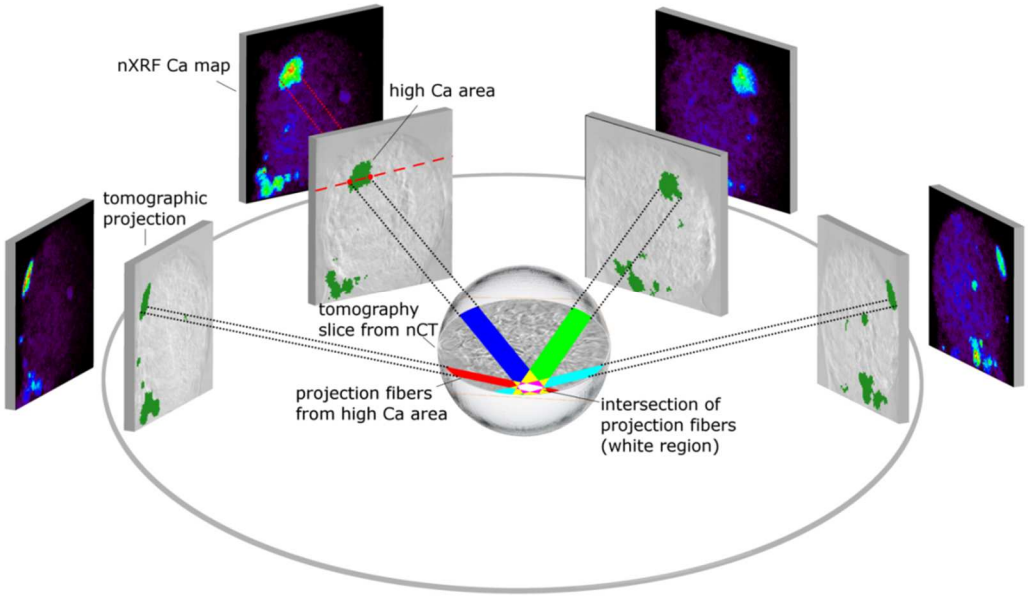

Fig 3.3 – An overview of nTACCo. The nXRF Ca maps were first overlaid with the tomographic projections to align both coordinate systems. Next, the projection fibers from the combined data set are projected onto the tomography slice to find the intersections. This intersection highlights the high concentration geometry in the 3D data set.

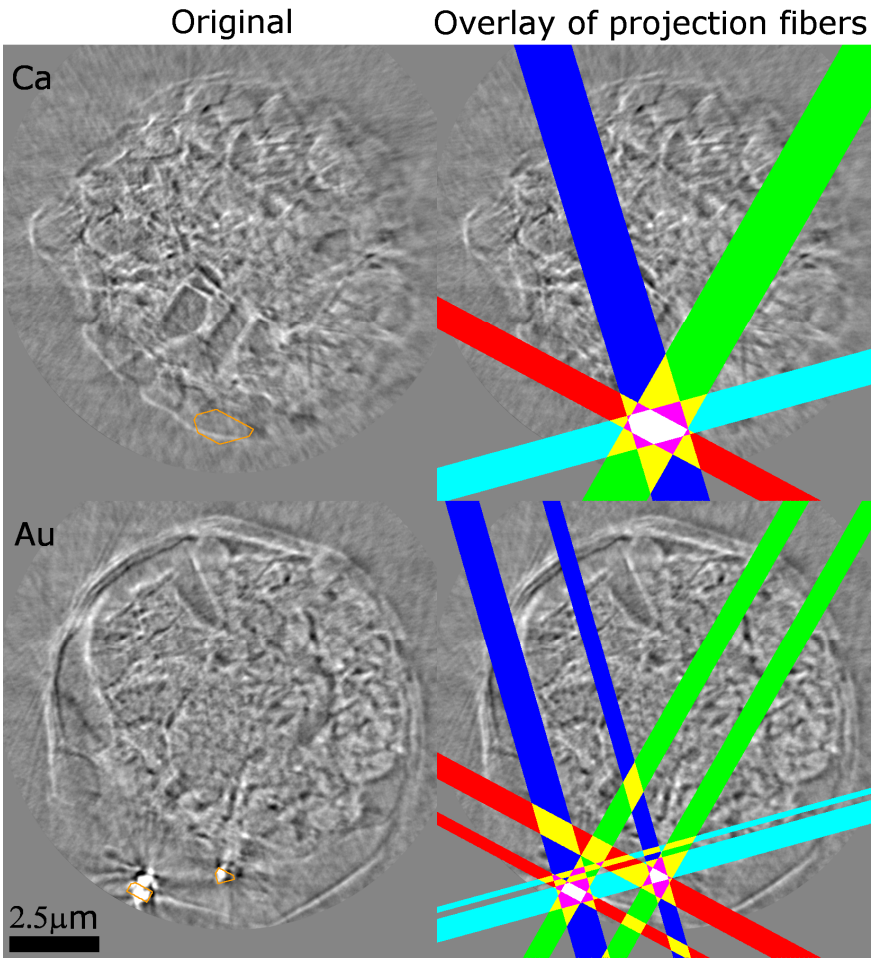

Fig 3.4 – A comparison of the original tomography slice and the projection fibers of high Ca and Au from four nXRF projections.

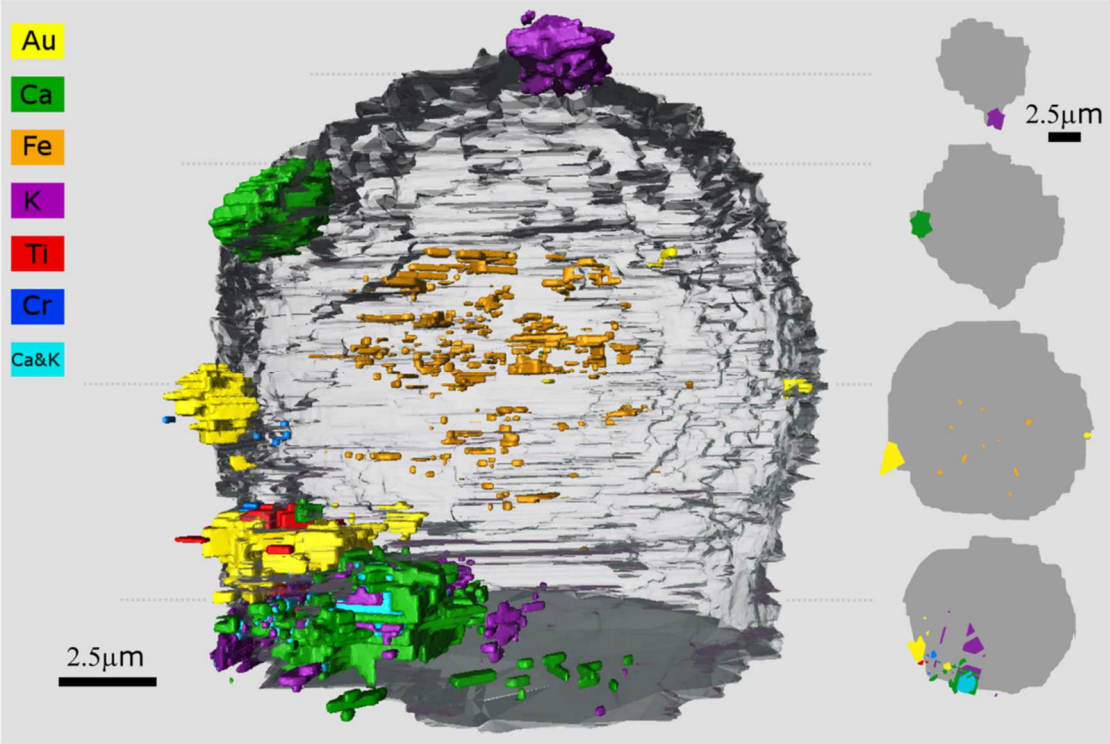

Fig 3.5 – The 3D chemical model of high concentration regions and several cross sections that shows the chemical diversity of the fly ash particle.

Table 3.1 – Bulk chemistry of the source particles.

SiO_2	38.34
Al_2O_3	19.87
Fe_2O_3	6.12
CaO	23.07
MgO	5.16
Na_2O	1.53
K_2O	0.62
TiO_2	1.43
MnO_2	0.02
P_2O_5	1.09
SrO	0.35
BaO	0.64
SO_3	1.14
L.O.I	0.62
Moisture	0.01
$SiO_2+Al_2O_3+Fe_2O_3$	64.34
ASTM C 618 classification	C

Table 3.2 – The instrument setting for both nCT and nXRF experiments.

nCT	Resolution		15.6 nm/pixel
	Exposure time		6 s
	Source energy		8 kev
	Optical magnification		x10
	Dynamic ranges*	min	-5000
		max	5000
nXRF	Resolution		150 nm/pixel
	Detector dwelling time		0.1 s
	Scaler count time		0.1 s

* the data is displayed in FLOAT type

Table 3.3 – The maximum concentrations and the orientations of the radiography coordinate systems for the nXRF maps in Fig 3.2.

nXRF orientation	maximum concentrations (μg/cm^2)								radiography orientation
	Ca	Au	Fe	Zn	Al	Si	S	K	
0^o	66.6	3184	1.07	80.7	229	2386	67.5	12.6	106^o
45^o	66.5	2385	1.06	80.3	196	1903	37.7	11.3	60.3^o
90^o	127	3103	1.1	72.7	211	5177	72.3	10.8	15.3^o
315^o	46.3	2574	1.06	78.5	202	2423	48	7.29	151.9^o

Table 3.4 – A summary of concentration and gray values of high concentration regions.

Rich element and labeled color		nCT gray value	nXRF element concentration (ug/cm^2)						
			Au	Ca	Fe	K	Cr	Ti	Seg range
Au (yellow)	Mean	184.9	667.1	6.2	24.4	1.3	3.4	1.9	Au>150
	σ	76.8	618.5	6.7	17.6	1.3	12.3	4.0	
Ca (green)	Mean	138.1	37.6	26.7	29.7	0.9	0.7	1.7	Ca>15
	σ	33.1	140.4	16.4	13.6	0.8	3.0	1.7	
Fe (orange)	Mean	137.3	40.8	8.1	60.0	1.0	0.9	1.8	Fe>55
	σ	51.6	96.7	5.3	4.5	0.8	1.7	1.9	
K (violet)	Mean	133.6	123.4	6.1	25.1	3.1	2.1	1.7	K>2
	σ	32.7	324.9	3.2	17.5	1.3	10.0	2.9	
Cr (blue)	Mean	146.8	331.4	8.8	22.8	1.8	31.3	3.8	Cr>7
	σ	75.7	430.5	8.0	15.3	1.7	25.7	6.9	
Ti (red)	Mean	154.0	293.0	5.7	27.3	1.0	1.9	16.0	Ti>7
	σ	50.7	531.9	3.3	17.3	0.9	7.0	8.5	
Ca & K (cyan)	Mean	133.6	82.0	30.6	20.0	3.7	1.5	2.6	Ca>15 & K>2
	σ	31.6	222.3	16.9	13.6	2.0	7.1	4.0	

CHAPTER IV

DIRECT THREE-DIMENSIONAL OBSERVATION OF THE MICROSTRUCTURE AND CHEMISTRY OF C_3S HYDRATION

Abstract

Disagreements about the mechanisms of cement hydration remain despite the fact that Portland cement has been studied extensively for over 100 years. One reason for this is that direct observation of the change in microstructure and chemistry are challenging for many experimental techniques. This paper presents results from synchrotron nano X-ray tomography and fluorescence imaging. The data show unprecedented direct observations of small collections of C_3S particles before and after different periods of hydration in 15 mmol/L lime solution. X-ray absorption contrast is used to make three dimensional maps of the changes of these materials with time. The chemical compositions of hydration products are then identified with X-ray fluorescence mapping and scanning electron microscopy. These experiments are used to provide insight into the rate and morphology of the microstructure formation.

Keywords: Microstructure; Ca3SiO5; Hydration product; EDX; Nano-tomography

4.1 Introduction

Tricalcium silicate (C_3S) is a major component of Portland cement. It reacts with water to form calcium silicate hydrate (C-S-H) and calcium hydroxide (CH). This hydration process determines most of the early-age properties of concrete and has been studied for decades. If one could understand and predict the kinetics and microstructure development during this process, strategies could be designed to control it and thereby improve the quality and economics of concrete. However, the mechanisms of hydration are not fully understood [65], and values of many of the thermodynamic and kinetic properties needed to make accurate predictions have not been measured [65-68]. In fact, agreement has still not been reached even about the basic mechanisms of early-age hydration due to a lack of sufficiently detailed experimental observations, especially of direct, in-situ evolution of the microstructure that can be used to guide numerical simulations [65-70].

Scanning electron microscopy with energy dispersive X-ray spectroscopy (SEM-EDS), transmission electron microscopy (TEM), atomic force microscopy (AFM), white light interferometry, and nano-indentation have been used to study cement hydration and to characterize the hydrated microstructure, especially the calcium silicate hydrate product (C-S-H) [71-88]. Generally, C-S-H is classified as "inner" or "outer" products, according to their location relative to the original boundary of the C_3S grains [73-87]. However, this classification is limiting because of the difficulty of imaging techniques to locate the original boundary of the C_3S grain in a hydrated microstructure. The products have also been classified based on their apparent density and chemistry [74-78,81]. The molar ratio of calcium to silicon (Ca/Si) in C-S-H is commonly accepted to be between 1 and 2 depending, on the hydration environment when the products are formed [83,89-93]. Recent work with SEM-EDS and nano-indention has suggested that there is likely an inter mixing of CH with C-S-H in hardened paste samples [81]. Different

degrees of mixing could lead to different Ca/Si of hydration product that are possibly outside typical values [73,94].

Electron microscopy has also suggested that the dissolution of C_3S is controlled by the formation and coalescence of etch pits on the grain surfaces [79,80,86,87]. These etch pits seem to form preferentially where mechanical damage from grinding or crystalline imperfections are present in the material. Despite these observations being of great insight, this work has not been able to make direct observations of the evolution of the in-situ structure over time. In addition, these imaging techniques require careful sample preparation that may introduce artifacts. Furthermore, since the surfaces are examined at such high magnification, the observations are highly localized and may not statistically reflect the structure or kinetic behavior at greater length scales. These challenges make it difficult to obtain quantitative measurements that are representative and can aid in the development and validation of predictive models based on chemistry and physics.

Soft X-ray microscopy has been used to take in-situ time-lapse nanoscale transmission images while C_3S is reacting at an average water-to-solid (w/s) ratio of five [95,96]. The technique provides information about the structure of the hydration products and the process of formation during in-situ reactions. However, analyzing the images is challenging because the 3D microstructure is projected onto a 2D transmission image. This is similar to the radiographs shown in this paper. Results from this work have suggested that the hydration process occurs not only on the surface, but also inside of the C_3S particle, although the technique cannot resolve the specific location and is only roughly quantitative [95].

Recent advances with synchrotron hard X-ray nanoprobes have allowed X-ray nano-computed tomography (nCT) and nano X-ray Fluorescence to (nXRF) to become a reality. These techniques are capable of non-destructively imaging at a resolution of 16 nm. The sample preparations for these techniques are also minimal, so this technique lends itself to evaluating

processes that change over time. These techniques can be combined with other experimental methods and the results can be used as a starting point or as a comparison to computer simulations [23,49,56,97-100].

X-ray computed tomography (CT) is commonly used in the medical sciences to non-destructively image the internal structure of organisms. This technique combines a series of X-ray radiographs at small angles of rotation to produce a 3D tomograph [16,18]. In addition to the structural information, the materials investigated have different contrast depending on their X-ray absorption. The X-ray absorption is a function of the density and mass attenuation coefficient. For a given X-ray energy level, the mass attenuation coefficient is a function of the average atomic number with some discontinuities caused by X-ray absorption edges [54.101,102]. No X-ray absorption edges were encountered for the instrument settings and materials investigated. If there is significant contrast in X-ray absorption among the constituent materials, the data can be used to separate them in the images. The material interfaces are sometimes highlighted by edge diffraction [103,104], which can be used to find edges in low-contrast images. The use of nCT for construction materials has been quite limited. However work has been done to investigate the 3D structure of aluminosilicate geopolymer gel and the early stages of reaction of fly ash [23,97].

nXRF is a powerful tool when combined with nCT because it can provide elemental maps with detection limits better than a part per million (ppm). In this technique, a primary X-ray beam illuminates a sample and an energy dispersive detector is used to measure the fluorescence X-rays emitted by the sample. Each chemical element fluoresces at characteristic energies from the small region, so rastering the primary X-ray beam over the sample enables the creation of 2D chemical maps for the image [97,99,105].

In this paper, nCT is primarily used to investigate individual C_3S particles before and then after different time periods of hydration. The full 3D tomography from nCT gives direct observations

of the behaviors of C_3S hydration at both the surface and inner structure of the samples. The quantitative results from this technique provide accurate measurements of different hydration behaviors at different time periods. Thanks to the non-destructive nature of nCT, the same sample can then be scanned by nXRF. The resulting elemental maps give useful information about the chemical composition of the hydration product.

The goal of this work is to establish the utility of nCT and nXRF to study C_3S hydration during its first several hours. Additional work is ongoing to further refine the techniques to improve fundamental understanding of the mechanisms and measuring the relevant structural and kinetic properties that are needed by numerical models of chemical and microstructural evolution; this will be the subject of future publications.

4.2 Materials

The triclinic C_3S powder used in this study was produced by Mineral Research Processing (Meyzieu, France). The material has been characterized with inductively coupled plasma optical emission spectroscopy (ICP-OES), X-ray powder diffraction (XRD), automated scanning electron microscopy (ASEM) for particle size distribution analysis, multipoint nitrogen adsorption (BET method), and isothermal calorimetry during 24 h of hydration. Experimental details are contained in Appendix B. The elemental composition of C_3S obtained from ICP-OES and the BET surface area are shown in Table 4.1. The XRD pattern indicates that this material is close to pure triclinic phase. Based on ASEM observations of 4000 particles, 95 % of them are between 1 μm and 7.5 μm in average dimension. For the calorimetry experiments, two samples were prepared using the w/s of five by mass with a solution of 15 mmol/L $Ca(OH)_2$ solution at either 25 ^oC or 50 ^oC. These samples were designed to replicate the conditions of the nCT and nXRF experiments in this paper. Another sample with w/s of 0.40 using deionized water was also included in order to show the performance of this material in a more practical w/s. For the calorimetry samples with

w/s of 5.0, there was no stirring during the reaction and so some settlement is expected during hydration. This means that the timing in the images may not exactly match the calorimetry data; however, the suspension provides an average w/s that matches the nCT experiments and previous soft X-ray microscopy work. Three time periods of hydration in the imaging experiments are labeled on the x-axis as wide bars. The details of the materials characterization is provided in Appendix B.

4.3 Experimental Methods

4.3.1 Sample preparation and hydration

With the low X-ray energy used in these techniques, it was not possible to examine hydration in situ at industrially relevant w/s; a much more dilute suspension was required to permit X-ray transmission. However, dilute suspensions tend to promote extremely rapid initial dissolution rates of C_3S, potentially causing them to dissolve completely before measurements could be made. Past research using calorimetry measurements on continually stirred suspensions has shown that mixtures with solutions saturated in lime showed comparable hydration rate profiles in suspensions with w/s from 0.5 up to 5.0 [106,107]. This was also confirmed by calorimetry data presented in Fig 4.1. Because of this, a w/s of 5.0 was chosen for these experiments

The sample was prepared by first separating individual C_3S particles of which sizes were 15 μm or smaller and fixing them to the tip of a tungsten needle with epoxy, as shown in Fig 4.2. Gold particles that were approximately 100 nm in diameter were then placed on the C_3S as fiducial markers. A fixed mass of additional C_3S powder was affixed to the needle shoulder below the tip. An initial nCT scan of the assembly was performed, and the assembly was stored in a dry nitrogen environment to prevent prehydration or carbonation.

To intentionally reduce the initially rapid rate of C_3S dissolution that happens in water, these hydration experiments were performed using a 15 mmol/L $Ca(OH)_2$ solution, which was prepared in advance by adding reagent grade lime (CaO) to continuously stirred deionized water. The solution was filtered and stored in a nitrogen environment to minimize carbonation.

A cone-shaped polyethylene cup was tightly fit to the needle for holding the solution (Fig 4.2). The particle assembly could be alternately submerged in, then extracted from, the solution by moving the cup up or down along the needle. A volume of solution was added to the polyethylene cup so that w/s = 5.0 in the hydration environment. Each sample was submerged in fresh solution for times between 2 h and 7 h. Four samples were tested at 25 °C, including two at 7 h, and one sample (3C) was hydrated at 50 °C. After the prescribed hydration time, the reaction was interrupted by solvent exchange using isopropyl alcohol, and the sample was then imaged again. Isopropyl alcohol was used as it is suggested to cause minimal damage to the sample microstructure [108-112]. To confirm this, radiographs of Sample 3C were taken while submerged in solution and then again after being submerged in isopropyl alcohol. The results will be discussed further in section 4.1. The sample names and the reaction times are summarized in Table 4.2. The sample names provided merely a means of identification and do not have a specific meaning beyond that.

The data sets before and after hydration were registered so that one-to-one comparisons could be made. Next, the data were segmented into different material sets for qualitative and quantitative comparisons. For one sample, nXRF imaging was used to investigate elemental distribution of the hydrated sample. In addition, SEM-EDS imaging was used to confirm these findings. Details of instrumentation settings used in this study, including nCT, nXRF, SEM, and EDS are provided in Table 4.3.

4.3.2 Nano-tomography

All nCT measurements were made in the Hard X-ray nanoprobe at Sector 26 in a shared space between the Advanced Photon Source (APS) and the Center of Nanoscale Materials (CNM) in Argonne National Laboratory. The instrument settings are given in Table 4.3 and more details can be found in the study of Winarski et al. [22] and the Appendix B.

Radiographs and tomography are the two types of datasets collected from a nCT experiment. A radiograph is an image of the direct projection of the X-rays. The absorbed X-rays after passing through the sample generate an image, which carries the information from both the surface and interior structure. These data sets are similar to the ones produced by soft X-ray microscopy and can be useful, but sometimes challenging to interpret. A tomograph is the reconstruction of radiographs by combining the images from multiple angles. It is a 3D dataset of slices through the sample. By stacking the slices together, a 3D structural model of the sample can be produced. All of these scans produced a 3D array of pixels (or voxels), with each voxel being 15.6 nm on a side.

The gray value in the nCT dataset correlates to the X-ray intensity, I, transmitted through the material, which is a function of the mass attenuation coefficient, μ_m, density, ρ, and path length, x:

$$I/I_o = \exp(-\mu_m \rho x) \qquad (1)$$

where I_0 is the original intensity of the X-ray beam. The mass attenuation coefficient is a function of the chemical composition and density of the material, and the energy level of the X-rays [113]. The regions around the edges and internal interfaces of materials have more pronounced diffraction which can cause lighter gray values in these regions. This phenomenon is called a phase shift and can be used by phase contrast imaging to enhance the visibility of edges [103,104].

Quantitative information can be obtained from nCT data by separating the slice images into regions of different constituents based on their gray values into regions of different constituents. Due to the low contrast of the nanoscale imaging, the segmentation is not feasible by simple threshold of the gray value [54,97]. Phase contrast at the edges of the sample can be used; but its effectiveness depends on the accuracy and quality of the data and on the materials being imaged. For instance, the separation between solid and air is the easiest to determine, because of the sharp differences in densities. In contrast, the separation of remaining C_3S and hydration product is not always perceivable. This work has attempted to be conservative by not reporting results in cases when the data could not be clearly segmented. The location of the needle was used to align the images so that identical locations (within 15.6 nm) could be compared quantitatively at different hydration times.

After hydration, the dimension of the reacted sample was sometimes larger than the scan window. In these circumstances a mosaic tomography technique was used [114]. In this technique the sample was systematically moved in the field of view and a series of radiographs was captured. Successful post-alignment of the radiograph required approximately 20 % overlap between each image recorded. These overlapped regions were then used to stitch the radiographs together into a single image, and then these images were used to reconstruct a tomograph of the sample. This technique allowed a much larger tomograph to be created without sacrificing the resolution of the technique. While mosaic tomography is not a new technique, this is the first time that it has been successfully used at a nano length scale. This technique was helpful for the data sets obtained from the current study because large volumes of hydration products were common and it was not possible to predict where they would form. The reconstruction software Stanford TXRM Wizard was used [114]. Reconstruction details can be found in the supplementary information.

4.3.3 Nano X-ray fluorescence

One sample was investigated with nXRF after completing nCT. Emitted characteristic X-ray fluorescence radiation is detected with a four-element silicon drift energy dispersive detector [22]. Additional details can be found in Hu et al. [97]. Fluorescence was analyzed using the software package MAPS [64]. Fitting and quantification of the fluorescence data were carried out with thin film standards (National Bureau of Standards, Standard Reference Material 1832 and 1833). The detailed settings for the scans are listed in Table 4.3.

Two major challenges must be overcome to obtain quantitative chemical composition data by nXRF. First, the X-ray beam penetrates into the material and causes X-ray fluorescence along its path, making it difficult to directly render depth-dependent information. Second, X-ray fluorescence is absorbed in the sample before it reaches the detector, which complicates adequate quantification of the signal. A correction needs to be applied first to the original nXRF data before the data can be quantitatively used. However, qualitative observations are still useful and valid to tell the overall distribution of the elemental composition of the sample, using the raw nXRF data. In this study, the absorption artifacts were also minimized for materials closest to the detector. The detector was always present on the left side of the images. The pixel size in each of these scans was 150 nm. The quantitative evaluation of the data has been restricted to a region that was within 3 μm of the left boundary of the sample. That depth was chosen because prior work [115] suggests that less than 25 % of the Si and 5 % of the Ca X-rays should be absorbed in this region. Future work will focus on further refining of the data to examine larger depths.

4.3.4 SEM-EDS

Partially hydrated samples were investigated by SEM-EDS in order to validate the observations of chemistry from nXRF. The setting of the instrument is given in Table 4.3. One sample of the anhydrous triclinic C_3S material was used to verify the calibration of EDS.

4.4 Results and Discussion

A summary of the samples and changes in their dimension and volume are shown in Table 4.2. Samples were investigated at three different time periods of hydration and at two different temperatures. For the C_3S and the $Ca(OH)_2$ solution used in this study, not much change was observed in the first two hours of hydration, confirming the efficacy of the $Ca(OH)_2$ solution in slowing the initial reaction. But after 2.5 h the changes were significant. More detailed observations for individual samples will be presented in the following sections.

It should be noted that due to limited synchrotron time that only one replicate sample was able to be investigated (7 h of hydration at 25 ^oC). Although these two samples showed good agreement, the limited number of repeat samples means that care should be taken in drawing strong conclusions at a single time period. However, each presented observation was taken from hundreds of similar observations of the phenomenon from the 3D data sets. This means that strong statements can be made about the stated phenomena and their distribution within a single sample.

4.4.1 Impact of Isopropyl alcohol on sample integrity

Radiograph experiments were conducted to investigate the influence of isopropyl alcohol on sample preparation. Through these experiments, the geometry and microstructure of the hydrated samples were compared while they were in solution with those after the solvent exchange. Although radiographs do not give 3D information, they only took a short time and were still useful to obtain the information about the boundary and internal changes of the sample.

Fig 4.3 shows four different radiographs of Sample 3C, each of which was taken at different conditions: 1) before hydration, 2) after 10 min of hydration, 3) after 2.5 h of hydration, and 4) after the solvent exchange. This test was performed at 50 ^oC. It should be noted that both radiographs for the anhydrous sample and the sample after submerging in isopropyl alcohol were imaged in air and the others were imaged in lime solution. The border of the particle was

identified using the orange line (see the radiographs in the second row of Fig 4.3). These lines were drawn based on visual inspection of the images. The gold particle was observed to move during the 2.5 h hydration period. This is likely caused by hydration products forming between the particle and the needle.

A rectangular area, shown by a white dashed box, has been magnified from three of the radiographs. These areas were chosen because it was easy to observe the edge of the sample in all of the radiographs. These edges were highlighted with white lines in the magnified images, except the border after being exposed to isopropyl alcohol was shown in orange.

The radiograph data indicate that after 2.5 h of hydration at 50 ºC, the particle boundary has expanded by at least 1.3 μm due to the formation of hydration product on the surface of the particles (see Fig 4.3). In addition, the sample border closely matched the images from before (white dotted-line) and after (orange line) the sample was exposed to isopropyl alcohol. Furthermore, the interior structure of the sample does not appear to change qualitatively. This suggests that the exposure to isopropyl alcohol did not significantly damage the microstructure of the sample. This finding supports the work done by others [108,109], while also providing additional data at the nanoscale. It appears that the hydration products in these images were not impacted but it is possible that, if the material was exposed to isopropyl alcohol at earlier times, the more delicate structures might be altered. This is an area for further investigation.

4.4.2 Changes of internal structure at different hydration times

Fig 4.4 shows radiographs of Sample 1C after two hours of hydration at 25 ºC. The particle boundaries before and after hydration closely match each other. The slice images show that the perimeter of the particle is growing and the surface of the C_3S seems to been modified. These changes caused noticeable textural difference between the radiograph images before and after hydration, as shown in Fig 4.4. This may be caused by etching of the C_3S particle. The very

small amount of perimeter change from the individual images compared well with the observations made in Table 4.2 which showed overall small dimension and volume changes for the Sample 1C. According to the calorimetry curve in Fig. 1, these changes are occurring during the induction period.

In contrast, Sample 2C was hydrated just 30 min longer in the same conditions and showed an estimated 16 % increase in volume (Fig 4.5). According to the calorimetry curve, this time (2.5 h) corresponds with the beginning of the acceleration period, although there may be differences caused by settlement. The overall dimensions of the sample were almost the same (or showed very slight decrease), but the x dimension decreased about 0.8 μm. This decrease in dimension was likely caused by dissolution. The large increase in volume was caused by the formation of hydration products between two C_3S particles that are about 2 μm apart (see the bottom figures in Fig 4.5). One C_3S particle near the top of the image was approximately 4 μm in diameter and has changed greatly in gray value. This could be caused by dissolution of the particle accompanied by formation of hydration products in this same region [95].

Fig 4.6 shows the inner structures of Sample 3C before and after 2.5 h of hydration at 50 ^{o}C. Based on the calorimetry curve in Fig 4.1, this sample was in the middle of the acceleration period. The locations of slices were selected based on the same locations of the fiducial markers. This marker provided a convenient location to make a comparison in both scans. The border of the sample is shown in orange before and after hydration. The border of the C_3S particle before and after hydration is shown in white in the bottom images. There is some material between the particles with a lower gray value than the C_3S particles. This material is likely epoxy from the sample preparation. The images after hydration show a substantial growth of hydration product and the dissolution of the C_3S particle. Table 4.2 shows that the dimensions of the sample increased by 50 % and the total volume increased almost fourfold. The large volume change at

this time period is attributed to the higher temperature, and hence more rapid hydration, of this sample compared to the others during hydration.

The radiographs and tomography slices of sample 4C after seven hours of hydration are shown in Fig 4.7. Based on the calorimetry curves in Fig 4.1, this sample is in the middle of the acceleration period. Mosaic tomography was used to construct these images because this sample is larger than the scanning window. A 3D model gives the overall distribution of these materials where the hydration product has been made transparent to show the internal particle boundary. These images show that the hydration product has not formed uniformly around the particles. This could be caused by different sides of the sample having different surface areas, concentration defects, or exposed crystal planes. Over the seven hours of hydration, this sample showed a decrease in C_3S volume of only 6 % and a growth of hydration products that is almost 4.5 times the size of the original C_3S particles. The images show that hydration product formed between the particles has a higher gray value than the material formed near the edges of the particle. These regions are labeled “high X-ray absorption” and “low X-ray absorption”. This suggests the hydration product is not homogeneous and will be discussed in the next section. Sample 5C is a replicated sample with the same hydration period with a similar amount of growth in dimension and volume. Details are provided in Table 4.2. More details of this sample are provided in the Appendix B.

4.3 The quantitative analysis of the heterogeneity of hydration product

The difference in gray value indicates different X-ray absorption. According to equation (1) this relates to localized differences in chemistry, density, or both. To quantify this variation the average gray values at different distances away from the anhydrous C_3S particle were measured. Nested shells with thickness 0.6 μm were created that follow the outside border of the anhydrous C_3S particle; each shell was built on the previous one until the outside of the particle was reached.

An example of 2D and 3D cross-sections through the shells is shown in Fig 4.8. The average gray value for each shell is then plotted versus the distance from the surface of the remaining C_3S particle. For reference, markers have been added that show the average gray values for air, C_3S, and hydration product.

These data show that there are hydration products with different X-ray absorption coefficients at different distances away from the surface of the anhydrous C_3S particles. On average, the hydration products within about 1 μm of the surface of the anhydrous C_3S have higher X-ray absorption coefficients than other regions. This means that even though a significant volume of hydration products are shown in Table 3, the hydration products do not have a constant chemistry and/or density. This difference in chemistry and/or density matches previous reports in the literature [93-95]. This finding confirms the presence of very low X-ray absorption and likely low-density hydration products that have been suggested by others based on observations from SEM and neutron scattering [74,116]. However, this work provides much more quantitative information than previous techniques. The high X-ray absorption area between the particles may be more representative of hydration products that form within closely spaced cement paste and the lower X-ray absorption areas may be more representative of products in water-filled spaces.

4.4 Chemical Variation of Hydration Products

Sample 4C, hydrated for 7 h at 25 °C, was also investigated with nXRF. The raw elemental maps for Ca and Si are given in the first row of Fig 4.9. The unit of concentration, μg/cm2, measures the mass of elements over the depth within a unit area. An additional map of the molar Ca to Si ratios shows the variation of the elemental composition. Regions of C_3S, CH, and hydration product are shown in the second and third rows of Fig 4.9. The regions of C_3S are determined from the aligned nCT and nXRF data. The elemental Ca map shows that there are regions of high Ca concentration at the top and bottom of the sample with Ca/Si > 15. This suggests that these

regions are likely a mixture of CH and C-S-H with larger amounts of CH. These regions dominated by CH were segmented by using a Ca threshold concentration greater than 250 $\mu g/cm^2$. The remaining material has been labeled hydration product with higher proportion of C-S-H. The mean and standard deviations of the chemistry for each region is given in Table 4.4.

Regions within and near the surface of C_3S were also investigated and are shown as regions A through D in the second and third rows of Fig 4.9. These regions were chosen to minimize the artifacts from X-ray absorption of the materials. Region A is representative of hydration products found close to the particle surface and Region B is representative of hydration products found at least 1.6 μm from the C_3S surface. The anhydrous C_3S was investigated because this material is expected to have a predictable chemistry. Region C has a Ca/Si of 3 as expected, but region D had higher amounts of calcium and lower amounts of silicon, indicating a Ca/Si of 3.71.

This higher Ca/Si in region D was not expected. However, a nXRF measurement is the average X-ray fluorescence from the material along the path of the beam. It is possible that hydration products containing Ca or Si had formed around region D and that the chemistry of these materials changed the nXRF measurement. To further investigate this, the sample was rotated by 90^o and measured again. This showed that the anhydrous C_3S in region D was surrounded by CH and region C was not. Images are included in the supplementary section. This supports the hypothesis and confirms that the measurement in region D was coming from both the underlying CH and the C_3S particle. This highlights how interpretation of nXRF data can be challenging if the distribution of constituents is not known a priori.

Next, we analyzed the hydration product both within 1.6 m of the C3S surface (region A) and further away (region B). The calcium concentrations were found to be similar; however, the mean silicon concentration of the hydration product within 1.6 μm is twice that of the hydration products found further away. The silicon concentration of region A is 14.1 ± 4.4 $\mu g/cm^2$

compared to 7.1 ± 2.0 μg/cm^2 in region B. These measurements reflect the average and standard deviation. This difference in chemistry contributes, along with any differences in density, to the variations in gray value of the hydration products shown in Fig 4.8.

Since C-S-H is a nonstoichiometric solid with a variable Ca/Si, the C-S-H chemistry will depend on the chemical potentials of the calcium and silicate components in solution when the hydration product is formed. Silicate ions have a lower mobility in solution than calcium ions, which could contribute to the observed differences in composition as a function of distance from C_3S. This difference in silicate chemistry over 1.6 μm away from the surface may define a critical diffusion length for silicon in this system.

The Ca/Si in both region A and B are greater than the values typically reported in the literature with SEM-EDS and C-S-H solid in solution [72,74,76,89-93,117,118]. These increased Ca/Si values are likely caused by contributions from both CH and C-S-H lying along the X-ray absorption length, similar to the mixture of CH and C_3S observed in region D of the anhydrous C_3S. It is also possible that the CH and C-S-H are intimately mixed, as suggested in past literature [73,81,94].

4.4.5 Comparison of nXRF with SEM EDS

To support the measurements from the nXRF, sample 4C was examined by SEM at the same orientation as was used for the nXRF measurements. A sample of anhydrous C3S was also included. These experiments were done to give a comparison between nXRF and SEM-EDS. Results from the surface chemical analysis with standardless EDS are given in Table 4.5. The Ca/Si values for the C_3S are near 3 as expected. Points measured in Region A of Fig 4.9 show comparable Ca/Si to those from the same region measured by nXRF. The Ca/Si ratios in Region B are much higher than those in Region A. This matches and lends further support to the measurements made by nXRF in the same regions.

Some differences in the measured SEM EDS from expected values may reflect the combined effects of the standardless EDS analysis and using surface measurements instead of flat polished samples. More refined measurements were not made because the sample was too delicate for additional sample preparation and the goal was to show a comparison between nXRF and SEM-EDS.

4.4.6 The evolution and nature of the observed hydration product

These experiments show that neither C_3S dissolution nor hydration product growth occurs uniformly over the particle surfaces by the end of the slow reaction period. Enhanced growth of hydration products was observed between closely spaced C_3S particles during the beginning of the acceleration period. Hydration product was found to bridge particles that were as far as 2 μm apart. This localized formation of hydration products may be caused by higher concentrations of ions found near the surfaces of these closely spaced particles. Hydration products also seem to preferentially form on certain regions of the particles. This may be caused by increased surface area, mechanical damage from grinding, or other crystalline defects. This is an area of future research. As the acceleration period continues, the hydration products found within 1 μm to 1.6 μm seem to have a higher X-ray absorption and contain higher amounts of silicon compared to the hydration products found further from the surface of the anhydrous C_3S.

4.5 Conclusion

This paper highlights the utility of using nCT and nXRF to measure the 3D structure and chemistry of the early hydration of C_3S at 15 nm and 150 nm length scales. The hydration of triclinic C_3S particles in 15 mmol/L lime solution at w/s = 5 was examined as a function of time and temperature. The volumetric growth and variation of X-ray absorption and chemistry has been measured and will serve as a useful bench mark for future experiments and simulations.

The following observations were made for hydration at 25 ^oC:

- At the beginning of the acceleration period, some C_3S particles that were approximately 4 μm in diameter showed significant changes, while other particles of smaller size show only limited changes.

- Hydration product was observed to form between particles that were about 2 μm apart but not in other parts of the sample.

- For samples near the middle of the acceleration period, the volume of hydration products was over 4 times the original volume of the particles within the field of view. The hydration products within about 1 μm of the anhydrous C_3S surface had a higher X-ray absorption.

- During this same time period the hydration products within 1.6 μm of the anhydrous C_3S had twice the Si concentration as hydration products found further from this region.

The following observations were made for hydration at 50 °C:

- Solvent exchange using isopropyl alcohol showed minimal disruption of the microstructure for a sample hydrated for 2.5 h.

- Samples that were cured at 50 °C showed more rapid reaction and a higher volume of hydration than those at 25 °C.

Additional work is underway to investigate other solutions and materials. Improvements are also being made to the measuring techniques to gain even greater insight into the hydration mechanisms.

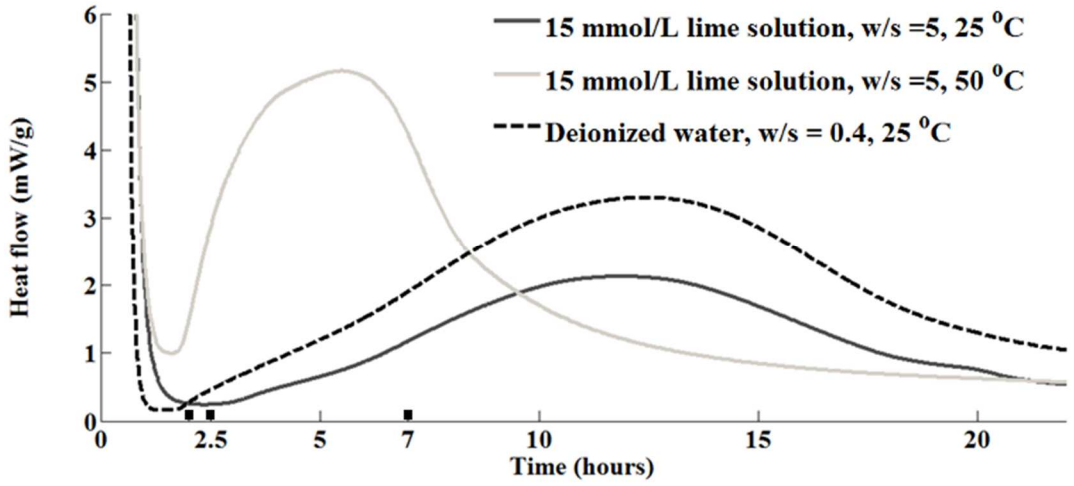

Fig 4.1 – The heat flow from isothermal calorimeter for C_3S, in mW/g of C_3S based on a single measurement. The bars labeled on the X-axis of the calorimetry curves show the time periods of hydration used in the imaging experiments.

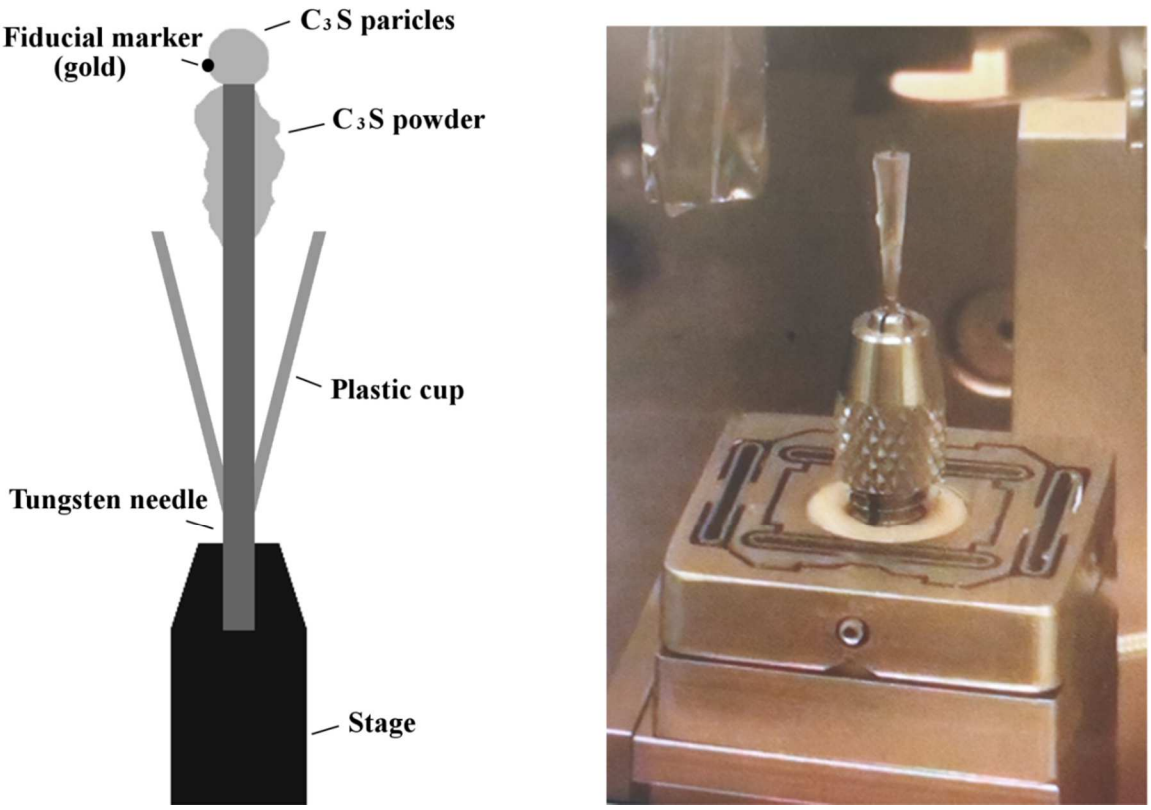

Fig 4.2 – An overview of the experimental setup (left) and the assembled setup on the beam line (right).

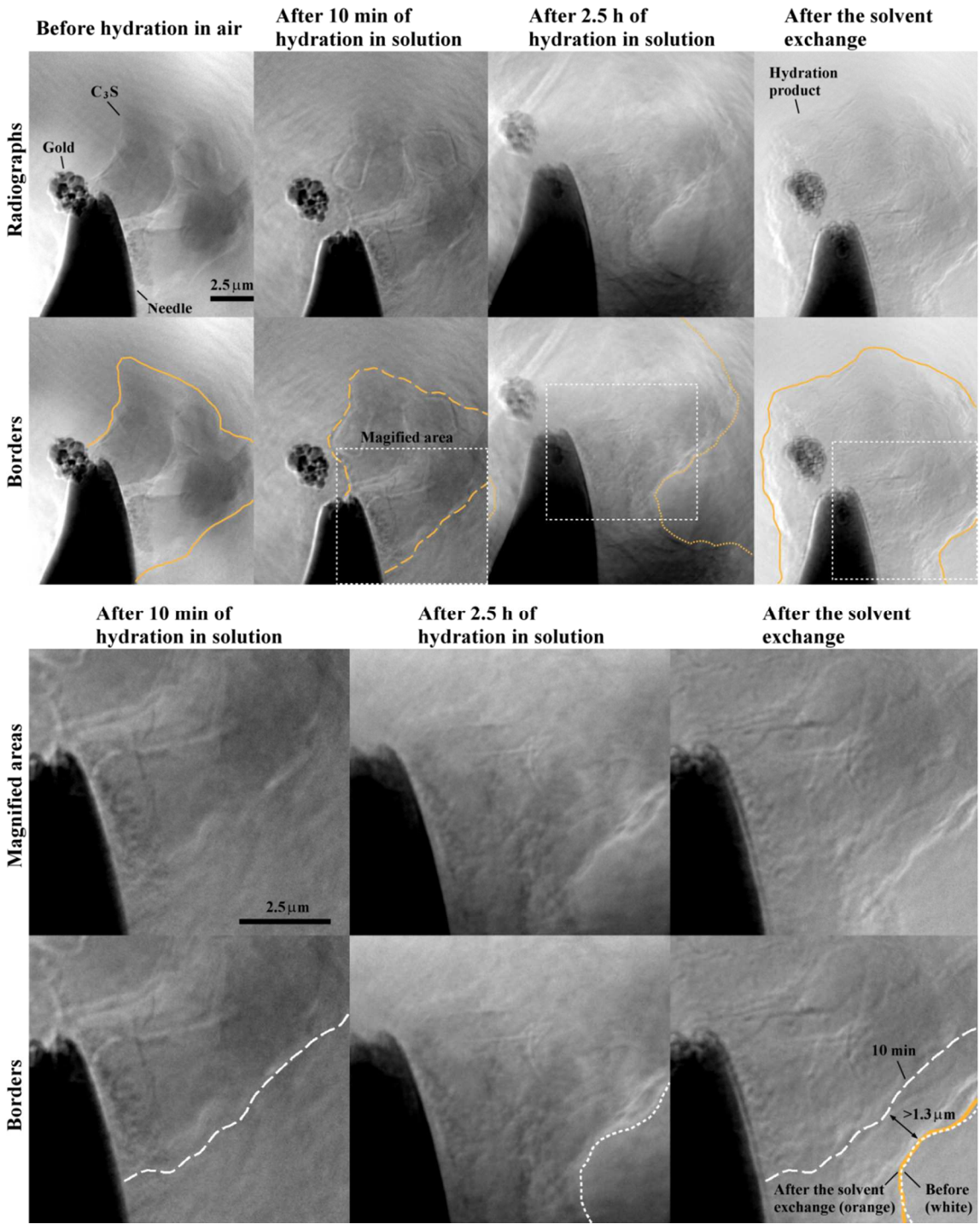

Fig 4.3 – Radiographs of sample 3C before hydration imaged in air, after 10 min and 2.5 h in 15 mmol/L lime solution at 50 °C, and then after the hydration has been stopped with isopropanol. The magnified areas from the last three stages are zoomed in and shown at the bottom with the

borders highlighted. The borders at the stage before and after soaking in isopropyl alcohol closely match.

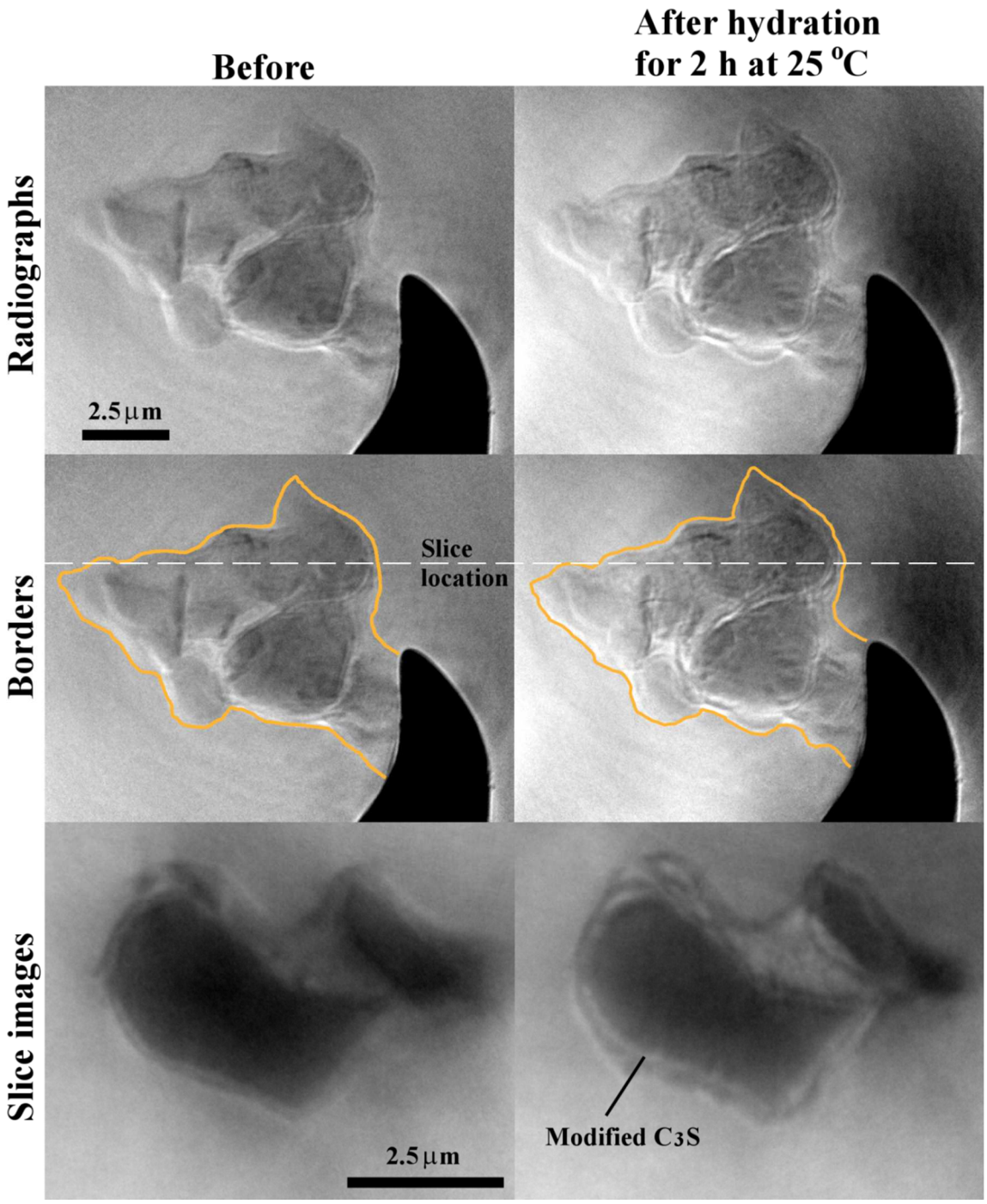

Fig 4.4 – The radiographs and tomography slices of Sample 1C before and after hydration for 2 h at 25 °C.

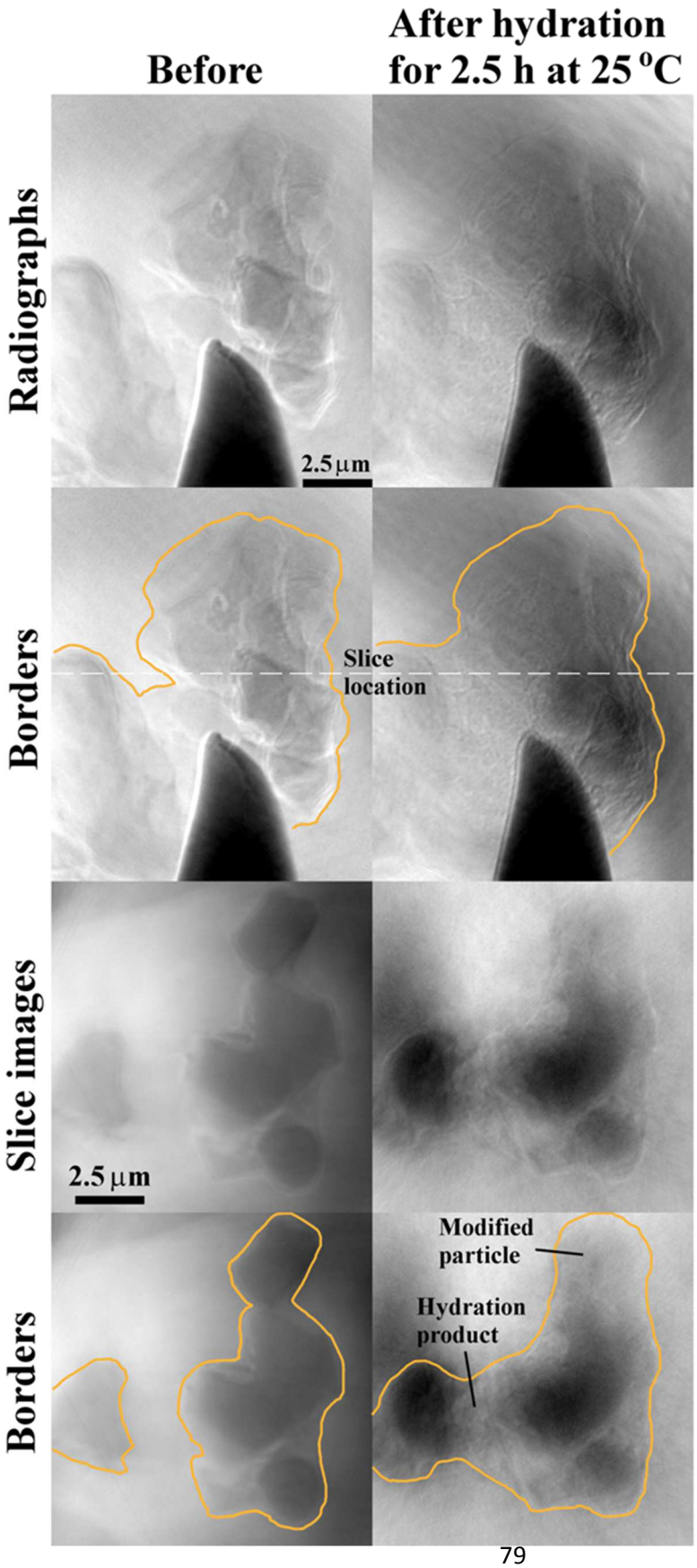
Before
After hydration for 2.5 h at 25 °C
Radiographs
2.5 µm
Borders
Slice location
Slice images
2.5 µm
Borders
Modified particle
Hydration product

Fig 4.5 – The radiographs and tomography slices of Sample 2C before and after hydration for 2.5 h at 25 ^{o}C.

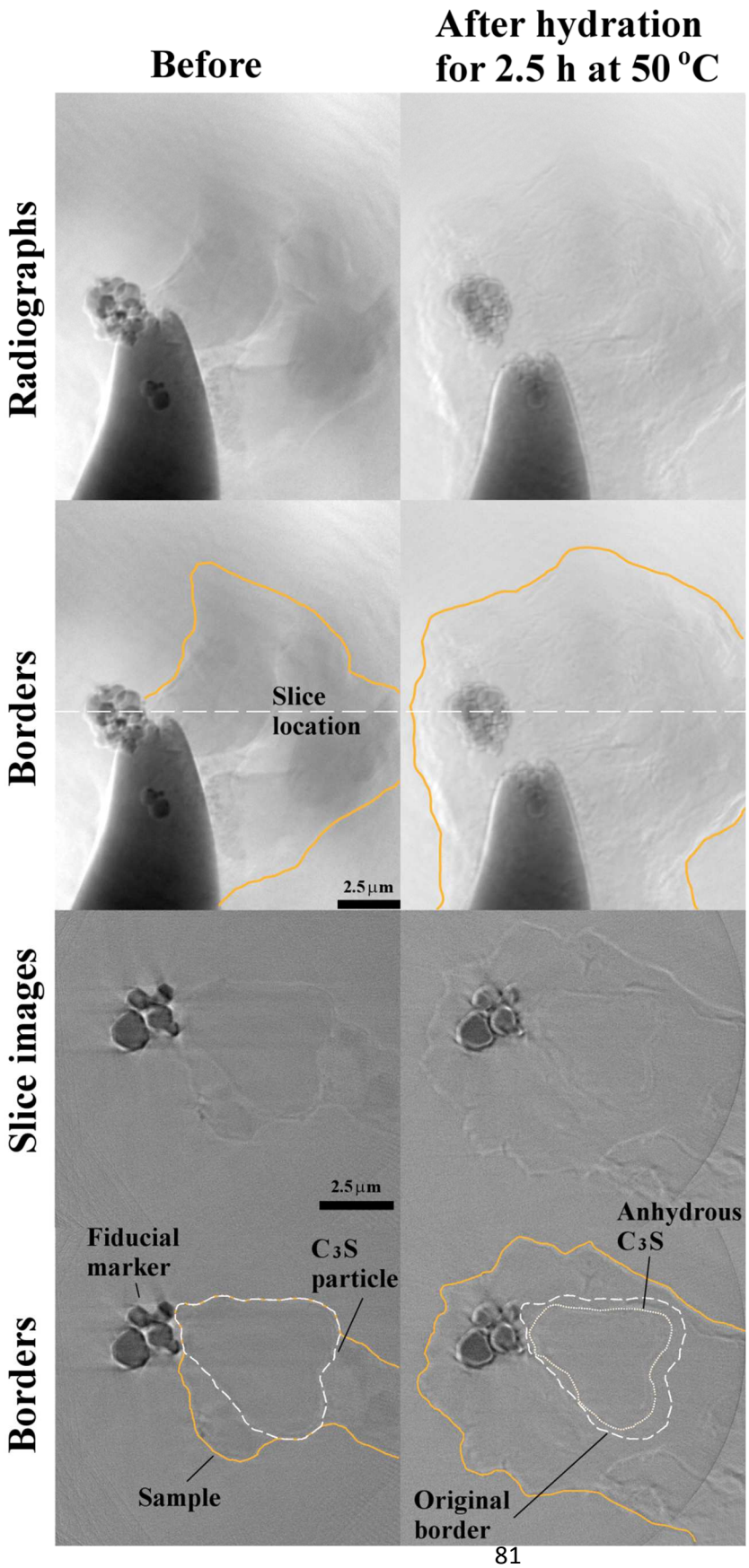
Before
After hydration for 2.5 h at 50 °C
Radiographs
Borders
Slice location
2.5 μm
Slice images
2.5 μm
Borders
Fiducial marker
C3S particle
Sample
Anhydrous C3S
Original border

Fig 4.6 – The radiographs and tomography slices of Sample 3C before and after hydration for 2.5 h at 50 ^{o}C. In the tomography slices, the borders of one C_3S particle are highlighted as white dash line in both hydration stages (the fourth row).

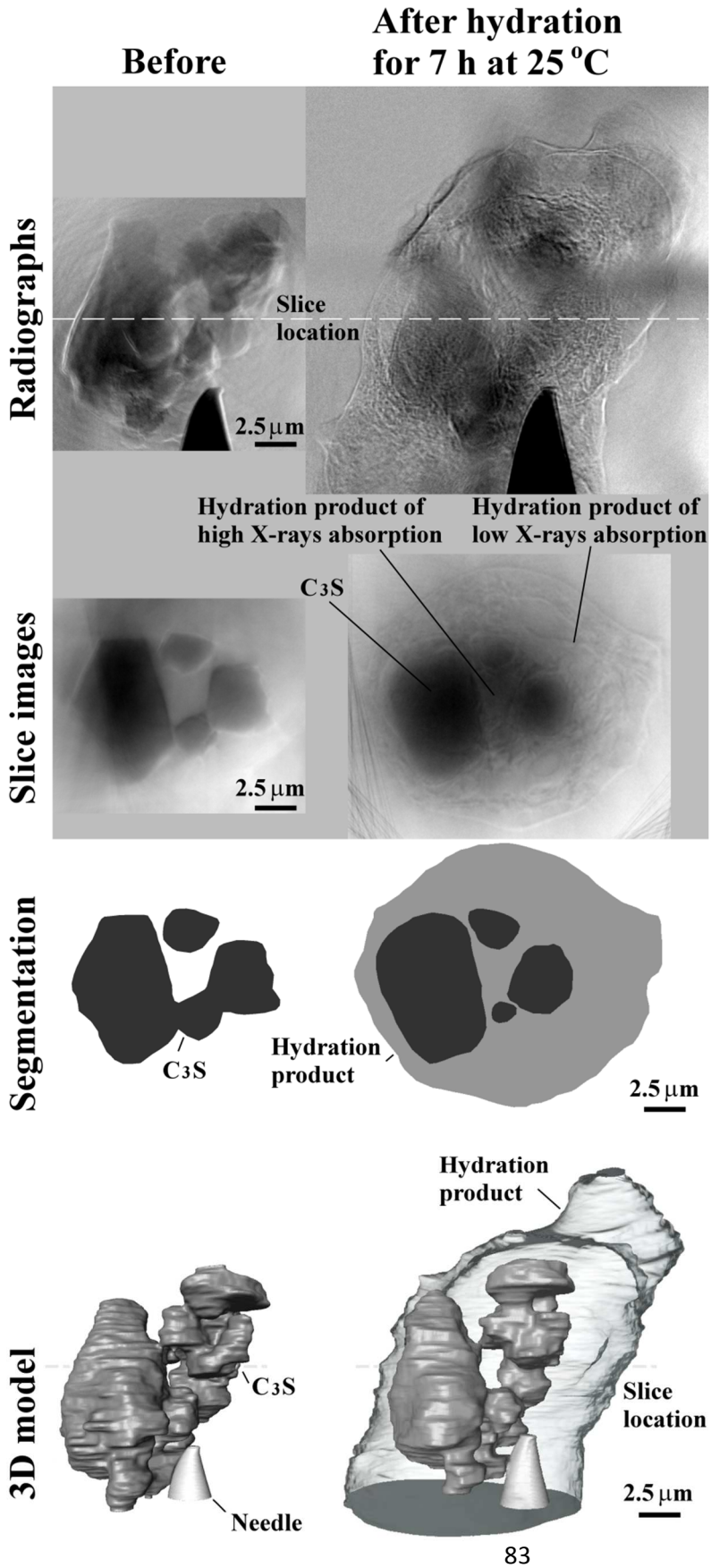
Before
After hydration for 7 h at 25 °C
Radiographs
Slice location
2.5 μm
Hydration product of high X-rays absorption
Hydration product of low X-rays absorption
C3S
Slice images
2.5 μm
Segmentation
C3S
Hydration product
2.5 μm
3D model
Hydration product
C3S
Slice location
Needle
2.5 μm

Fig 4.7 – An overview of the results of sample 4C: radiographs, tomography slices, segmentation on slice images and 3D model.

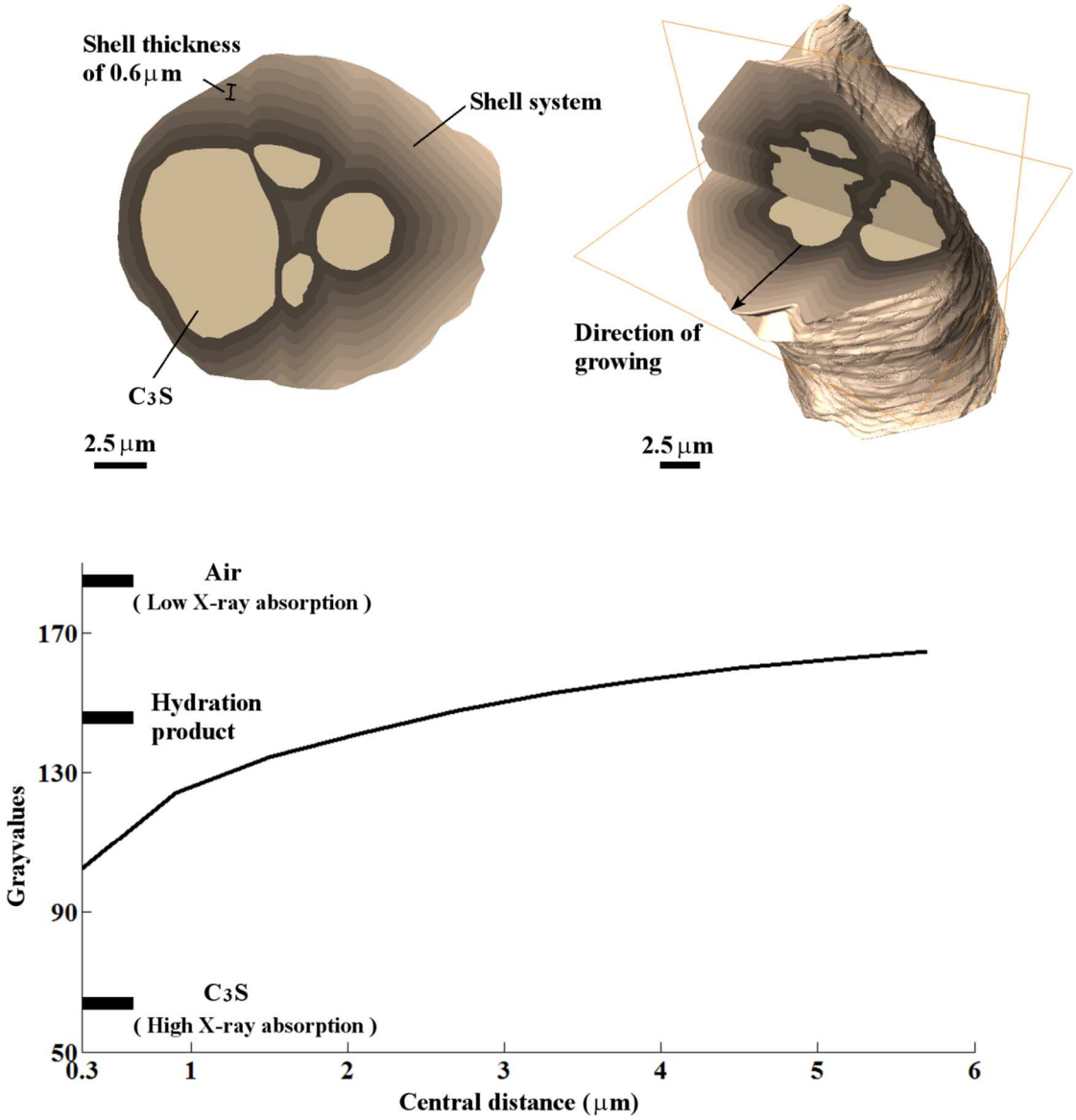

Fig 4.8 – Uniformly thick shells for the 2D and 3D system, and the plot of the mean gray values of the shells versus their central distances from the C_3S particle surfaces.

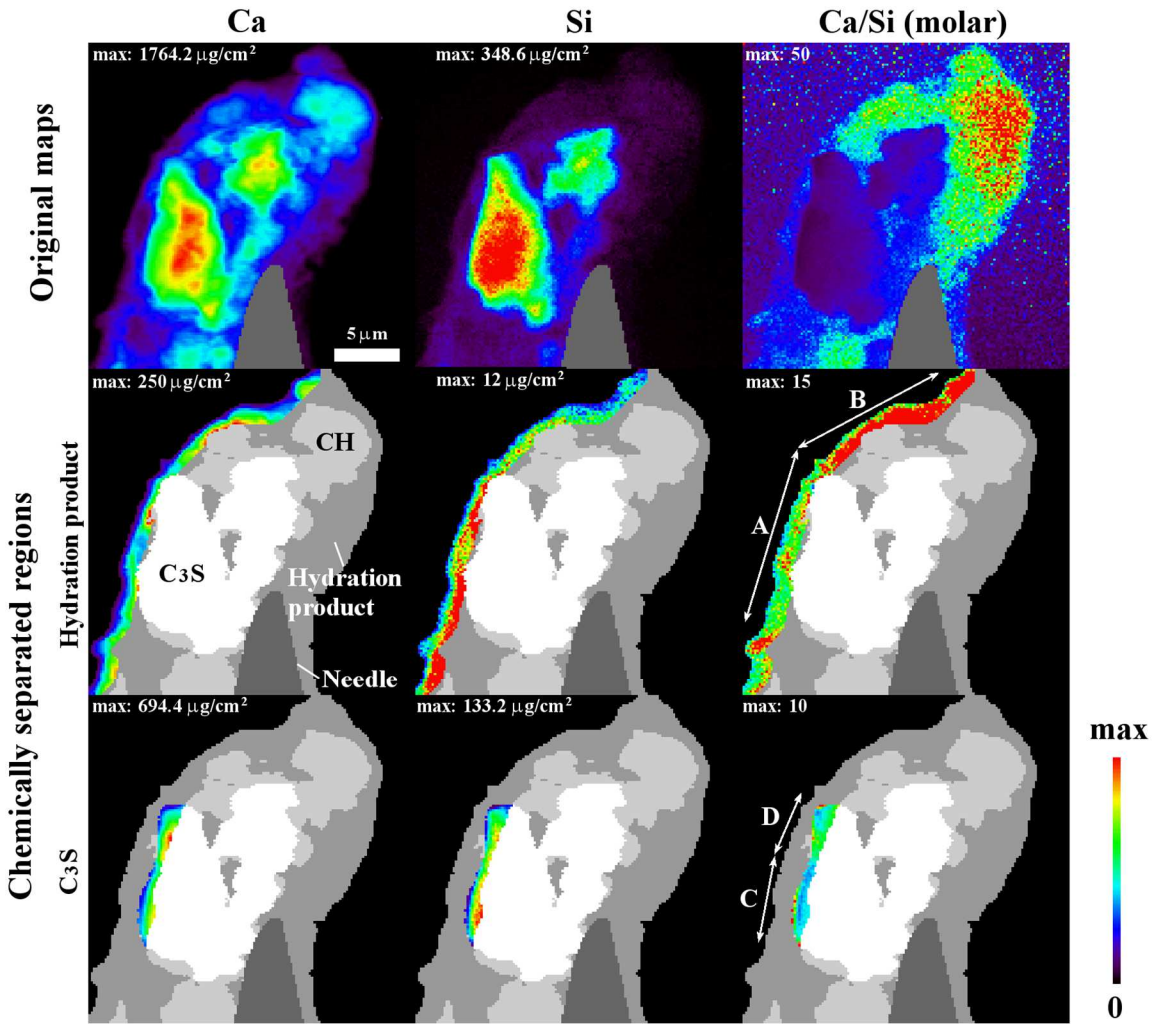

Fig 4.9 – The elemental composition of sample 4C from nXRF analysis. The raw maps for Ca, Si and molar Ca to Si ratio are given in the first row. Quantitative analysis is given from a 1.6 μm thick band for hydration product and 3 μm for C_3S as this material will have minimal X-ray absorption. Segmentation map is shown in the second and third rows. The bands were divided into regions A and B for hydration product and regions C and D for C_3S.

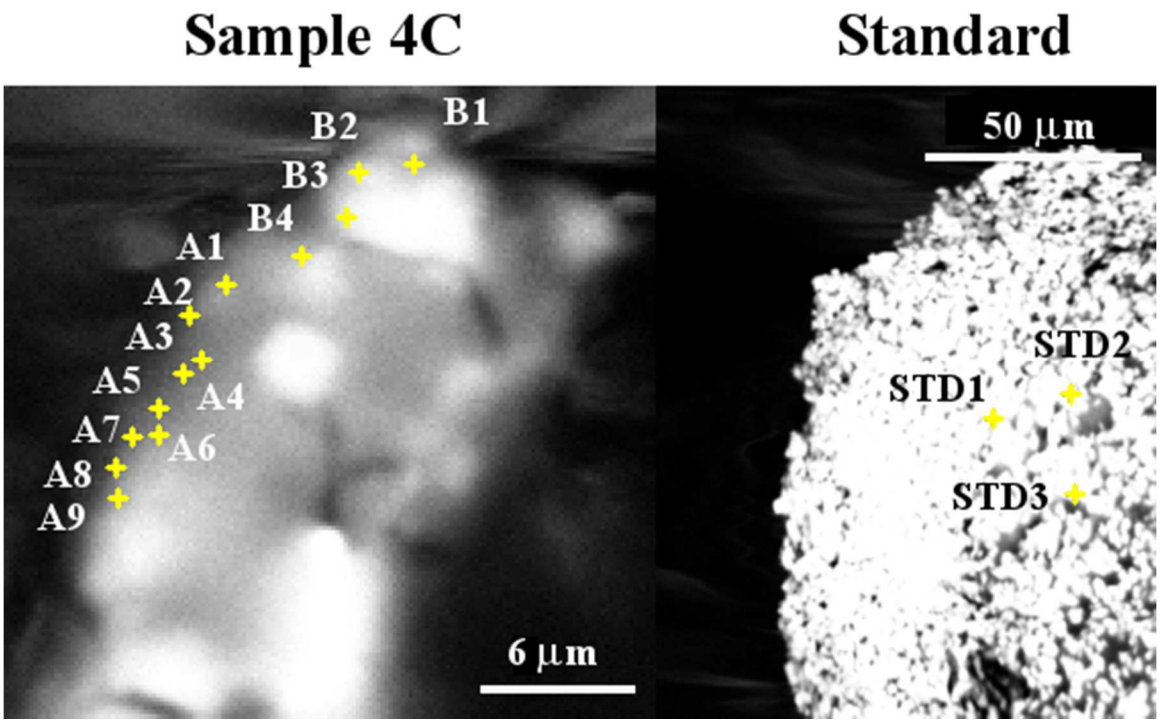

Fig 4.10 – The backscattered electron images of sample 4C and standard sample. Points, A1 to A9 and B1 to B4 from the regions A and B in Fig 4.9 respectively and Points, STD1 to STD3, from the standard sample as anhydrous triclinic C_3S were investigated by EDS with the results given in Table 4.5.

Table 4.1 – The elemental composition based upon a single analysis and the surface area of C_3S based on three analysis. An uncertainty in the surface area measurement of one standard deviation is given.

ICP Elemental analysis	Al	Ca	Mg	Si	Sr
(mole %)	<0.2	74.8	<0.002	25	0.018
BET surface area (m^2/g)	1.2156± 0.0028				

Table 4.2 – The dimensions and volumes of the samples before and after hydration based on a single measurement.

Sample name and scans		Time (h)	°C	dim-x (μm)	dim-y (μm)	Height (μm)	Volume (μm^3)		
							C_3S	Hydration product	Total
1C	before	2	25	6.53	9.23	4.76	82.40	0	82.40
	After			6.47	9.12	4.71	82.73		82.73
2C	before	2.5	25	14.24	11.99	7.98	269.26	0	269.26
	After			13.46	11.64	7.725	311.58		311.58
3C	before	2.5	50	8.36	13.22	4.74	101.77	0	101.77
	After			12.59	11.31	7.47	378.58		378.58
4C	before	7	25	11.97	14.60	10.74	593.96	0	593.96
	After			23.28	23.31	17.1	561.09	2611.15	3172.25
5C	before	7	25	9.68	9.84	5.06	108.69	0	108.69
	After			21.06	22.74	20.76	4011.09		4011.09

Table 4.3 – The instrument settings for, nCT, nXRF, SEM and EDS experiments

nCT	Resolution		15.6 nm/pixel
	Exposure time		6 s
	Source energy		8 kev
	X-ray magnification		x83
	Optical magnification		x10
	Dynamic ranges[a]	min	-5000
		max	5000
nXRF	Resolution		150 nm/pixel
	Detector dwelling time		0.1 s
	Scaler count time		0.1 s
SEM[b]	Spot size		40%
	Accelerating voltage		≈20kV
	Filament drive		75 %
	Emission current		≈50 μA
	Pico-amp meter reading		1.15 -1.20 nA
	Brightness		-15 %
	Contrast		90 %
	Magnification		2500×
	Working distance		17 to 18 mm
EDS	Minimum counts per second		3500
	Live time (acquisition time)		5 s

[a]: the data are displayed in FLOAT type
[b]: backscattered imaging mode

Table 4.4 – Ca and Si concentrations and uncertainties expressed as a single standard deviation for hydration product and C_3S in the chemically separated regions from nXRF.

Elements	Hydration product		C_3S	
	A	B	C	D
Ca ($\mu g/cm^2$)	159.6±36.6	145.8±36.5	343.1±119.0	378.4±141.2
Si ($\mu g/cm^2$)	14.1±4.4	7.1±2.0	80.6±33.9	71.4±25.8
Ca/Si (molar)	8.0±3.1	14.4±5.5	3.0±1.8	3.7±1.9
number of measurements	549	613	161	172

Table 4.5 – The summary of elemental composition expressed as mass percent and uncertainties as a single standard deviation from EDS analysis of the points labeled in Fig. 4.10.

	Point #	Elements (mass %)				Ca/Si (molar)
		Ca	Si	O	Al	
Region A	1A	58	9	29	3	5
	2A	55	5	35	4	8
	3A	55	5	35	3	7
	4A	57	5	33	3	7
	5A	57	7	32	3	6
	6A	54	6	35	4	7
	7A	58	8	31	3	5
	8A	60	8	29	2	5
	9A	60	8	29	2	5
	Ave ± std	57±2	7±2	32±3	3±0.5	6±1
Region B	1B	79	1	19	0	51
	2B	69	1	28	1	43
	3B	68	0	29	2	Inf
	4B	57	3	34	5	13
	Ave ± std	68±9	1±1	27±6	2±2	>36±22
C_3S	STD1	62	14	24	0	3
	STD2	63	14	23	0	3
	STD3	65	15	20	0	3
	Ave ± std	63±2	14±0.4	22±2	0	3

CHAPTER V

IN-SITU MEASUREMENTS OF STRUCTURE, CHEMISTRY AND MASS DENSITY OF C_3S DURING THE INDUCTION PERIOD

Abstract

The reasons for the start and end of the induction period remain a mystery in cement hydration. One long-standing hypothesis is the importance of early hydration products on the surface of cement particles. However, because this material is not widely observed in experimentation the importance of this material has been questioned. In this work, a combined analysis of nano-tomography and nano-X-ray fluorescence makes the direct imaging of early hydration product possible. These novel X-ray imaging techniques provide quantitative measurements of 3D structure, chemical composition, and mass density of the hydration product during the induction period. This work does not observe a low density product on the surface of the particle, but does provide insights into the formation of etch pits and the subsequent hydration products that fill them.

Keywords: Induction period, C_3S hydration, C-S-H, Microstructure, Nanoscale

5.1 Introduction

The dissolution of tricalcium silicate (C_3S) and subsequent formation of hydration products are important processes that have been hypothesized to control the induction period of hydration of Portland cement [65,119]. The induction period is of practical significance as it gives time for the concrete to be transported and cast into the desired shape. Although C_3S dissolution has been extensively studied for over a decade, there is still widespread disagreement on the basic mechanisms due to a lack of sufficient detailed observations, especially of direct, in-situ evolution of the microstructure of the C3S surface and the hydration products [65,69,79,119,120].

Recent publications have emphasized the importance of geochemical dissolution theory in the induction period [86,121-123]. Initially, when the undersaturation of ions is high, material is proposed to dissolve rapidly at surface defects such as screw dislocations, leaving an etch pit [121,122]. Later, as the ion concentration increases and the undersaturation decreases, the driving force for dissolution is evidently too low to sustain the unwinding of the etch pits, so dissolution may switch to a slower but more uniform step flow mechanism. Recent experimental work supports these ideas [79,80,87,124-126]. The uneven reaction on alite grains has been reported using scanning transmission electron microscopy (STEM) after two hours of hydration [79]. This preferential reactivity relates to the density of etch pits on the grains. From another pure dissolution experiment under a highly undersaturated solution flow on a polished section of a C_3S sample, the reaction has been found to cause irregular morphological changes on the polished surface [125].

The formation of etch pits is suggested to be related to the high density of crystallographic defects, mechanical damage or other disorder in the crystal structure [80,121]. These defects on some anhydrous C_3S particles have been imaged using TEM [80]. The impact of the density of defects on the induction period has also been confirmed by studying the same C_3S material before

and after annealing using calorimetry [80,126]. However, calorimetry experiments measure bulk heat release and do not provide insights into the details of the hydration product formation and dissolution process [127-131].

The formation of early age hydration product could impact the dissolution process. The exothermic behavior during the induction of C_3S hydration observed using high-resolution differential calorimetry suggests that there is an early formation of hydration products over that period [129]. This early hydration product has been suggested to be a metastable phase, which could account for the slow hydration of C_3S at this early period [128]. Recent experimental work has found that the pure dissolution of C_3S in the absence of any precipitate shows much higher dissolution rate than the same material in a diluted suspension that promotes the formation of hydration products [131]. These results suggest that early hydration of C_3S may be restricted by other mechanisms besides its pure dissolution, namely the presence of hydration product.

To better understand how hydration product is involved in the dissolution process, it would be helpful to have an experimental technique that could track the location, density, and chemical composition of the dissolution sites and hydration products. Scanning electron microscopy (SEM) and transmission electron microscopy (TEM) have been widely used to study the early age microstructure during the induction period [79,80,87,121,124,125]. The hydration product is typically classified in terms of inner product or outer product, based on its location relative to the original boundary of the cement grain and the perceived differences in density or composition [132-134]. These early hydration products are typically found to have varied density and chemistry with a molar Ca to Si ratio (Ca/Si) typically between 1 and 2, with a value of 1.7 commonly reported [79,81,83,128,130,134]. However, SEM and TEM imaging are not able to easily determine the location of the original surface of the anhydrous particle and so this classification based on location can be challenging to determine with these techniques.

In-situ soft X-ray microscopy has been used to capture time-lapse transmission images while C_3S is reacting at an average water-to-solid (w/s) ratio of five [95]. The results provide insight into the changes in structure of the original particle and the surrounding hydration product, but image analysis is challenging because the 3D dataset is projected onto a 2D transmission image. This is similar to the radiographs shown later in this paper. The soft X-ray microscopy experiments show that in the presence of an accelerator, such as $CaCl_2$, the reaction of C_3S could form inner product to maintain the overall boundary of the particles during the early hydration period [95]. This inner product is less dense than the hydration products observed from the solution without $CaCl_2$ by comparing their X-ray absorption. However, detailed information about the chemical composition and density of the inner product material cannot be obtained by this technique.

Recent advances with synchrotron hard X-ray nanoprobes have allowed X-ray nano-computed tomography (nCT) and nano X-ray fluorescence to (nXRF) to become a reality. In addition, lab scale X-ray tomography instruments are able to achieve quite comparable measurements. These techniques are capable of non-destructively imaging at the nanoscale. The sample preparations for these techniques are minimal and so lend themselves to evaluating processes that change over time. These techniques can also be combined with other chemical mapping techniques or other experimental methods and the results can be used as a starting point for or as a comparison to computer simulations [23,49,57,97-100,135].

X-ray computed tomography (CT) is commonly used in the medical sciences to non-destructively image the internal structure of organisms. This technique combines a series of X-ray radiographs at small angles of rotation to produce a 3D model or tomograph [16,18]. The X-ray absorption contrast of the materials as a function of density and chemistry permits extraction of 3D structural information [54,101,102]. New lab-scale nCT systems that can use X-ray imaging energies as low as 5.4 keV have been developed. These lower X-ray energy levels provide sufficient

transmission and improved contrast for cementitious and geologic materials; however, their imaging times are often longer than those at the synchrotron.

The nXRF technique uses a focused X-ray beam to illuminate a sample. Each chemical element fluoresces at characteristic energies along the path of the beam. An energy dispersive detector measures the fluorescence X-rays emitted by the sample. By rastering the primary X-ray beam over the sample it is possible to create 2D maps of its composition [97,99,105]. This technique can provide elemental maps with detection limits better than a part per million (ppm). One challenge with nXRF is the interaction volume of the X-ray beam with the sample, the extent of which is not well known. This means that the measurements are reported in terms of the elemental concentration only divided by the area of the beam without considering the length of each path of X-ray. As shown in previous publications, the combination of nCT and nXRF can be used to overcome this limitation. When combined in this fashion, the technique has been named nano-tomography assisted chemical correlation (nTACCo) [97].

In this paper, nCT was used to image individual C_3S particles with sizes from 2 μm to 5 μm before and after 2.5 h of hydration and to make direct comparisons at different hydration times. The 3D microstructure datasets showed the reactions of these particles at their surfaces and in their interior. Two particles were analyzed by nTACCo, from which the chemical composition and mass density of the different regions of the reacted particles were identified. These results provide new insights into the dissolution and formation of early age hydration products and their role in the induction period.

5.2 Methodology

5.2.1 Materials

The triclinic C_3S used in this study was manufactured by Mineral Research Processing (Meyzieu, France). This material was characterized with inductively coupled plasma optical emission spectroscopy (ICP-OES) for elemental composition, X-ray diffraction (XRD) for crystalline phase abundance, automated scanning electron microscopy (ASEM) on the dispersed powder for particle size distribution (PSD), multi-point nitrogen adsorption isotherms (BET) for specific surface area, and isothermal calorimetry for average hydration rates in water. The results from ICP-OES analysis and BET are shown in Table 1 and the calorimetry measurements are shown in Fig 5.1. The XRD analysis indicates this material is close to pure triclinic phase (T3). The PSD measured by ASEM using 4000 individual particles suggests that 95 % of the particles are between 1 μm and 7.5 μm in characteristic linear dimension. One sample in the calorimetry experiments used a 15 mmol/L lime solution with w/s = 5 to replicate the conditions of the experiments in this paper. Another sample of w/s = 0.40 reacted with deionized water was used to study the performance of this material at an industrially relevant w/s. A time period of 2.5 h is highlighted on the X-axis as a black wide bar. This is the time period used for the imaging experiments. Some sedimentation (bleeding) could occur in the sample with w/s = 5 during the experiment, but the results provide an average w/s that matches the nCT experiments. The details of these experiments are given in Appendix B.

5.2.2 Sample preparation and experimental steps

The sample was prepared by gluing multiple C_3S particles on the tip of a tungsten needle with Devcon 5 minutes epoxy as demonstrated in Fig 5.2. A plastic cone that fit tightly to the needle was used as a solution container. The cup has a small hole that allowed the needle to penetrate through it. The cup fit tightly to the needle and stayed in place due friction unless intentionally pulled up or down the needle. Additional C_3S powder was attached on the side of the needle to make the average w/s = 5 within the cone volume.

At the beginning of the experiment, an initial scan of the dry particle-needle configuration was made with the cup at the lowest location. Next, the sample was placed in an Airgas ultrahigh purity nitrogen environment and the cup was filled with 15 mmol/L lime solution. The cup was then raised to submerge the sample in solution. The sample was then sealed in the nitrogen environment to avoid carbonation and allowed to hydrate for 2.5 h. The seal was removed after the prescribed hydration time, the solution was removed, and the sample was submerged in 99 % isopropyl alcohol (IPA) for five minutes to arrest hydration. IPA was used because it has been suggested previously to have the least impact on the microstructure of hydrated samples [108,109]. Previous work with these same materials and techniques has indicated no observed differences in the microstructure before and after using IPA to stop hydration [136]. The cup was then lowered and the sample was placed back on the nCT scanner to obtain final tomography scan. nXRF scans were also completed on two of the single particles for subsequent nTACCo analysis.

A w/s of 5 was used because it allowed sufficient X-ray transmission for tomographic imaging. If pure water had been used, the mounted particle might have reacted too quickly to make meaningful measurements, so a solution containing 15 mmol/L of calcium hydroxide was chosen instead. Past research on microcalorimetry of continually stirred C_3S in lime solutions, confirmed by the data in Fig 5.1, showed little influence on the hydration rate for w/s from 0.5 to 5 [106,107].

5.2.3 nano-tomography (nCT)

The nCT scanner used in this experiment was a Zeiss 810 Ultra (Carl Zeiss X-ray Microscopy, CA, USA) with X-ray energy level of 5.4 Kev at the resolution of 65 nm per pixel. A detailed summary of the scan setting is given in Table 2. One nCT scan produces two different types of data sets. Radiographs are a measurement of the X-rays that pass through the sample. An

example of a radiograph is shown in Fig 5.3. A tomograph is created from the reconstruction of all the radiographs from multiple angles. One tomograph is a 3D data set that contains a number of 2D virtual slice images through the sample and example of which is shown in Fig 5.3. The grayscale value of a pixel represents the X-ray absorption of the material as a function of its local composition and density. With enough contrast, the segmentation of different phases can be made by the direct threshold of their gray values. This allows the 3D structure of the material to be rendered.

Because of the nanometric length scale of this experiment, any small shifting of the sample due to thermal expansion and imperfection of stage positioning could change the position of the sample in the nCT data sets. To compensate for these movements and allow the same region to be compared, the data from before- and after hydration scans need to be aligned. Usually, this alignment can be accomplished by using the mounting needle as a reference point. However, because individual particles may have independent movements that do not match the needle, these individual particles were first separated from the sample and then their data were aligned individually. A computer algorithm was developed to find a rigid-body translation and rotation needed to match the scans taken before and after the reaction. The algorithm is explained in supplementary information. Seven particles were investigated in this study, which were chosen because they could be found in the scan before and after hydration. An example of a data set for an individual particle is shown in Fig 5.4.

5.2.4 Depth of reaction

The depth of reaction of each particle was quantified by drawing a straight line from the reacted surface to the centroid of the particle. When this line reaches anhydrous C_3S, the distance is recorded and this determines the depth of reaction. With this technique, every voxel on the reacted surface provides an independent measurement of the reaction depth. A histogram for the

reaction depths was determined at 65 nm intervals. In addition, an alternative approach was also applied to measure the depth of reaction along the norm direction of the surface. The results give similar trends that match well with the former approach. The details of this second approach and results are given in the supplementary information. For the robustness and simplicity of the first approach, the values of the depth of reaction reported in this paper are all based on the measurement along the directions from the surface to the centroid.

To examine the distribution of reaction depth for every particle, the histogram for all the voxels on the reacted surface is plotted as the "Entire reacted surface" as shown at bottom of Fig 5.4. For some particles, the reactions are localized on some disconnected regions. These areas are selected as individual sites to plot their distributions separately in order to compare their depths to all regions. For some particles, the reacted regions contain zones of total dissolution. To quantify the depths of these totally dissolved regions, the same method is used by measuring the centroid distance from the original surface, but counting only the length within the totally dissolved regions.

5.2.5 nano-X ray fluorescence

The nXRF measurements were made with an X-ray spot size better than 50 nm at the hard X-ray nano-probe beamline at sector ID-26 of the Advanced Photon Source (APS) and the Center of Nanoscale Materials (CNM) at Argonne National Laboratory. The instrument settings are given in Table 5.2 and more details can be found in Winarski et al. [22].

X-ray fluorescence radiation is detected with a four-element silicon drift energy dispersive detector (Vortex ME4) [22]. Additional details can be found in Hu et al. [97]. Fluorescence was analyzed using the software package MAPS [64]. Fitting and quantification of the fluorescence data were performed with thin film standards (National Bureau of Standards, Standard Reference

Material 1832 and 1833). An anhydrous C_3S particle was used as an additional standard material to increase the accuracy.

The nXRF results have two limitations: 1) the X-ray beam penetrates through the material and causes X-ray fluorescence along its path, which makes it challenging to determine depth-dependent information in the sample; 2) a portion of the fluoresced X-rays are absorbed by the sample before they can reach the detector. Both of these limitations can be overcome by combining the structural information from nCT with the nXRF datasets.

After aligning the two data sets, the nCT measurements can determine the travel path of the nXRF beam as well as the different materials that the beam traverses. Next, the areas analyzed by nXRF are carefully chosen so that they are close to the EDS detector (less than 4 μm from the edge). By reducing the travel path of the X-rays, the absorption is reduced to about 10 % for Si and 5 % for Ca [113]. Finally, a region of anhydrous C_3S was purposely included in this analysis so that these measurements could be compared to measurements of the C_3S standard.

5.2.6 Data Fusion of nCT and nXRF

An overview of the data fusion of nCT and nXRF, which will be called nTACCo for brevity, is shown in Fig 5.5. The nCT and nXRF data are aligned by comparing 2D radiographs to match the particle boundary and areas of uniquely identifiable chemical composition. Additional details about nTACCo are provided in earlier publications [97,136].

The nXRF signal can be deconvoluted after aligning the data sets to determine the chemical composition for each individual constituent in the particle. Examples of this process are shown using Particle 1 in Fig 5.5 at locations A and B. At location A, the nCT data show that the X-ray beam only passes through the anhydrous C_3S. This material will have a concentration, C_A, per unit area of the beam ($\mu g/\mu m^2$), and the length of travel, L_A, is expressed in μm. The concentration density can then be calculated at point A in $\mu g/\mu m^3$ as

$$D_{C_3S} = C_A/L_A \qquad (1)$$

This process is then repeated at location B. According to the nCT data, this location has two constituents present and the aligned data can help determine the length that the X-ray beam has passed through each constituent (L_{B1}, L_{B2}). Since the concentration density of the anhydrous C_3S was determined in the calculation of location A, and at 119 other points like it, the average value, $\overline{D_{C_3S}}$, can be used to estimate the concentration of the region modified during hydration (D_{Mod}). The concentration density of the modified region, D_{Mod}, can be found by subtracting the average concentration of the anhydrous C_3S multiplied by the length of the path through that material (L_{B1}) from the total concentration at point B and then dividing by the depth of the modified region at that location (L_{B2}), using the equation

$$D_{Mod} = \frac{C_B - \overline{D_{C_3S}} \cdot L_{B1}}{L_{B2}} \qquad (2)$$

This process was completed for 497 points. The average and one standard deviation are given in Table 5.4.

5.3 Results

The calorimetry data in Fig 5.1 indicate that the measurements taken at 2.5 h occur during the period of slow reaction that commences shortly after mixing with water. In Fig 5.3, the nCT data of the entire sample shows some changes caused by the formation of hydration products and the movement of individual particles; however, there are no large changes in volume or dimensions. A slice from the 3D tomograph shows a cross-section from Particle 1 before and after the 2.5 h reaction. This particle is modified in some areas within its original boundary, but has not formed a significant amount of outer product (*i.e.*, outside the original surface of the C_3S grain). Seven particles have been investigated in detail for this paper and their locations are shown on the 3D tomograph. The volumetric changes of these particles are summarized in Table 5.3. The initial

volume of the particle is labeled as “Original”. After hydration for 2.5 h, the volumes are labeled as “Modified”, “Totally dissolved” and “Total”. The modified region is a portion of the particle that has changed in gray value when compared to the original scan. The totally dissolved material corresponds to an area where there was material in the original scan, but after 2.5 h the material in the region is gone. The column labeled “Total” is the sum of the modified and totally dissolved material. The percentage of change in volume for each particle is calculated by dividing the total volume of hydrated phases by the initial particle volume.

5.3.1 Analysis of individual particles

The nCT data for each particle are used to show its 3D structure, inner structure, typical slices and the distribution of reaction depth. A typical example is shown in Fig 5.4. The slice locations are indicated by gray dashed lines on the 3D structural model. The inner structure shows the particle with a quadrant removed so that the internal structure of the particle can be observed. These slices and inner structure are chosen to highlight the interior changes of the particle. The images in the column “Before” give the original boundary of the anhydrous C_3S particle; the images in column “After 2.5 h” show how these same areas changed after 2.5 h of hydration.

All investigated particles show regions of the particle with some changes in gray value but little change in their overall geometry. This change in gray value means the reacted regions could have different density, different composition, or both. To determine the regions of high change, the “Before” and “After” images are subtracted so that the areas of change are highlighted in the “Difference” column of Fig 5.4. These areas of significant change are collectively called the “modified region”. The modified region could be partially dissolved C_3S or perhaps a newly formed hydration product. However, this cannot be determined from just the nCT results. The nXRF data will be used to provide more insight into these regions later in the paper.

Next, the data are separated into different materials by using a set of constant gray value ranges. These regions were labeled as anhydrous C_3S, modified region, or totally dissolved region. The totally dissolved regions were defined as those high change regions with a gray value close to that of air.

5.3.2 Detailed Analysis of Particle 1

As shown in Table 5.3, Particle 1 had an original volume of 22.32 μm^3. After 2.5 hours of hydration, 37.8 % of the particle volume was modified. In Fig 5.4, these modified regions are localized to two primary sites, Site 1 and Site 2. By removing a quadrant from the particle to examine the internal structure, the depths of the two sites are significantly different, being about 0.4 μm for Site 1 and about 1.1 μm for Site 2. The differences in depths for two sites are further described by comparing their distributions, which show that Site 2 has more areas with depth greater than 0.6 μm than Site 1 (the bottom figure in Fig 5.4). Moreover, a peak can be observed from the depth distribution of Site 2 near 1.2 μm, which indicates some locally deep areas on the particle can react to much greater depths than other regions. The average reaction depth of the entire reacted surface is calculated as 0.61 μm with one standard deviation of 0.29 μm as given in Table 5.3.

5.3.3 Particle with different amounts of reaction

The data for Particle 2 are shown in Fig 5.6. Originally, this particle had a volume of 97.71 μm^3. After hydration, 21 % of the particle was modified and 9 % totally dissolved. The images from five different internal locations show the formation of interior structures, including a deep pit and a hole in slice 1 to 3 and 5. This pit penetrates much further than the other regions, reaching 1.4 μm, compared with the average reaction depth of 0.64 μm.

The distribution in reaction depth for this particle was examined by plotting the "Entire reacted surface" based on the depths from the totally dissolved and modified regions. The majority of the

reaction depths are limited to within one standard deviation of the mean, which is (0.64 ± 0.35) μm; however, some areas of the particle have pits with depths greater than 1.5 μm. The depths for the totally dissolved regions are plotted separately based on measuring the depth only within these regions. The majority of the totally dissolved areas are within one standard deviation range of the mean, (0.38 ± 0.23) μm, but some areas can still reach as deep as 1 μm.

5.3.4 Particles with different degrees of hydration

The apparent extents of reaction among different particles are quite variable. As an example, Particle 3 in Fig 5.7 shows almost 90 % change in its interior while still maintaining the original boundary. Only a small region of the particle remains unreacted on the surface. This anhydrous region corresponds to the areas of low reaction depth that appear as a small peak located at about 0.4 μm in the bottom figure of Fig 5.7.

In contrast to Particle 3, Particle 4 (Fig 5.8) changed in volume by 9 %. Like Particle 2, Particle 4 also has some regions that are "totally dissolved". In the image of "Before" at slice 1, a split in the lower left corner of the particle indicates this area may be damaged. After reaction, the regions close to that split show more reaction than any other regions on the particle, forming a localized reaction site (Site 1). Site 1 is the only area on this particle that has a depth greater than 1 μm.

5.3.5 The chemical composition of the modified region

The molar Ca/Si and estimated mass densities for Particles 1 and 3 are given in Table 5.4. Their distributions shown in Fig 5.9 are all close to a Gaussian shape. For the modified region on Particle 1, average densities of Ca and Si are (0.62 ± 0.18) g/cm^3 and (0.26 ± 0.06) g/cm^3, respectively, corresponding to an average Ca/Si molar ratio of 1.68 ± 0.55. The modified region on Particle 3 shows a similar the density of Si, (0.24 ± 0.07) g/cm^3, but lower density of Ca, (0.47

± 0.09) g/cm^3, yielding an average Ca/Si molar ratio of 1.53 ± 0.64. Based on previous publications, these ratios correspond more closely to newly formed hydration product, in particular to C-S-H [79, 83,128,130,134,137]. To complete the stoichiometry for these modified regions as C-S-H, the amount of bonded H_2O needs be determined. According to a recent study on the structural modeling for C-S-H, the H_2O/Si of the hydration product after drying at 110 ^oC has been found to be approximately a linear function of the Ca/Si ratio as

$H_2O/Si = 19/17 \cdot Ca/Si - 7/17$ (3) [138]

By assuming the stoichiometry as C_x-S-H_y , where *x* is the Ca/Si ratio and y is the H_2O/Si ratio in equation (3), one could estimate the mass density based on the measured Ca and Si densities.

The result shows the average dried mass densities of (1.69 ± 0.43) g/cm^3 and (1.34 ± 0.22) g/cm^3 for the modified region on Particles 1 and 3, respectively, which could be higher if the pores are filled with water. These values are very close to the predicted density in the literature of 1.7 g/cm^3 for the low-density product, or even lower if the material has higher porosity based on the colloidal structural models of C-S-H [139]. However, since the amount of Si indicates the chain length in C-S-H composition, the similar Si densities of these regions suggest they are expected to have similar porosity [140]. The difference of the calculated mass densities is mainly attributed to the different Ca densities between the two materials. Although nXRF measurements were not made on all the particles, similar gray values were measured in the tomographs for these regions. Since the gray value is an indication of the X-ray absorption, this suggests that all of these regions would have composition and density close to what has been classically called inner product.

5.3.6 Summary of particle modification

The summary of the volumetric results of seven particles is given in Table 5.3. The additional nCT data for Particles 5, 6 and 7 are given in the supplementary information. The amount of modification of the particles varied from 9 % to 90 %. This suggests that the reaction behavior of

individual particles is quite different and that the particle modification does not happen uniformly around the particle surface. This could be attributed to the differences in particle sizes, the number density of the reaction sites, and the depths of reaction. Excluding Particles 3 and 4, the remaining particles have a similar *average* degree of modification (33.65 %), but the standard deviation of 23.55 % indicates that the local extents of reaction are quite variable. All particles except for Particle 3 show similar average depths of reaction within one standard deviation range of the mean, (0.72 ± 0.3) μm.

The modified particles are not observed to have volume changes that extend outside the original boundaries of the particle. However, on the two largest particles (Particles 2 and 4) certain regions were observed to dissolve completely, and to have modified regions of much larger volumes. This means that the phenomenon of forming hydration product while the C_3S is reacting at the same location is still more predominant than pure dissolution without precipitation.

It should be noted that it is possible that any other particles that were present initially but which may have become dislodged or may have completely dissolved, were not included in this analysis.

5.4 Discussion

5.4.1 Degree of modification

The percentage change in Table 5.3 is higher than one would expect from suggested changes in the literature based on bulk analysis [131,141,142]. It should be noted that all of the particles investigated were quite small (< 5 μm diameter) and the reaction depths of the particles were quite comparable. This means that larger particles will have significantly less reaction relative to their initial volumes than these smaller particles. Larger particles will be the primary contribution to the volume of material in the bulk analysis, which may be why the bulk measurements do not correspond to the measurements in this study. Also, the higher w/s may cause a higher rate of

dissolution and therefore ultimately a greater amount of dissolution for a particle over a given time period.

5.4.2 Preferential reactions

Although the triclinic C_3S in this experiment is a pure material, the reaction on every particle is not uniform and does not cover the entire surface. Some regions show more reactions than others. This preferential reaction could be caused by the high density of defects, such as crystallographic imperfections, mechanical damage or other disorder in the crystal structure [121]. These high-defect regions could cause more etch pits to form and lead to rapid localized dissolution. This observation of preferential reaction agrees with the findings of earlier SEM/TEM studies [79,80,87,124,125]. The smaller particles may be more reactive because they could originate from material that has been broken off during the grinding process and so could have originated from a damaged portion of a larger particle. Further work is needed to investigate this.

5.4.3 The formation of inner product

For crystalline materials such as C_3S with ionic bonding, the dissolution is expected to follow the stoichiometry of the material. Congruent dissolution of C_3S has been previously observed by others [141,142]. One important observation is that the hydration product seems to closely match the surface of the original particle. It is possible that the hydration product forms soon after the C_3S has dissolved.

Observations from soft X-ray microscopy have suggested that the rapid dissolution of C_3S caused by adding $CaCl_2$ accelerator leads to the formation of inner product as the material dissolves [95]. This would allow the particles to maintain their original boundaries despite rapid dissolution. The rapid reaction may increase the local ion concentration faster than the ions can be transported away from the surface, resulting in immediate precipitation.

5.4.4 The possible mechanism and influences

A hypothesized mechanism for the formation of this type of hydration product is summarized in Fig 5.10. First, as the disturbed regions of the anhydrous C_3S material reacts with solution, the etch pit start to form on the surface. Rapid dissolution continues to occur inside the pit. This dissolution makes the ionic concentration inside the pit much higher than the surrounding regions. If the ionic concentration continues to increase within the pit at a faster rate than it can diffuse into the bulk solution, hydration products may form locally inside of the pit. This early hydration product would then start filling the pit. This would continue until the hydration product reaches the original surface of the particle. Growth may stop if the pit fills to the surface with hydration product because the ionic concentration would not be as high in the bulk solution, owing to the relatively high w/s used in this experiment. If the w/s were lower, the ionic concentration in the surrounding fluid would likely be higher and therefore the hydration product might continue to form outside the original particle boundary. Investigating this possibility is an area of future work.

For Particles 2 and 4, the geometry or reactivity of the pit appear to lead to a low local concentration, so these portions of the particle dissolve and do not fill with hydration product. In any case, important changes are occurring in the slow reaction period that is characterized by rapid localized dissolution and precipitation. Ionic concentration gradients in the local areas appear to be important on this length scale and may control phenomena that will occur in the later stages of hydration.

The formation of early hydration product has been hypothesized as a factor in the reaction rate of early periods of hydration [127-131]. According to this work, the early hydration product preferentially forms at locations where the C_3S is rapidly dissolved. This localized rapid dissolution of C_3S and subsequent formation of hydration product could impact the dissolution

rate of C_3S. Deeper dissolved regions correspond to larger volumes of hydration product needed to fill the etch pit. This hydration product may act to block reaction sites or to reduce diffusive mass transfer away from those sites, thereby reducing the reaction rates of the covered C_3S. Because the C_3S is obscured, the concentration gradient should decrease over time, which may cause some of the early hydration products to start dissolving. This metastable behavior of the early hydration product of C_3S hydration has been studied by other researchers [128]. This could explain how the formation of early hydration product could control the dissolution of C_3S during the induction period.

5.6 Conclusion

In this paper, seven individual C_3S particles were studied by nCT, and two of these particles with nXRF, after hydration of 2.5 hours with w/s = 5 in 15 mmol lime solution. The nCT technique is able to give a one-to-one comparison of the same region before and after reaction to show precisely how and where the reaction happens. These datasets can be turned into 3D models to show the reactions on both the surface and interior of the particles. These observations can also be quantified into volumetric datasets. Using nTACCo, the nCT and nXRF data were combined to characterize the chemical compositions and mass densities of the constituents on two reacted particles. The following results have been found:

- The reactions on individual particles are not uniformly distributed on the surface of the particles.

- The percentage of changes in volume varies from 9 % to 90% for different particles with average 33.65 % and one standard deviation of 23.55 %.

- The depths of reaction also vary with location: the average depths for these individual particles are 0.72 μm with one standard deviation of 0.3 μm.

- The majority of the particles retain their original geometry after they react (for 2.5 h). The modified regions seem to fill the space of the dissolved material.

- The modified region is hydration product with Ca/Si of 1.53 and 1.68 for two different particles with similar Si density, but different Ca density.

- The average mass densities for these modified materials are found as 1.34 g/cm^3 and 1.69 g/cm^3 for two particles, which correspond to low density product in the literature.

- Two particles were observed to have regions that totally dissolved.

The formation of this hydration product is hypothesized to result from the local concentration gradient inside the etch pits. This observation could explain a possible impact of this hydration product on the initial dissolution rate of C_3S, as the rate of attack on the defect is self-limiting

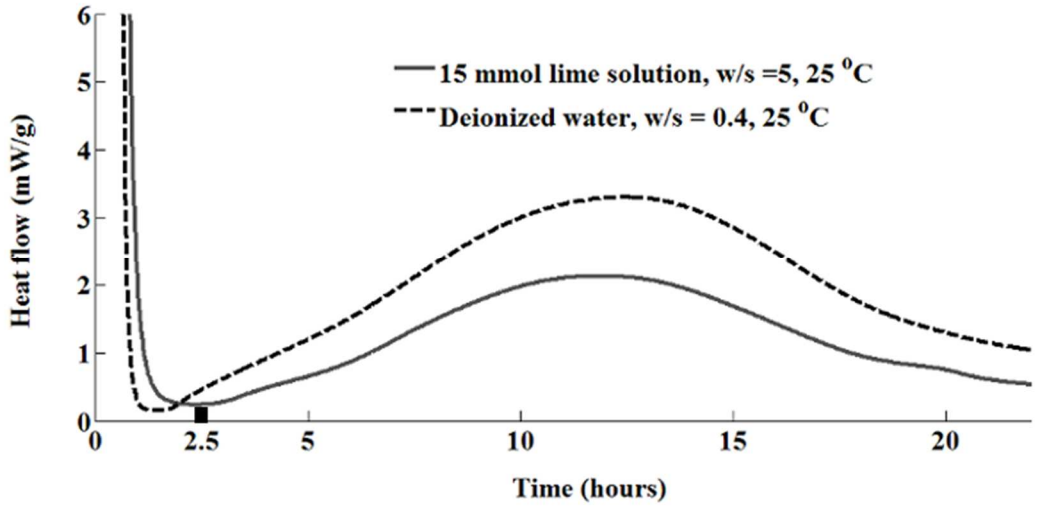

Fig 5.1 – Curve from isothermal calorimeter. The wide bar on the X-axis shows the time period of hydration used in the imaging experiments.

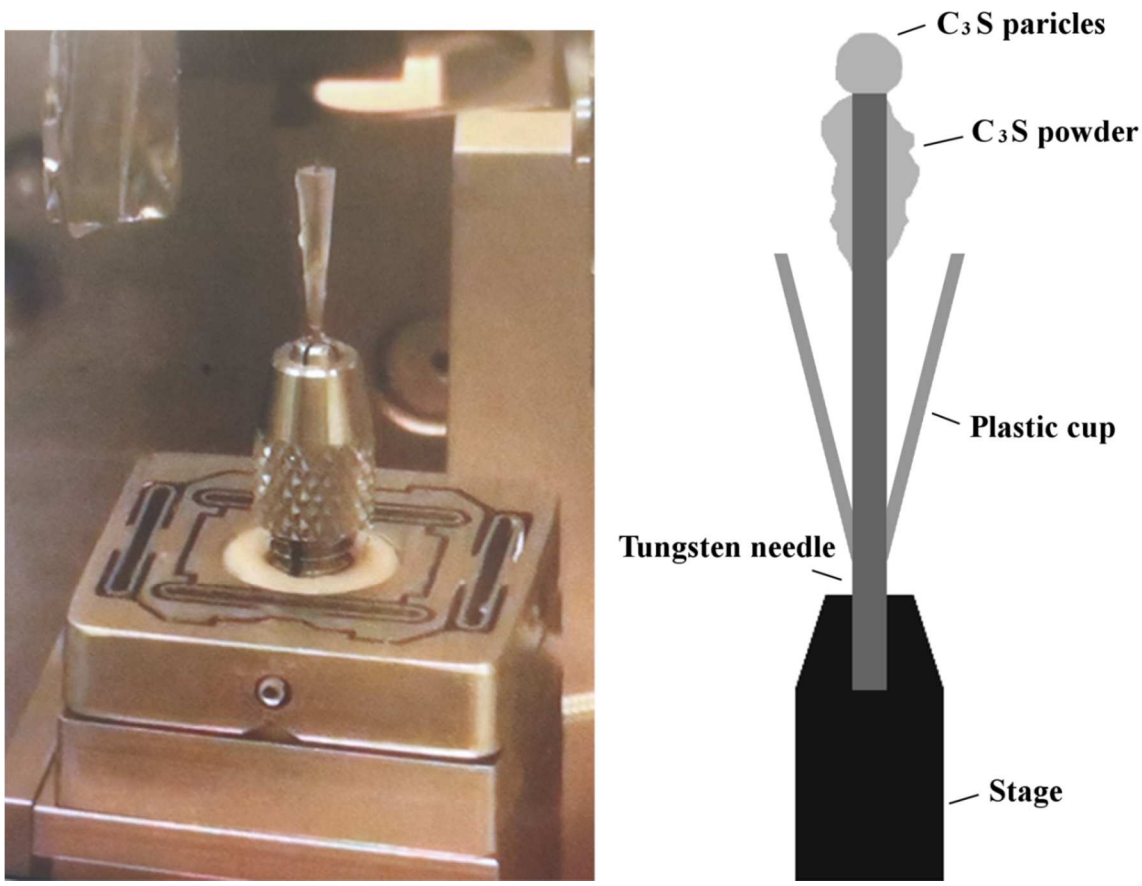

Fig 5.2 – An overview of the experimental setup and the assembled setup on the beam line.

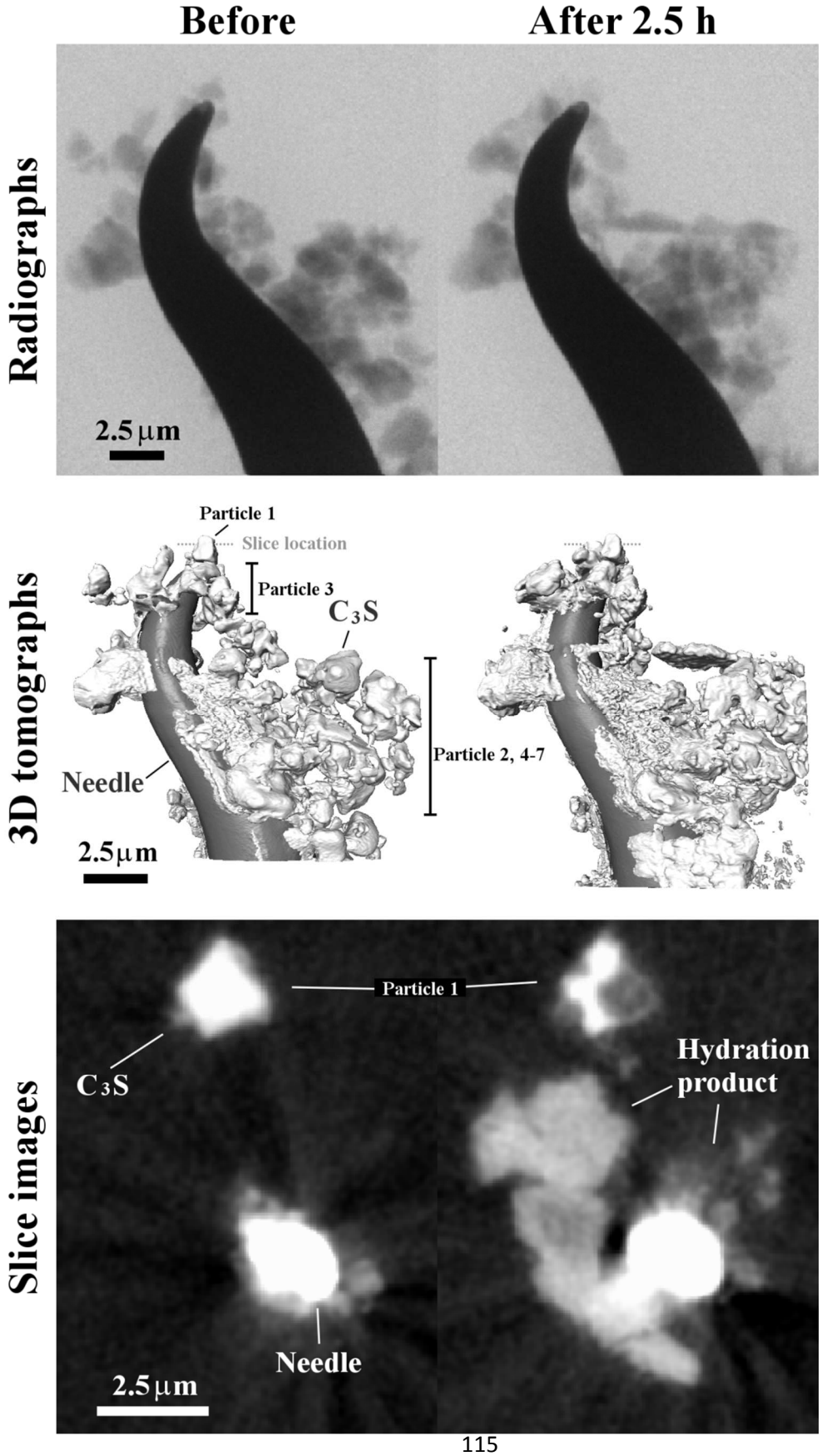
Before
After 2.5 h
Radiographs
2.5 μm
Particle 1
Slice location
Particle 3
C3S
Needle
Particle 2, 4-7
3D tomographs
2.5μm
Particle 1
C3S
Hydration product
Needle
2.5 μm
Slice images

Fig 5.3 – The nCT dataset showing a radiograph, tomograph, and a slice image crossing a single particle, Particle 1.

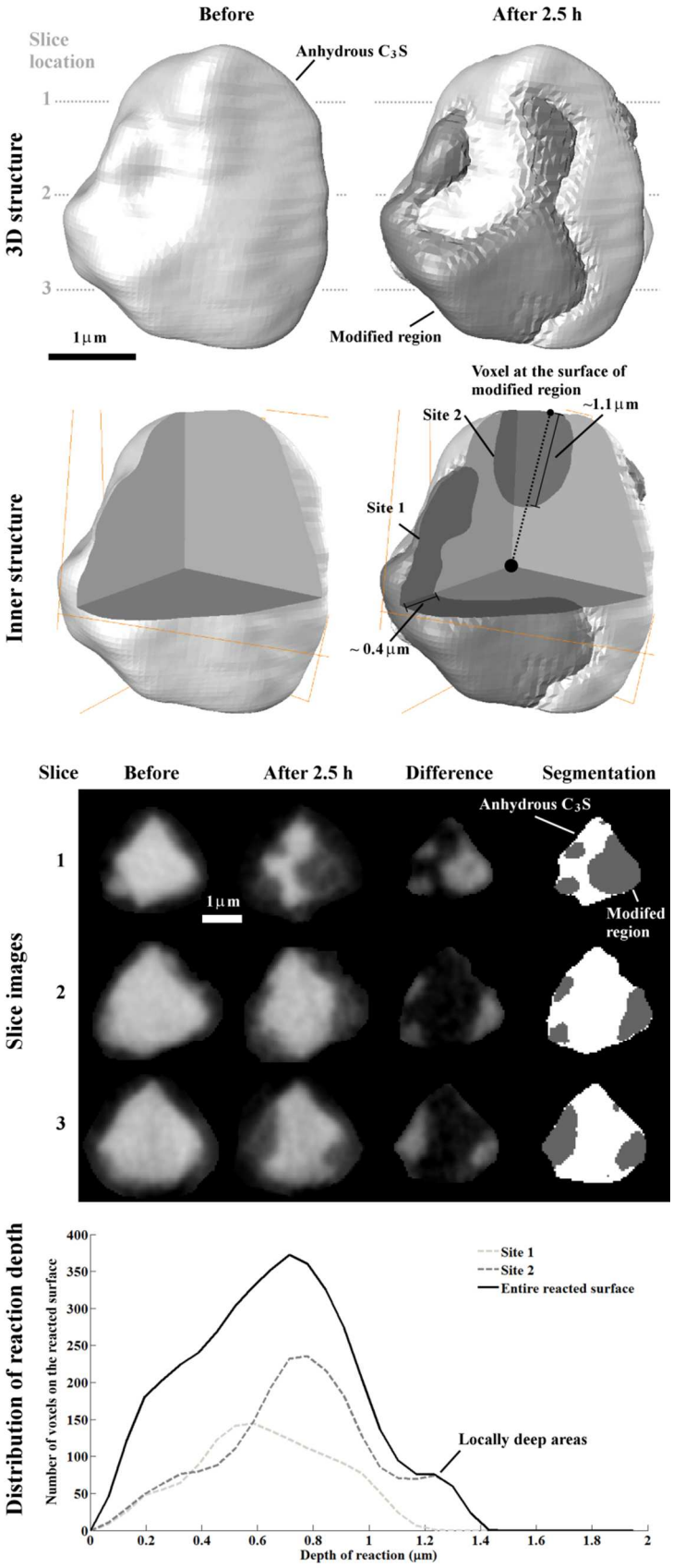
Before
After 2.5 h
Slice location
1
2
3
3D structure
Anhydrous C_3S
Modified region
1 μm
Voxel at the surface of modified region
Site 2
~1.1 μm
Site 1
~ 0.4 μm
Inner structure
Slice
Before
After 2.5 h
Difference
Segmentation
Anhydrous C_3S
Modifed region
1 μm
Slice images
Site 1
Site 2
Entire reacted surface
Locally deep areas
Number of voxels on the reacted surface
Depth of reaction (μm)
Distribution of reaction depth

Fig 5.4 – The nCT datasets of Particle 1

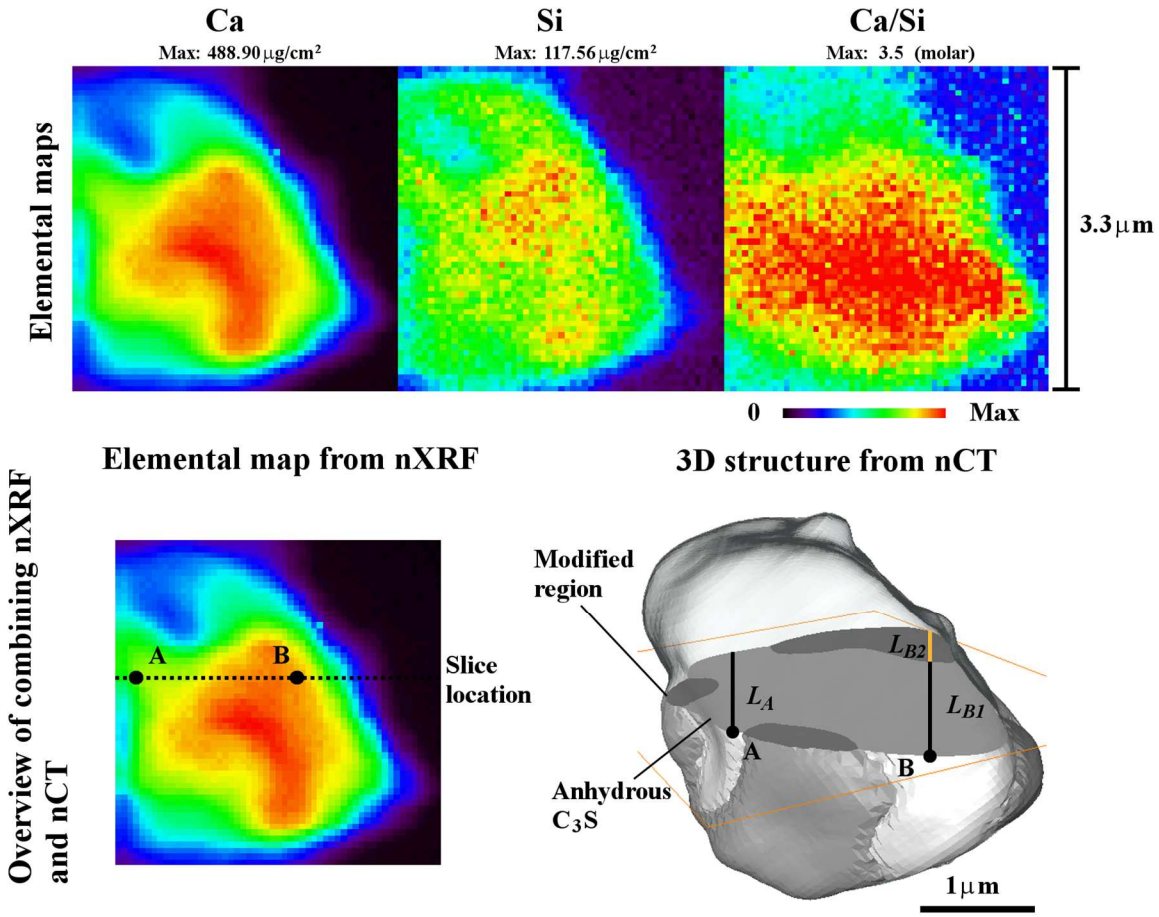

Fig 5.5 – The elemental maps from nXRF analysis of Particle 1. An overview of the scheme of de-convoluting the nXRF elemental maps by using the structural information from nCT datasets.

Fig 5.6 – The nCT datasets for Particle 2

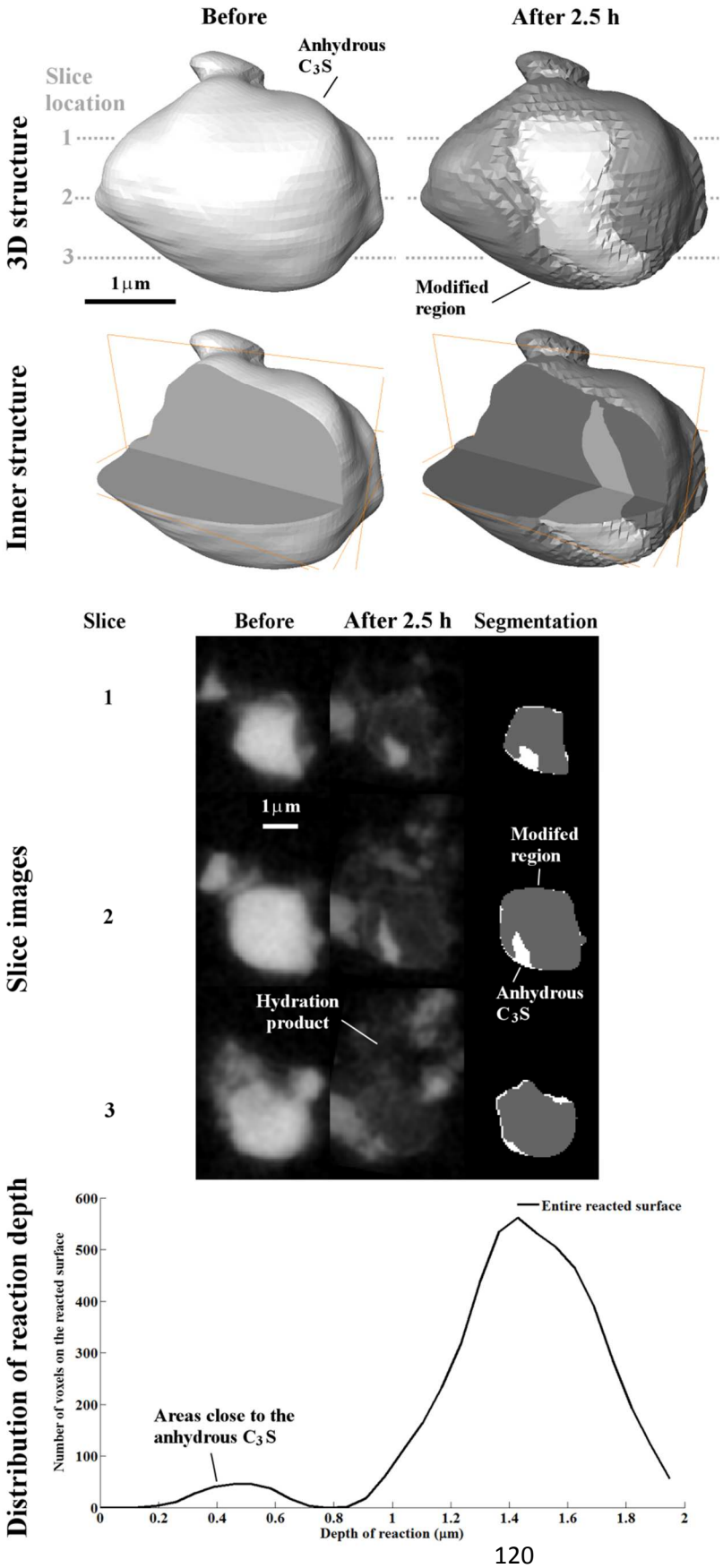
Before
After 2.5 h
Anhydrous C_3S
Slice location
1
2
3
3D structure
1 μm
Modified region
Inner structure
Slice
Before
After 2.5 h
Segmentation
Slice images
1
2
3
1 μm
Modifed region
Anhydrous C_3S
Hydration product
Distribution of reaction depth
Entire reacted surface
Number of voxels on the reacted surface
Areas close to the anhydrous C_3S
Depth of reaction (μm)
0
100
200
300
400
500
600
0.2
0.4
0.6
0.8
1
1.2
1.4
1.6
1.8
2

Fig 5.7 – The nCT datasets for Particle 3

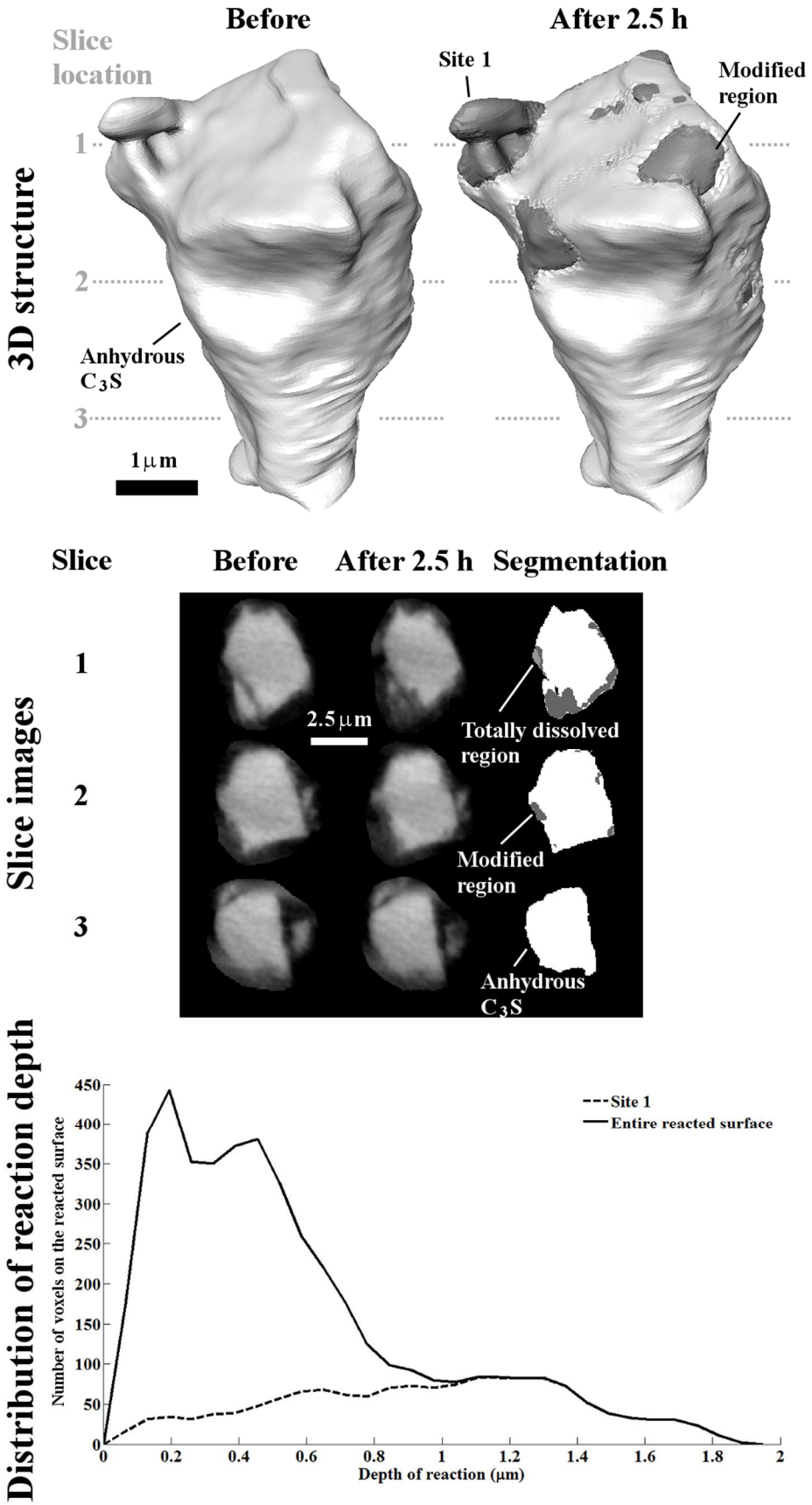
Before
After 2.5 h
Slice location
Site 1
Modified region
3D structure
1
2
3
Anhydrous C_3S
1 μm
Slice
Before
After 2.5 h
Segmentation
Slice images
1
2
3
2.5 μm
Totally dissolved region
Modified region
Anhydrous C_3S
Distribution of reaction depth
Number of voxels on the reacted surface
Depth of reaction (μm)
Site 1
Entire reacted surface
0
50
100
150
200
250
300
350
400
450
0.2
0.4
0.6
0.8
1
1.2
1.4
1.6
1.8
2

Fig 5.8 – The nCT datasets for Particle 4.

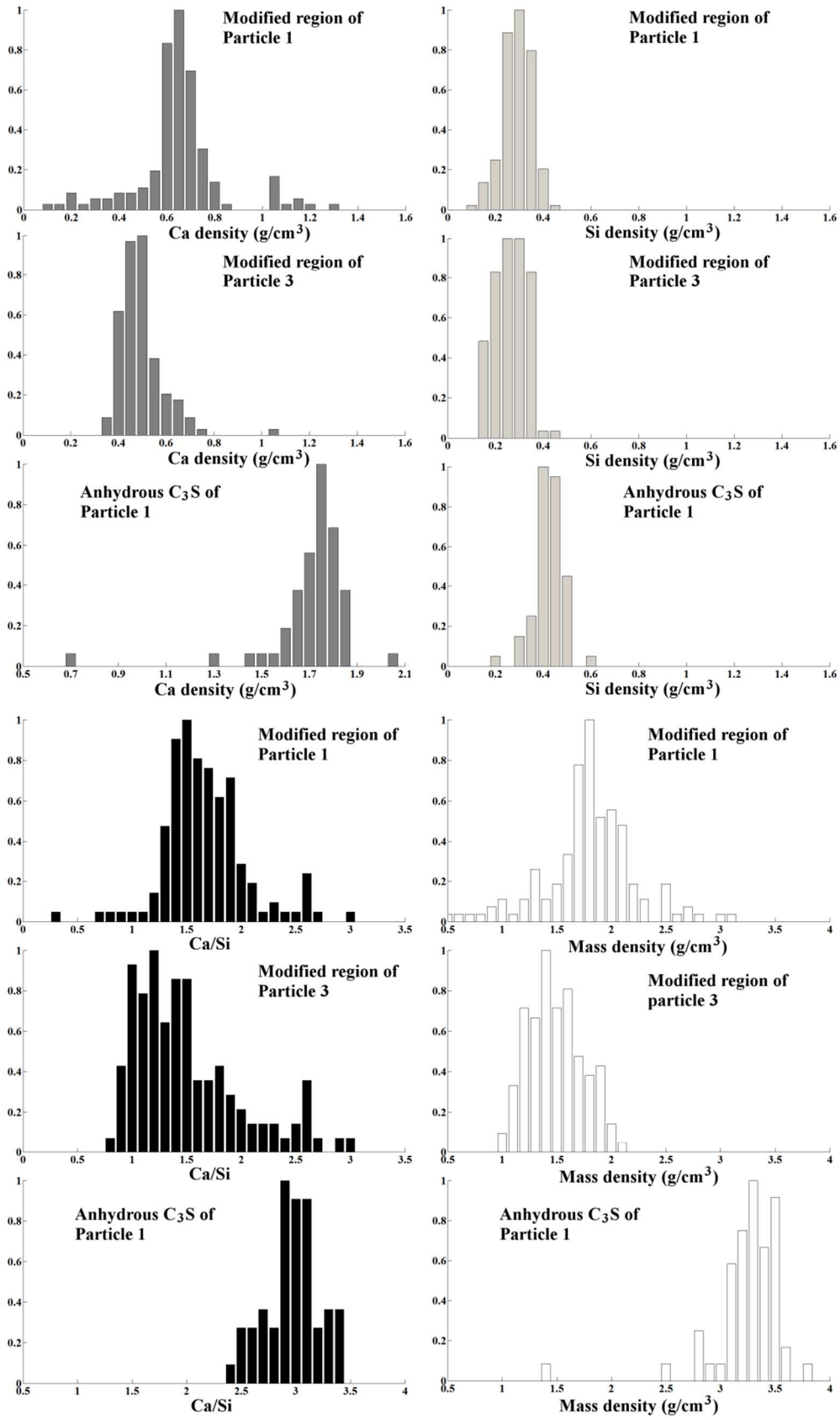
Modified region of Particle 1
Ca density (g/cm3)
Modified region of Particle 1
Si density (g/cm3)
Modified region of Particle 3
Ca density (g/cm3)
Modified region of Particle 3
Si density (g/cm3)
Anhydrous C3S of Particle 1
Ca density (g/cm3)
Anhydrous C3S of Particle 1
Si density (g/cm3)
Modified region of Particle 1
Ca/Si
Modified region of Particle 1
Mass density (g/cm3)
Modified region of Particle 3
Ca/Si
Modified region of particle 3
Mass density (g/cm3)
Anhydrous C3S of Particle 1
Ca/Si
Anhydrous C3S of Particle 1
Mass density (g/cm3)

Fig 5.9 – The distributions of densities of Ca and Si, Ca/Si ratio, and mass density for each constituent analyzed by nTACCo technique.

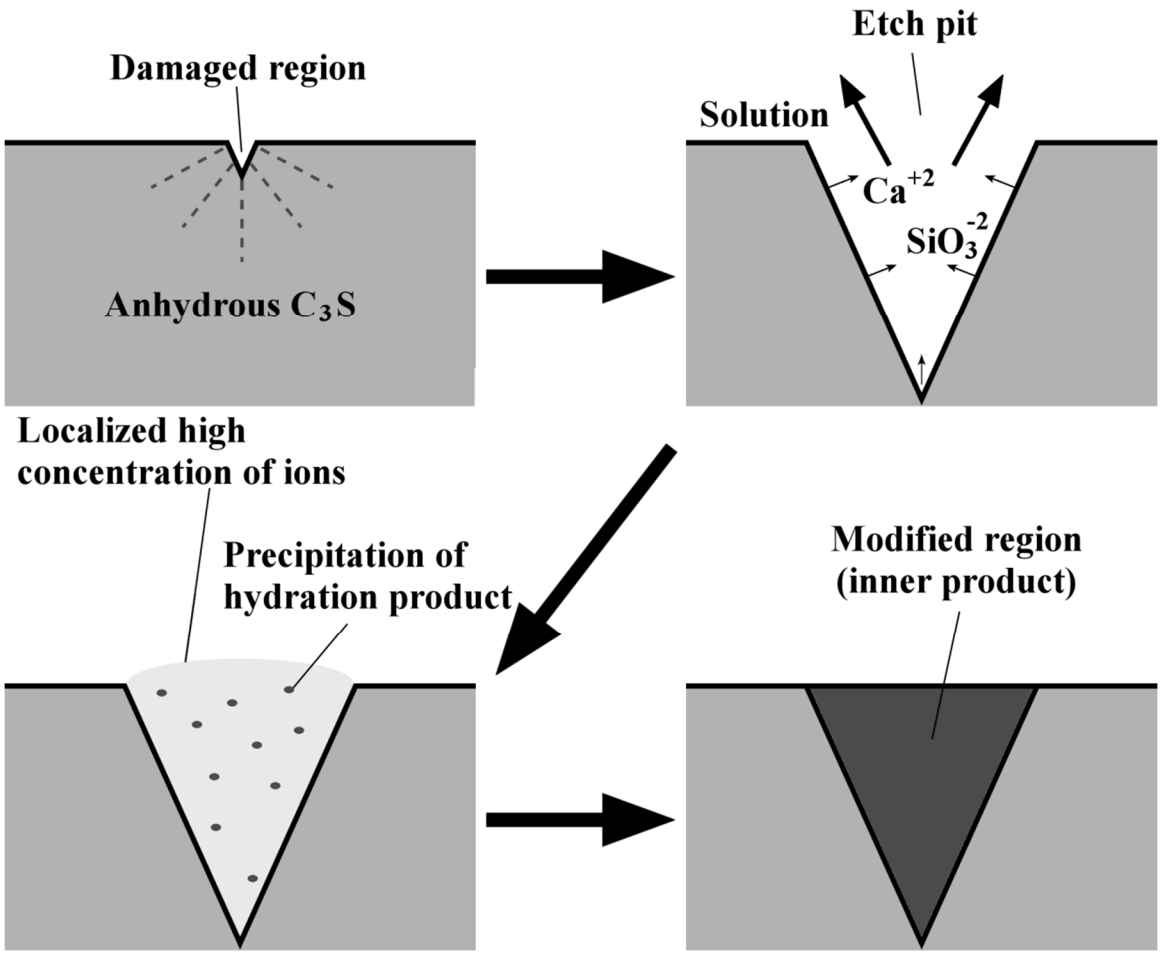

Fig 5.10 – A demonstration of mechanism of how the hydration could form in the etch pit during dissolution.

Table 5.1 – The elemental composition based upon a single analysis and the surface area of C_3S based on two analysis. An uncertainty in the surface area measurement of one standard deviation is given.

ICP Elemental analysis (mole %)	Al	Ca	Mg	Si	Sr
	<0.2	74.8	<0.002	25	0.018
BET surface area (m^2/g)	1.2156± 0.0028				

Table 5.2 – The summary of the instrument settings for nCT and nXRF experiments

nCT	Resolution		65 nm/pixel
	Numbers of radiographs from 0^o to 180^o		901
	Exposure time		20 s
	Source energy		5.4 kev
	Dynamic ranges*	min	-5000
		max	5000
nXRF	Resolution		50 nm/pixel
	Detector dwelling time		0.1 s
	Scaler count time		0.1 s

* the data is displayed in FLOAT type

Table 5.3 – The summary of the measurements of volume and drilling depth of dissolution for seven particles.

Particles	Original (μm^3)	After hydration(μm^3)					
		Anhydrous C_3S	Regions of changes			Percentage of change	Depth of reaction (μm) Ave±Std
			Modified	Totally dissolved	Total		
3	12.33	1.21	11.12	~0	5.51	90.19%	1.40±0.30
5	17.21	12.47	4.74	~0	4.74	27.53%	0.72±0.29
1	22.32	13.87	8.44	~0	8.44	37.84%	0.61±0.29
6	27.75	19.01	8.74	~0	8.74	31.50%	0.59±0.45
7	50.43	38.16	12.27	~0	12.27	24.33%	0.59±0.40
4	88.17	81.30	5.89	0.98	6.87	8.98%	0.52±0.40
2	97.71	68.73	20.13	8.85	28.98	30.21%	0.64±0.35
					Avg=	33.65%	0.72
					Std dev	23.55%	0.3

Table 5.4 – The elemental density and mass density of the constituents on Particle 1 and 3.

	Modified region		Anhydrous C_3S	
	Particle 1	Particle 3	Particle 1	Standard
Ca (g/cm^3)	0.62±0.18	0.47±0.09	1.69±0.18	1.69±0.06
Si (g/cm^3)	0.26±0.06	0.24±0.07	0.40±0.06	0.40±0.03
Mass density (g/cm^3)	1.69±0.43	1.34±0.22	3.22±0.36	3.20±0.13
Ca/Si (molar)	1.68±0.55	1.53±0.64	3.01±0.28	3.03±0.16

CHAPTER VI

CONCLUSION

The research presented in this dissertation have developed two novel analysis techniques that combines 3D tomography with 2D chemical map to study complex particle materials with the applicable resolutions from micron scale to nanoscale. These techniques are called TACCo and nTACCo respectively. These techniques were first developed to characterize fly ash samples and then modified to be used for in-situ study of cement hydration. Although the applications presented in this dissertation are mainly based on only two types of cementitious material, the potentials have been shown that it could be applicable for many other materials.

The main conclusions of the dissertation are:

6.1 3D Chemical Segmentation of Fly ash particles with X-ray Computed Tomography and Electron Probe Microanalysis

- Tomography assisted chemical correlation (TACCo) was demonstrated to perform consistently on three different fly ash particles from the same source.
- This technique found that there were two unique constituents that made up over 50% of the volume of the particles. Minor phases in the particles were observed as well.
- The segmentation range for these repeated constituents were similar between particles.
- 3D chemical models were created for the fly ash particles.

- The subsequent analysis of these 3D models showed that while there was similarity between the constituents in each, the chemical distribution with depth differed.

6.2 Combined three-dimensional structure and chemistry imaging with nanoscale resolution

- The 3D structure information from nCT and 2D chemical information from nXRF was combined with a novel data fusion technique called nTACCo. This is the first time that a 3D combined chemical and microstructure map at the 150 nm length scale was created in only a few hours.

- The technique was validated through the use of Au fiducial markers.

- The technique was able to create 3D segmented maps of six constituents that would not have been determined by only using the nCT technique because of low X-ray absorption contrast.

- The 3D results from this technique show that the dissolution of this fly ash particle occurred throughout the volume and not just at the surface. These internal channels are likely caused by localized rapid dissolution.

6.3 Direct three-dimensional observation of the microstructure and chemistry of C_3S hydration

- The samples observed near the end of the induction period show localized formation of hydration product about 200 nm thick on some of the particle surfaces.

- At the beginning of the acceleration period, some C_3S particles that were approximately 4 μm in diameter showed significant changes, while other particles of smaller size show only limited changes.

- Hydration product was observed to form between particles that were about 2 μm apart but not in other parts of the sample.

- For samples near the middle of the acceleration period, the volume of hydration products was over 4 times the original volume of the particles within the field of view. The hydration products within about 1 μm of the anhydrous C_3S surface had a higher X-ray absorption.

- During this same time period the hydration products within 1.6 μm of the anhydrous C_3S had twice the Si concentration as hydration products found further from this region.

- Solvent exchange using isopropyl alcohol showed minimal disruption of the microstructure for a sample hydrated for 2.5 h.

- Samples that were cured at 50 ^oC showed more rapid reaction and a higher volume of hydration than those at 25 ^oC.

6.4 Measurement of 3D structure, chemistry, and mass density of C_3S hydration during the induction period

- The observed particle reactions were not uniformly distributed on the surface of the particles.

- The percentage of changes in volume varies from 9 % to 90% for different particles with an average of 33.65 % and one standard deviation of 23.55 %.

- The depth of reaction of the particles were different for different locations, the average depths for the individual particles is 0.72 μm with one standard deviation of 0.3 μm.

- The reacted region of the particles retained a similar geometry despite showing chemical changes.

- Two particles showed regions that were totally dissolved.

- This hydration product in modified region has been found with Ca/Si ratios of 1.53 and 1.66 for two different particles with similar Si density but different Ca density.

6.5 Future work

In this work, the research has focused on studying triclinic C_3S within the first seven hours of reaction in 15 mmol lime solution. However, to understand the hydration mechanisms of Portland cement, more observations are needed for different types of material and solution. The following is a list of future work:

- The hydration of monoclinic C_3S with saturated $CaSO_4$ solution and lime solution needs be studied. This is to investigate the difference between monoclinic and triclinic C_3S and the impact of SO_4 ions on hydration.

- Different solutions, such as saturated $CaSO_4$ solution, saturated $CaSO_4$ and lime solution, and Na_2SO_4 solution, need be investigated to understand the roles of different ions in the hydration process.

- Another major component of Portland cement, tricalcium aluminate (C_3A) should be studied as it reacts in saturated $CaSO_4$ and lime solution and the morphological and chemical changes need to be better understood in the hydration process.

REFERENCES

[1] American Portland Association: Untied States Cement Industry 2015. Available from http:// http://www.cement.org/

[2] Madlool NA, Saidur R, Hossain MS, Rahim NA., A critical review on energy use and saving in the cement industries. Renewable and Sustainable Energy Reviews 2011;15:2042-2060.

[3] Ahmaruzzaman M. A review of the utilization of fly ash. Progress in Energy and Combustion Science 2010;36:327-363.

[4] Fernández-Jiménez A, Palomo A. Characterization of fly ashes. Potential reactivity as alkaline cements. Fuel 2003;83:2259-2265.

[5] Li C, Li Y, Sun H, Li, L. The Composition of Fly Ash Phase and Its Dissolution Properties Applying to Geopolymeric Materials. J. Am. Ceram. Soc. 2011;94:1773-1778.

[6] Ward CR, French D. Determination of glass content and estimation of glass composition in fly ash using quantitative X-ray diffractometry. Fuel 2006;85:2268-2277.

[7] Kutchko BG, Kim AG. Fly ash characterization by SEM-EDS. Fuel 2006;85: 2537-2544.

[8] Rindby A, Engström P, Janssens K. The use of a scanning X-ray microprobe for simultaneous XRF/XRD studies of fly-ash particles. Journal of Synchrotron Radiation 1997;4:228-235.

[9] Osan J. of Solid Atmospheric Particles and the Environmental Cycle of Fly Ash. Budapes: Semmelweis Medical University; 1996.

[10] Adams F, Janssens K, Snigirev A. Microscopic X-ray fluorescence analysis and related methods with laboratory and synchrotron radiation sources: Plenary lecture. Journal of Analytical Atomic Spectrometry 1998;13:319-331.

[11] Tastan EO, Edil TB, Benson CH, Aydilek AH. Stabilization of Organic Soil with Fly Ash. Journal of Geotechnical and Geoenvironmental Engineering © ASCE 2011 Sept;819-833.

[12] Goldstein J, Newbury D, Joy D, Lyman, C, Echlin P, Lifshin E, et al. Scanning Electron Microscopy and X-ray Microanalysis. 3rd ed. New York: Springer Science + Business Media; 2003.

[13] Göetz LW, Göetz G, Sabbioni E. Mobilization of heavy metals from fossil-fuelled power plants, potential ecological and biochemical implications: assessment studies of the European situation part4. EUR 1981;6998:1–165.

[14] Bright DS, Newbury DE. Concentration histogram imaging. Analytical Chemistry 1991;63:243-250.

[15] Newbury DE, Flori CE, Marinenko RB, Myklebust RL, Swyt CR, Bright DS. Compositional mapping with the electron probe Microanalyzer: Part II. Analytical Chemistry 1990;60:1245-1254.

[16] Kak AC, Slaney M. Principal of Computerized Tomographic Imaging. Philadelphia: Society of Industrial and Applied Mathematics; 2001.

[17] Clackdoyle R, Defrise M. Tomographic Reconstruction in the 21st Century. IEEE SIGNAL PROCESSING MAGAZINE 2010 Jul;60-80.

[18] Kalender WA. Computed Tomography: Fundamentals, System Technology, Image quality, Applications. 3rd ed. Erlangen: Publicis Publishing; 2011.

[19] Alshibli KA, Reed AH. Advances in Computed Tomography for Geomaterials: GeoX2010. Hoboken: John Wiley & Sons, Inc; 2010.

[20] Camerani CM, Golosio B, Somogyi A, Simionovici, SA, Steenari B, Panas I. X-ray Fluorescence Tomography of Individual Municipal Solid Waste and Biomass Fly Ash Particles. Anal. Chem 2004;76:1586-1595.

[21] Takeda T, Wu J, Thet-Theta-Lwin, Huo Q, Yuasa T, Hyodo K, et al. X-ray fluorescent CT imaging of cerebral uptake of stable-iodine perfusion agent iodoamphetamine analog IMP in mice. Journal of Synchrotron Radiation 2009;16:57-62.

[22] Winarski RP, Holt MV, Rose V, Fuesz P, Carbaugh D, Benson C, et al. A hard X-ray nanoprobe beamline for nanoscale microscopy. Journal of Synchrotron Radiation 2012;19:1056-1060.

[23] Provis JL, Rose V, Winarski RP, van Denventer JS. Hard X-ray nanotomography of amorphous aluminosilicate cements. Scripta Materialia 2011; 65:316-319.

[24] ASTMC618. Standard Specification for Coal Fly Ash and Raw or Calcined Natural Pozzolan for Use in Concrete. Pennsylvania: ASTM International; 2004.

[25] Williams PJ, Biernacki JJ, Rawn CJ, Walker L, Bai J. Microanalytical and Computational Analysis of a Class F Fly Ash. ACI Materials Journal 2005;102:330-337.

[26] McCarthy GJ, Swanson KD, Keller LP, Blatter WC. Minerology of western fly ash. Cem. Concr. Res.1984;14:471-478.

[27] Winburn RS, Grier DG, McCarthy GJ, Peterson RB. Rietveld quantitative X-ray diffraction analysis of NIST fly ash standard reference materials. Powder Diffraction 2000;15:163-172.

[28] Chancey RT, Stutzman P, Juenger MC, Fowler DW. Comprehensive phase characterization of crystalline and amorphous phases of a Class F fly ash. Cem. Concr. Res. 2010;40:146-156.

[29] Rémond S, Bentz DP, Pimienta P. Effects of the incorporation of municipal solid waste incineration fly ash in cement pastes and mortars - II: Modeling. Cement and Concrete Research 2002;32:565-576.

[30] Limaye A. Drishti: Volume Exploration and Presentation Tool (Version 1.0.2) [Software]. 2006. Available from http://anusf.anu.edu.au/Vizlab/drishti.

[31] AMIRA (Version 4.1) [Software]. Burlington, MA: VSG.

[32] Raines KS, Salha S, Sandberg RL, Jiang H, Rodriguez JA, Fahimian BP, Kapteyn HC, Du J, Miao J. Three-dimensional structure determination from a single view. Nature 2010;463:214-217.

[33] Chen C, Zhu C, White ER, Chiu C, Scott MC, Regan BC, Marks LD, Huang Y, Miao J. Three-dimensional imaging of dislocations in a nanoparticle at atomic resolution. Nature 2013;496:74-77.

[34] Elechiguerra JL, Larios-Lopez L, Liu C, Garcia-Gutierrez D, Camacho-Bragado A, Yacaman MJ. Corrosion at the nanoscale: The Case of Silver Nanowires and Nanoparticles. Chem. Mater. 2005;17:6042-6052.

[35] Pardo A, Merino MC, Coy AE, Arrabal R, Viejo F, Matykina E. Corrosion behavior of magnesium/aluminium alloys in 3.5 wt.% NaCl. Corrosion Science 2008;50:823-834.

[36] Ryan M, Corrosion: Peering below the surface. Nature Materials 2004;3:663-664.

[37] Shearing PR, Gelb J, Yi J, Lee WK, Drakopolous M, Brandon NP. Analysis of triple phase contact in Ni-YSZ microstructures using non-destructive X-ray tomography with synchrotron radiation. Electrochemistry Communications 2010;12:1021-1024.

[38] Gu M, Genc A, Belharouak I, Wang D, Amine K, Thevuthasan S, Baert DR, Zhange J, Browning ND, Liu J, Wang C. Nanoscale Phase Separation, Cation Ordering and Surface Chemistry in Pristine $Li_{1.2}Ni_{0.2}Mn_{0.6}O_2$ for Li-Ion Batteries. Chem. Mater. 2013;25:2319-2326.

[39] Rose V, Chien TY, Hiller J, Rosenmann D, Winarski RP. X-ray nanotomography of SiO2-coated Pt90Ir10 tips with sub-micron conduction apex. App. Phys. Lett. 2011;99:173102.

[40] Strachan JP, Medeiros-Ribeiro G, Yang JJ, Zhang MX, Miao F, Goldfarb I, Holt M, Rose V, Williams S. Spectromicroscopy of tantalum oxide memristors. App. Phys. Lett. 2011;98:242114.

[41] Hou P, Wang K, Qian J, Kawashima S, Kong D, Shah SP. Effect of colloidal nanoSiO2 on fly ash hydration. Cement & Concrete Composites 2012;34:1095-1103.

[42] Hou P, Kawashima S, Kong D, Corr DJ, Qian J, Shah SP. Modification effects of colloidal nanoSiO2 on cement hydration and its gel property. Composites: Part B 2013;45:440-448.

[43] Tariq F, Haswell R, Lee PD, McComb DW. Characterization of hierarchical pore structures in ceramics using multiscale tomography. Acta Materialia 2011;59:2109-2120.

[44] Shanti NO, Chan VW, Stock SR, De Carlo F, Thornton K, Faber KT. X-ray micro-computed tomography and tortuosity calculations of percolating pore networks. Acta Materialia 2014;71:126-135.

[45] Ferrari M. Cancer Nanotechnology: opportunities and challenges. Nature Reviews | Cancer 2005;5:161-171.

[46] Bressan E, Sbricolim L, Guazzo R, Tocco I, Roman M, Vindigni V, Stellini E, Gardin C, Ferroni L, Sivoella S, Zavan B. Nanostructured Surfaces of Dental Implants. Int. J. Mol. Sci. 2013;14:1918-1931.

[47] Dusad A, Chakkalakal DA, Namavar F, Haider H, Hanisch B, Duryee MJ, Diaz A, Rensch A, Zhang Y, Hess R, Thiele GM, Fehringer EV. Titanium implant with nanostructured zirconia surface promotes maturation of peri-implant bone in osseointegration. Proc Inst Mech Eng H 2013;227:510-22.

[48] Lengeler B. X-ray techniques using synchrotron radiation in material analysis. Adv. Mater. 1990;2:123-131.

[49] Holt M, Harder R, Winarski R, Rose V. Nanoscale Hard X-ray Microscopy Method for Materials Studies. Annu. Rev. Mater. Res. 2013;43:183-211.

[50] Yan H, Rose V, Shu D, Lima E, Kang HC, Conley R, Liu C, Jahedi N, Macrander AT, Stephenson GB, Holt M, Chu YS, Lu M, Maser J. Two dimensional hard x-ray nanofocusing with crossed multilayer Laue lenses. OPTICS EXPRESS 2011;19:15069.

[51] Rose V, Wang K, Chien T, Hiller J, Rosenmann D, Freeland JW. Preissner C, Hla S. Synchrotron X-ray scanning tunneling microscopy: Fingerprinting near to far field transition on Cu(111) induced by synchrotron radiation. Adv. Funct. Mater. 2013;23:2646-2652.

[52] Blissett RS, Rowson NA. A review of the multi-component utilization of coal fly ash. Fuel 2012;97:1-23.

[53] Bosak A, Snigireva I, Napolskii KS, Snigirev A. High resolution transmission X-ray microscopy: a new tool for mesoscopic material. Adv. Mater. 2010; 22:3256-3259.

[54] Hu Q, Ley MT, Davis J, Hanan JC, Frazier R, Zhang Y. 3D Chemical Segmentation of Fly ash particles with X-ray Computed Tomography and Electron Probe Analysis. Fuel 2014;116:229-236.

[55] Firsching M, Nachtrab F, Uhlmann N, Hanke R. Multi-energy X-ray imaging as quantitative method for material characterization. Adv. Mater. 2011;23:2655-2656.

[56] Chen Y., Geddes III JB., Yin L., Wiltzius P., Braun PV. X-ray computed tomography of holographically fabricated three-dimensional photonic crystals. Adv. Mater. 2012;24:2863-2868.

[57] Lee N, Choi SH, Hyeon T. Nano-sized CT contrast agents. Adv. Mater. 2013;25:2641.

[58] Ice GE, Budai JD, Pang JW. The Race to X-ray Microbeam and Nanobeam Science. Science 2011;334:1234-1239.

[59] Vincze L, Vekemans B, Brenker FE, Falkenberg G, Rickers K, Somogyi A, Kersten M, Adams F. Three-Dimensional Trace Element Analysis by Confocal X-ray Microfluorescence Imaging. Anal. Chem. 2004;76:6786-6791.

[60] de Jonge MD, Holzner C, Baines SB, Twining BS, Ignatyev K, Diaz J, Howard DL, Legnini D, Miceli A, McNulty I, Jacobsen CJ, Vogt S. Quantitative 3D elemental microtomography of Cyclotella meneghiniana at 400-nm resolution. PNAS 2010;107:15676-15680.

[61] Deng B, Yang Q, Du G, Tong Y, Xie H, Xiao T. The progress of X-ray fluorescence computed tomography at SSRF. Nuclear Instruments and Methods in Physics Research B 2013;305:5-8.

[62] Qiu J, Deng B, Yang Q, Yan F, Li A, Yu X. Internal elemental imaging by scanning X-ray fluorescence microtomography at the hard X-ray microprobe beamline of the SSRF: Preliminary experimental results. Nuclear Instruments and Methods in Physics Research B 2011;260:2662-2666.

[63] Remond S, Pimienta P, Bentz DP. Effects of the incorporation of Municipal Solid Waste Incineration fly ash in cement pastes and mortars I. Experimental study. Cem. Concr. Res. 2002;32:303-311.

[64] Vogt S. MAPS: A set of software tools for analysis and visualization of 3D X-ray. J. Phys. IV France 2003;104:635.

[65] Bullard JW, Jennings HM, Livingston RA, Nonat A, Scherer GW, Schweitzer JS, Scrivener KL, Thomas JJ. Mechanisms of cement hydration, Cem. Concr. Res. 2011;41:1208-1223.

[66] Scherer GW, Zhang J, Thomas JJ. Nucleation and growth models for hydration of cement. Cem. Concr. Res. 2012;42:982-993.

[67] Bullard JW. A determination of hydration mechanisms for tricalcium silicate using a kinetic cellular automation model. J. Am. Ceram. Soc. 2008;91:2088-2097.

[68] Biernacki JJ, Xie T. An advanced single particle model for C_3S and alite hydration. J. Am. Ceram. Soc. 2011; 94:2037-2047.

[69] Scrivener KL, Nonat A. Hydration of cementitious materials, present and future. Cem. Concr. Res. 2011;41:651-665.

[70] Thomas JJ, Biernacki JJ, Bullard JW, Bishnoi S, Dolado JS, Scherer GW, Luttge A. Modeling and simulation of cement hydration kinetics and microstructure development. Cem. Concr. Res. 2011;41;1257-1278.

[71] Peled A, Castro J, Weiss WJ. Atomic force and lateral force microscopy (AFM and LFM) examination of cement and cement hydration products. Cem. Concr. Compos. 2013;36:48.

[72] Garrault S, Finot E, Lesniewska E, Nonat A. Study of C-S-H growth on C_3S surface during its early hydration. Mater. Struct. 2005;38:435-442.

[73] Goto S, Daimon M, Hosaka G, Kondo R, Composition and morphology of hydrated tricalcium silicate. J. Am. Ceram. Soc. 1976;59:281-284.

[74] Richardson IG. The nature of C-S-H in hardened cements. Cem. Concr. Res. 1999;29:1131-1147.

[75] Tennis PD, Jennings HM. A model for two types of calcium silicate hydrate in the microstructure of Portland cement pastes. Cem. Concr. Res. 2000;30:855-863.

[76] Jennings HM. A model for the microstructure of calcium silicate hydrate in cement paste. Cem. Concr. Res. 2000;30:101-106.

[77] Constantinides G, Ulm F. The effect of two types of C-S-H on the elasticity of cement-based materials: Results from nanoindentation and micromechanical modeling. Cem. Concr. Res. 2004;34:67-80.

[78] Vandamme M, Ulm F, Fonollosa P. Nanogranular packing of C-S-H at substochiometric conditions. Cem. Concr. Res. 2010;40:14-26.

[79] Juilland P, Gallucci E, Flatt R, Scrivener KL. Dissolution theory applied to the induction period in alite hydration. Cem. Concr. Res. 2010;40:831-844.

[80] Bazzoni A, Cantoni M, Scrivener KL. Impact of annealing on the early hydration of tricalcium silicate. J. Am. Ceram. Soc. 2014;97:584-591.

[81] Chen JJ, Sorelli L, Vandamme M, Ulm F, Chanvillard G. A coupled Nanoindentation/SEM-EDS study on low water/cement ratio Portland cement paste: evidence for C-S-H/$Ca(OH)_2$ nanocomposites. J. Am. Ceram. Soc. 2010;93:1484-1493.

[82] Daimon M, Ueda S, Kondo R. Morphological study on hydration of tricalcium silicate. Cem. Concr. Res. 1971;1:391-401.

[83] Richardson IG. The calcium silicate hydrates. Cem. Concr. Res. 2008;38:137-158.

[84] Richardson IG. Tobermorite/jennite- and tobermorite/calcium hydroxide-based models for the structure of C-S-H: applicability to hardened pastes of tricalcium silicate, B-dicalcium siliate, Portland cement and blends of Portland cement with blast-furnace slage, metakaolin, or silica fume. Cem. Concr. Res. 2004;34:1733-1777.

[85] Diamond S. Cement paste microstructure—an overview at several levels, in: Hydraulic cement pastes: Their structure and properties. Proceedings of a conference held at the University of Sheffield, 8–9th April 1976. Cement and Concrete Association, Slough, (1976) 2–30.

[86] Gallucci E, Mathur P, Scrivener KL. Microstructural development of early age hydration shells around cement grains. Cem. Concr. Res. 2010;40:4-13.

[87] Menetrier D, Jawed J, Sun TS, Skalny J. ESCA and SEM studies on early C_3S hydration. Cem. Concr. Res. 1979;9473-482.

[88] Kumar A, Reed J, Sant G. Vertical scanning interferometry: a new method to measure the dissolution dynamics of cementitious minerals. J. Am. Ceram. Soc. 2013;96:2766-2778.

[89] Barret P, Bertrandie D. Fundamental hydration features of the major cement constituents: Ca3SiO5 and βCa2SiO4. Journal de Chimie. Physique 1986;83:765-775.

[90] Greenberg SA, Chang TN. Investigation of the colloidal hydrated calcium silicates. II. Solubility relationships in the calcium oxide-silica-water system at 25°. J. Phys. Chem. 1965;69:182-188.

[91] Taylor HFW. Hydrated calcium silicates. Part I. Compound formation at ordinary temperature. J. Chem. Soc. 1950:3682-3690.

[92] Flint EP, Wells LS. Study of the system $CaO\text{-}SiO_2\text{-}H_2O$ at 30 C and of the reaction of water on the anhydrous calcium silicates. J. Res. Natl. Bur. Stand. 1934;12:751-783.

[93] Taylor HFW. Cement chemistry, Second ed., Thomas Telford, London, 1997.

[94] Taylor HFW. Newbury DE. Calcium hydroxide distribution and calcium silicate hydrate composition in tricalcium silicate and β-dicalcium silicate pastes. Cem. Concr. Res. 1984;14:93-98.

[95] Juenger MCG, Monteiro PJM, Gartner EM, Denbeaux GP. A soft X-ray microscope investigation into the effects of calcium chloride on tricalcium silicate hydration. Cem. Concr. Res 2005;35:19-25.

[96] Silva DA, Monteiro PJM. The influence of polymers on the hydration of Portland cement phases analyzed by soft X-ray transmission microscopy. Cem. Concr. Res. 2006;36:1501-1507.

[97] Hu Q, Aboustait M, Ley MT, Hanan JC, Rose V, Winarski RP. Combined three-dimensional structural and chemistry imaging with nanoscale resolution. Acta Mater. 2014;77:173-182.

[98] Wang J, Chen-Wiegart YK, Wang J. In situ three-dimensional synchrotron X-ray nanotomography of the (De)lithiation processes in tin anodes. Angew. Chem. Int. Ed. 2004;53:4460-4464.

[99] Bernal SA, Provis JL, Rose V, Mejia de Gutierrez R, High-resolution X-ray diffraction and fluorescence microscopy characterization of alkali-activated slag-metakaolin binders. J. Am. Ceram. Soc. 2013;96:1951-1957

[100] Chae SR, Moon J, Yoon S, Bae S, Levitz P, Winarski R, Monteiro PJM. Advanced nanoscale characterization of cement based materials using X-ray synchrotron radiation: a review. Int. j. Concr. Struct. Mater. 2013;7:95-110.

[101] Gallucci E, Scrivener K, Groso A, Stampanoni M, Margaritondo G. 3D experimental investigation of the microstructure of cement pastes using synchrotron X-ray microtomography (μCT). Cem. Concr. Res. 2007;37:360-368.

[102] Trtik P, Diaz A, Guizar-Sicairos M, Menzel A, Bunk O. Density mapping of hardened cement paste using ptychographic X-ray computed tomography. Cem. Concr. Compos. 2013; 36:71-77.

[103] Pfeiffer F, Weitkamp T, Bunk O, David C. Phase retrieval and differential phase-contrast imaging with low brilliance X-ray sources. Nature Phys. 2006;2:258-261.

[104] Momose A, Takeda T, Itai Y, Hirano K. Phase-contrast X-ray computed tomography for observing biological soft tissues. Nature Medicine 1996;2:473-475.

[105] Provis JL, Rose V, Bernal SA, van Deventer JS. High-resolution nanoprobe X-ray fluorescence characterization of heterogeneous calcium and heavy metal distribution in alkali-activated fly ash. Langmuir 2009;25:11897-11904.

[106] Damidot D, Nonat A, Barrel P. Kinetics of tricalcium silicate hydration in diluted suspensions by microcalorimetric measurements. J. Am. Ceram. Soc. 1990;73:3319-3322.

[107] de Jong JGM, Stein HN, Stevels JM. Hydration of tricalcium silicate. J. Appl. Chem. 1967;17:246-250.

[108] Zhang J, Scherer GW. Comparison of methods for arresting hydration of cement. Cem. Concr. Res. 2011;41:1024-1036.

[109] Snoeck D, Velasco LF, Mignon A, Van Vlierberghe S, Dubruel P, Lodewyckx P, De Belie N. The influence of different drying techniques on the water sorption properties of cement-based materials. Cem. Concr. Res. 2014;64:54-62.

[110] Hughes DC, Crossley NL. Pore structure characterization of GGBS/OPC grouts using solvent techniques. Cem. Concr. Res. 1994;24:1255-1266.

[111] Beaudoin JJ. Validity of using methanol for studying the microstructure of cement paste. Mater. Struct. 1987;20:27-31.

[112] Beaudoin JJ, Gu P, Marchand J, Tamtsia B, Myers RE, Liu Z. Solvent replacement studies of hydrated Portland cement systems: the role of calcium hydroxide. Adv. Cem. Based Mater. 1998;56:56-65.

[113] Hubbell J. Photon Mass Attenuation and Energy-Absorption Coefficients from 1 keV to 20 MeV. Int. J. Appl. Radiat. Isot. 1982;33:1269-1290.

[114] Liu Y, Meirer F, Williams PA, Wang J, Andrews JC, Pianetta P. TXM-Wizard: a program for advanced data collection and evaluation in full-field transmission X-ray microscopy. J. Synchrotron Rad. 2012;19:281-287.

[115] Henke BL, Gullikson EM, Davis JC. X-ray interactions: photoabsorption, scattering, transmission, and reflection at E=50-30000 eV, Z=1-92. Atomic Data and Nuclear Data Tables 1993;54:181-342.

[116] Thomas JJ, Jennings HM, Allen AJ. The surface area of cement paste as measured by neutron scattering: evidence for two C-S-H morphologies. Cem. Concr. Res. 1998;28:897-905.

[117] Garrault-Gauffinet S, Nonat A. Experimental investigation of calcium silicate hydrate (C-S-H) nucleation. J. Crystal Growth 1999;200:565-574.

[118] Gartner EM, Jennings HM. Thermodynamics of calcium silicate hydrates and their solution, J. Am. Ceram. Soc. 1987;80:743-749.

[119] Taylor HFW, Barret P, Brown PW, Double DD, Frohnsdorff G, Johansen V, Menetrier-Sorrentino D, Odler I, Parrott LJ, Pommersheim JM, Regourd M, Young JF. The hydration of tricalcium silicate. Materiaux et Constructions 1984;17:457.

[120] Scrivener KL, Juilland P, Monteiro JM Advances in understanding hydration of Portland cement. Cem. Concr. Res.2015;78:38-56.

[121] Lasaga AC, Luttge A. Variation of crystal dissolution rate based on a dissolution stepwave model. Science 2001;291:2400-2404.

[122] Dove PM, Han N. Kinetics of mineral dissolution and growth as reciprocal microscopic surface process across chemical driving force. AIP Conference Proceeding 2007;916:215-234.

[123] Dove PM, Han N., De Yoreo JJ. Mechanisms of classical crystal growth theory explain quartz and silicate dissolution behavior. PNAS 2005;102:15357-15362.

[124] Makar JM, Chan GW. End of induction period in ordinary Portland cement as examined by high-resolution scanning electron microscopy. J. Am. Ceram. Soc. 2008;91:1292-1299.

[125] Juilland P, Gallucci E. Morpho-topological investigation of the mechanisms and kinetic regions of alite dissolution. Cem. Concr. Res. 2015;76:180-191.

[126] Fierens P, Verhaegen JP. Induction period of hydration of tricalcium silicate. Cem. Concr. Res. 1976;2:287-292.

[127] Makar JM, Beaudoin JJ, Sato T, Alizadeh R, Raki L. Discussion of "Dissolution theory applied to the induction period in alite hydration." Cem. Concr. Res.2011;41:565-567.

[128] Jennings HM. Aqueous solubility relationships for two types of calcium silicate hydrate. J. Am. Ceram. Soc. 1986;69:614-618.

[129] Hou P, Kong D, Kawashima S, Qian J, Corr DJ, Shah SP. A novel evidence for the formation of semi-permeable membrane surrounding the Portland cement particles during the induction period. J Therm Anal Calorim 2013;113:881-884.

[130] Gartner E. Discussion of the paper "Dissolution theory applied to the induction period in alite hydration" by P. Juilland et al., Cem. Concr. Res. 40 (2010) 831-844. Cem. Concr. Res. 2011;41:560-562.

[131] Bellmann F, Sowoidnich T, Ludwig H, Damidot D. Dissolution rates during the early hydration of tricalcium silicate. Cem. Concr. Res. 2015;72:108-116.

[132] Kjellsen KO, Lagerblad B. Microstructure of tricalcium silicate and Portland cement system at middle of hydration-development of Hadley grain. Cem. Concr. Res. 2007;37:13-20.

[133] Kjellsen KO, Justnes H. Revisiting the microstructure of hydrated tricalcium silicate –a comparison to Portland cement. Cement & Concrete Composite 2004;26:947-956.

[135] Shirato N., Cummings M., Kersell H., Li Y., Stripe B., Rosenmann D., Hla S.W., Rose V. Elemental Fingerprinting of Materials with Sensitivity at the Atomic Limit. Nano Letters 2014;14:6499-6504.

[136] Hu Q, Aboustait M, Kim T, Ley MT, Hanan JC, Bullard J, Winarski R, Rose V. Direct three-dimensional observation of the microstructure and chemistry of C_3S hydration. Submitted.

[137] Allen AJ, Thomas JJ, Jennings HM. Composition and density of nanoscale calcium-silicate-hydrate in cement. Nature Materials 2007;6:311-316.

[138] Richardson IG. Model structures for C-(A)-S-H (I). Acta Cryst. 2014;B70:903.

[139] Jennings HM, Thomas JJ, Gevrenov JS, Constantinides G, Ulm F. A multi-technique investigation of nanoporosity of cement paste. Cem. Concr. Res.2007;37:329-336.

[140] Richardson IG., Groves GW. Models for composition and structure of calcium silicate hydrate (C-S-H) gel in harden tricalcium silicate pastes. Cement and Concrete Research 1992;22:1001-1010.

[141] Barret P, Menetrier D, Bertrandie D. Mechanism of C_3S dissolution and problem of the congruency in the very initial period and later on. Cem. Concr. Res.1983;13:728-738.

[142] Nicoleau L, Nonat A, Perrey D. The di- and tricalcium silicate dissolutions. Cem. Concr. Res. 2013;47:14-30.

APPENDICES

Appendix-A

Parametric Study of μCT Settings to optimize Image quality

Scans were made at 0.3º of rotation step over 180o and with a 4 frame/step averaging rate. In all scans, the voltage was modified so that a transmission rate of 27.5% was required at the center of the particle. The minimum transmission was used as opposed to voltage or power because each fly ash particle may be of different composition and size. Radiographs of 1000 pixel x 1000 pixel were used to create tomography models for the trials with a 5 μm voxel size. Scans were done with the filters of 0.5 mm aluminum, 0.5 mm aluminum with 0.5 mm copper, and none. Filters absorb lower energy X-rays and allow high energy X-rays to interact with the sample. This narrows the bandwidth of the X-ray source reducing spurious signals to the X-ray detector improving image quality. The benefit depends on the need to detect low absorption phases.

Tomography cross section images were evaluated for the presence of beam hardening artifacts and overall contrast of the images. For each evaluation, a quantitative comparison was made of the gray scale histogram. The 0.5 mm aluminum filter was found to provide the best reduction in artifacts and overall quality of image. Next X-ray transmission rates between 20% and 40% were investigated for the sample to compare contrast and the quality of the radiographs. A transmission rate of 28% +/- 3% (one standard deviation) at the center of the particle was optimal for the materials, detector, and equipment.

Electron Probe Microanalysis

Once polished, the exposed surface is then imaged with the backscatter electron detector and a Bruker Quad 4040 x-ray energy dispersive spectrometer (EDS). All x-ray data were taken using the JEOL 8500f electron microprobe at 20 keV accelerating voltage, with 50 nA of probe current. These settings produced a stored count rate of approximately 100,000 counts/s. The standards were collected at similar conditions, although the probe current was decreased on the pure elemental standards. The per-pixel dwell time was adjusted on each map to provide at least 20,000 counts in each spectrum. Dwell times were generally approximately 100 ms/pixel. The X-ray data are collected and stored in a hyperspectral, binary data cube with a full X-ray spectrum at each point. First order approximations based on Monte Carlo calculations that 95% of the elemental x-rays were produced in the first 4 μm of the sample surface, although higher energy bremsstrahlung x-rays were produced from a larger area. For all particles studied, the

experimental conditions were held constant.

Unsupervised Classification of Electron Probe Microanalysis Data

To find these unique constituents, the data were first processed using DTSA II to convert the x-ray spectral data into compositional data through the use of a suite of pure elemental and mixed compositional standards [1]. Then, multivariate statistical analysis is performed on the data to reduce it to a few high variability vectors [2]. While many data transformations exist that can provide unsupervised classification (e.g., k-means, principle component analysis, or agglomerative nesting, etc.), the scheme chosen was known as ISO Means, and is part of the hyperspectral analysis program called ENVI [3]. The ISO means method uses principle components and k-means clustering in addition to in-class statistical controls to identify compositionally distinct areas. Pixels with high variability were separated out into an "unclassified" group. Subsequent analysis of "unclassified" pixels indicates that the high variability on some samples was due to high surface topography. It should be noted that larger fly ash particles are far more likely to contain large air bubbles, which, when cross sectioned, show up as sizeable depressions in the images and unclassifiable pixels. Therefore, unclassified regions should reduce on smaller or more homogeneous phases.

Details of chemical phases from EPMA

A summary of the chemical phases found are included in Table A1. The weight percentage is given for each element, as well as the percentage on the cross section investigated, and the calculated mass absorption coefficient. The mass absorption was calculated from the elemental makeup and by using NIST X-ray Attenuation Databases [4].

Fusion Electron Probe Microanalysis and micro Computed Tomography Datasets

The accuracy of the match is determined by comparing the coordinates of feature specific pixels. If the compared features in both EPMA and □CT were found to have the same normalized coordinate then it is considered to be a good match. The matching accuracy is estimated by the number of matched pixels divided by the total number of feature specific pixels compared.

Analytically peeling algorithm

The demonstration of shells or layers for 3D constituent analysis is shown in Fig A.1. Even through the fly ash particle is quite spherical, the algorithm needs to capture the irregularity of the geometry in order to have uniform thickness of the layers. The 3D information of the particle boundary was first obtained by imaging processing techniques such as edge detection or threshold of the foreground. Next, a 3D layer is defined by inner side and outer side of the boundary. Both of them are shrinked versions of the original particle boundary. The thickness of the layer is controlled by the difference of shrinkage ratios between two boundaries. The difference between inner and outer boundary ratio is 0.01 in order to produce 1 μm thick layer. All the voxels inside the layer were classified to chemical phases based on the segmentation ranges established by TACCo. The plots of different phase constituents over depth can thus be obtained by analyzing the successive layers from the surface to the core with successive shrinkage ratio from 1 to 0.1.

Details Description of Data Fusion

For Particle 1C the limits for the red phase was found to be between a gray value of 150 and 71. This is two standard deviations from the mean towards the high absorption phase and one standard deviation towards the overlapping constituents. Next the air phase was established to be a gray value of 20. This is one standard deviation from the mean. The green phase was taken to be values between 71 and 37. The 37 was chosen as it was one standard deviation from the mean towards the overlap and the 71 limit was established from the red constituent. The remaining gray values between 20 and 37 will be treated as a mixture.

TACCo

The algorithm of Tomograhy assisted chemical correlation (TACCo) is to find a corresponding cutting slice in the mCT dataset that could match with polished surface of sub sequential SEM/EDS analysis. The evaluation of the matching based on the selected feature points that exist in both datasets. These feature points could be the regions of voids or heavy metals or other materials that are easy for segmentation in both mCT and SEM/EDS datasets.

The morphology of the randomly polished surface in 3D mCT space is approximated using a composite plane, which contains eight adjustable octants as shown in Fig A.2. This composite plane has 13 parameters, which include the x and y coordinates and the height of the centroid node (x, y, Z_C), and the heights of eight perimetric nodes (Z_1 to Z_8). The heights of these nodes are related to the indice of slice images in the mCT datasets, since each slice image could be consider as a horizontal cutting plane at a certain height of the sample. The x, y coordinates are related to the spatial location within a 2D slice image.

To begin with, a visual inspection could find a similar slice image in the original mCT dataset, which could match many selected features in the SEM/EDS analysis. The index of this slice image is used as the initial values for height of all the nodes (Z_C, Z_1 to Z_8) for next iteration process. Furthermore, the location of centroid of the sample in this slice image can be set as the x and y coordinates of the centroid node of the composite plane.

To determine the heights of the nodes and to find the morphology of the composite plane in the 3D mCT space, an iterative approach is used by adjusting each octant plane so that all the features from SEM/EDS analysis could get matches. First, the orientation of the first octant plane Q1 can be determined by optimizing the feature alignment by changing the height of Node 2 (Z_2) while keeping Centroid node and and Node 1 constant for their heights (Z_C, Z_1). After Z_2 gets updated, the orientation of second octant plane Q2 can be adjusted by changing the height of Node 3 (Z_3) based on the updated Z2 and the height of the centroid Z_C. This process will continue for all eight octant planes to update the heights of Node 2 to 8 (Z_2 to Z_8). By finding the orientation of Q8, the height of Node 1 (Z_1) can be updated that is the end of the first iteration. Then, the second iteration starts using the updated Z_1 to find the orientation of the first octant Q1 by adjusting Z_2. The iterations will terminate until all the heights of the perimetric nodes get converged. Then, morphology of this composite plane can be obtained by interpolating the height values for the region within each octant plane using the heights of its three nodes. If sometime the converged

composite plane does not fit well for all features, a different height of the centroid Z_C may be used to repeat the iteration.

Reference

[1] Ritchie, N. DTSA II [Software]. 2008. Retrieved from Public Domain. Software available from the NIST:http://www.cstl.nist.gov/div837/837.02/epq/dtsa2/index.html Gaithersburg, MD: National Institute of Standards and Technology.

[2] Kotula PG, Keenan MR, Grant RP, Hlava PF. Multivariable Statistical Analysis of Wavelength and Energy Dispersive X-ray Spectral Image. Microsc Microanal 2004;10:118-119.

[3] Exelis Visual Information Solutions. ENVI: Environment for Visualizing Images [software]. 2012. Software available from the Exelis Visual Information Solutions company: www.exelisvis.com.

[4] Hubbell JH. Photon Mass Attenuation and Energy-Absorption Coefficients from 1 keV to 20 MeV. Int. J. Appl. Radiat. Isot.1982;33:1269-1290.

Table A.1 – Summary of the Different Compositions Observed with the EPMA.

element		Ca	Si	Al	Fe	O	K	Mg	S	Ti	area % on cross section	mass absorption[a] (cm^2/g)
Particle 1C - 427 µm diameter												
yellow	weight %	9.66	10.10	6.72	67.17	3.56	0.34	1.31	0.47	0.67	2.52	6.50
	1σ	7.05	6.64	4.62	12.46	6.12	0.51	1.61	0.93	0.97		
red	weight %	27.87	22.96	12.38	10.88	20.00	0.32	3.19	0.55	1.86	70.60	2.76
	1σ	6.78	5.90	3.49	7.87	9.98	0.46	1.68	0.61	1.12		
blue	weight %	4.36	29.35	31.00	14.59	19.11	0.35	0.56	0.27	0.41	5.82	2.15
	1σ	6.69	8.81	8.40	13.75	12.09	0.64	1.22	0.47	0.69		
green	weight %	1.08	65.21	0.53	1.29	31.29	0.07	0.17	0.12	0.26	21.05	1.09
	1σ	2.70	7.22	1.10	2.99	6.67	0.33	0.34	0.25	0.56		
Particle 2C - 427 µm diameter												
cyan	weight %	12.54	32.83	12.27	8.25	26.97	3.47	1.47	0.42	1.78	5.23	3.57
	1σ	5.40	9.78	5.99	6.87	9.88	2.02	0.93	0.63	2.10		
red	weight %	24.99	19.94	11.69	12.67	24.00	0.69	3.15	0.99	1.88	83.51	2.73
	1σ	6.56	4.87	2.78	5.26	10.01	0.59	1.07	1.11	1.06		
peach	weight %	15.24	11.50	14.12	28.64	21.05	0.63	6.00	1.39	1.43	6.09	2.44
	1σ	4.99	4.83	4.89	13.20	10.42	0.61	2.71	1.37	1.06		
gray	weight %	21.02	13.33	24.50	10.22	20.72	0.82	2.12	5.82	1.44	0.73	2.09
	1σ	14.34	9.90	14.26	7.74	13.33	0.82	1.86	8.35	1.66		
green	weight %	3.47	58.98	1.81	3.58	30.43	0.34	0.42	0.35	0.62	4.44	1.08
	1σ	3.88	9.99	1.93	4.46	8.91	0.55	0.50	0.74	1.15		
Particle 4C - 615 µm diameter												
forest green	weight %	19.94	51.22	9.64	7.06	5.50	2.23	2.21	0.48	1.71	0.61	2.54
	1σ	12.44	16.12	4.79	4.81	7.90	1.85	1.53	0.57	1.24		
red	weight %	21.69	26.69	10.16	6.39	29.77	0.62	3.12	0.19	1.36	88.10	2.16
	1σ	3.40	3.59	1.56	2.38	6.73	0.44	0.60	0.22	0.66		
brown	weight %	6.56	36.42	15.08	3.81	33.30	2.54	0.93	0.17	1.19	3.47	1.70
	1σ	4.97	8.03	6.72	5.70	8.76	1.19	0.75	0.22	0.88		
purple	weight %	18.82	27.55	18.86	3.41	29.41	0.26	0.99	0.16	0.54	1.54	1.34
	1σ	4.22	3.40	3.25	1.68	7.28	0.35	0.56	0.23	0.51		
green	weight %	1.55	56.17	1.42	1.23	38.52	0.37	0.26	0.13	0.35	6.29	1.00
	1σ	2.44	6.85	1.67	2.20	5.90	0.63	0.37	0.18	0.53		

[a] These values have been calculated based on the chemical makeup of the constituent by using NIST X-ray attenutation databases [4]

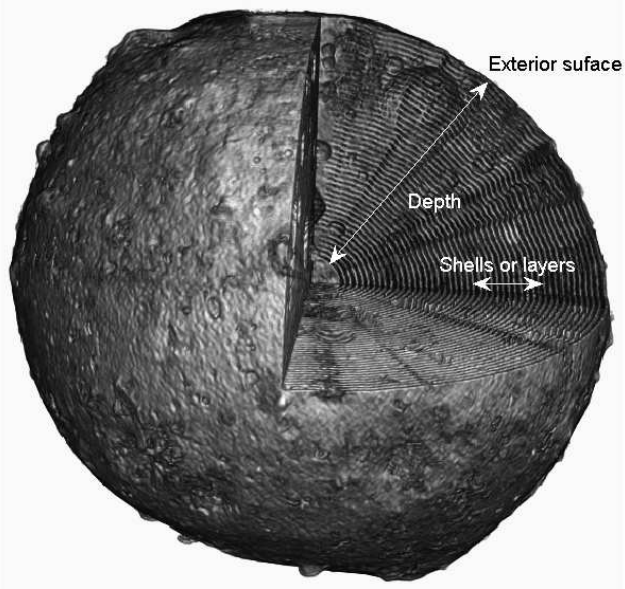

Fig A.1 – Shells or layers with 1 μm uniform thickness parallel to the particle surface was analytically peeled from exterior surface at different depths.

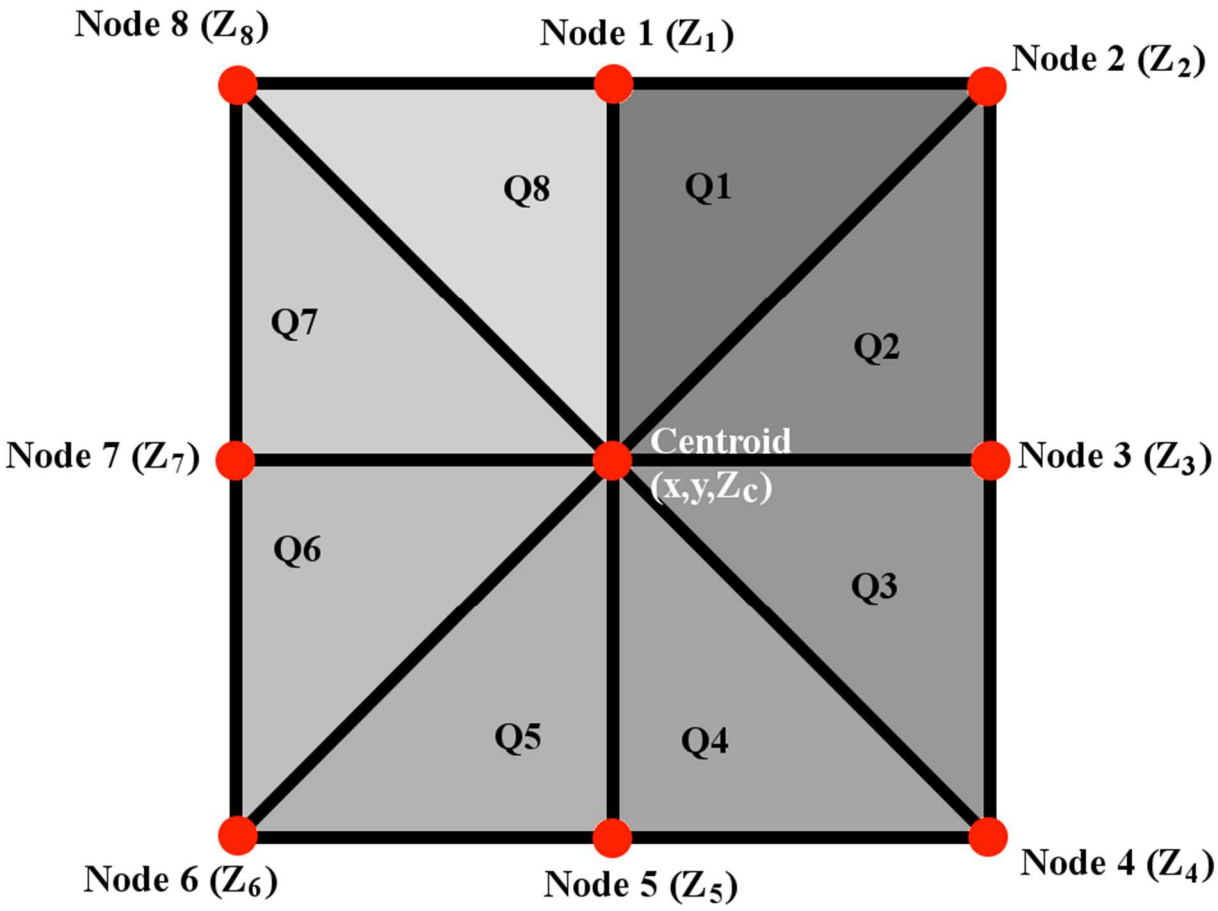

Fig A.2 – An overview of the composite plane for approximating the polished surface, which contains eight adjustable octant planes.

Appendix-B

ICP-OES and XRD

In the ICP-OES analysis, the test solution was diluted by a factor of 10 (by mass) in 5 % nitric acid solution, then nebulized and injected to a plasma field. A charge-coupled device (CCD) recorded the intensity of different spectral lines associated with each of the elements that were being analyzed. The intensities (counts per second) for each element were converted to ppm concentrations and corrected for the dilution by comparing the intensities to intensities recorded for a dilution series of known solutions that were made in advance for the purpose. For this solution, the elements of Al, Ca, Mg, Si, and Sr were analyzed. The elements scanned but not observed are: Ba, Cd, Ce, Co, Cr, Cu, Fe, Hf, K, Li, Mn, Mo, Na, Ni, P, S, Ti, V, Zn, and Zr.

The XRD result in Fig B.1 confirms that the triclinic C_3S is consistent with the polymorphs described in the literature [29]. A plot has been shown with the ICDD data (card # 00-031-0301) superimposed over the measurement.

PSD

An overview of the method is shown in Fig C.2. The powder is mixed with a non-reactive solution, dispersed by ultrasonic agitation, and then placed on double-sided carbon tape. This material is then placed on an aluminum stub and analyzed. The particle shape, size, and chemistry are then measured on 4000 individual particles. This technique is rapid and able to measure about 500 particles per hour. The result is given in Fig B.3, which shows 95 % of the C_3S particles within the size range from 1 μm to 7.5 μm. More details about this technique can be found in other publications [S1].

Calorimetry

The mixing procedure used to generate the calorimetry data in Fig. 1 is listed below because calorimetry measurements on cement pastes are known to be sensitive to prior mixing. Mixing was performed using a high vibration mixer.

1. Transfer 2 g of cement into a calorimetry vial.

2. Transfer prescribed masses of chemicals and water into a separate vial.

3. Add the water with chemicals into the cement vial.

4. Use a small disposable wooden stick/applicator and stir 10 times clockwise and 10 times counter clockwise. This operation should take about 10 s. Do not re-use the wooden applicator as nucleation can be accidentally introduced.

5. Put the cap on the vial and tighten it.

6. Place the vial on the mixer sample holder.

7. Cover the sample with the top holder and attach the rubber band to secure the vial.

8. Set the mix speed to 1000 rotations per minute.

9. Press the "On/Off" button once and select continuous mode to begin mixing.

10. Remove the vial from the mixer immediately after 3 min and put the vial into the calorimeter.

nCT data analysis

Due to the fine length scale, the samples underwent significant displacement during the scan that were caused by the imperfection and thermal expansion of the stages. These shifts were compensated with a laser tracking system [2S]. The radiographs had to be aligned with a reference point in order to be reconstructed for tomography. The object, chosen as reference point, had to appear in all radiographs and its location had to be precisely identified. To do so, the regions of needle were used. After reconstruction, in order to compare the same regions from the tomography datasets before and after hydration, the coordinate systems of two datasets had to be aligned. Since the tip of needle was reliable and existed in all scans, it was used as reference point in the registration of coordinates.

Two different reconstruction algorithms were used in this study with the TXM wizard software [3S]. A back projection (BP) algorithm was applied on the reconstruction of samples 1C, 2C, 4C and 5C, which gave better contrast of absorption. Filtered back projection (FBP) algorithm was applied on the reconstruction of sample 3C due to its highly noisy background in order to enhance the phase contrast in the images.

The segmentation scheme of the tomography datasets was mainly established based on the perceivable edges. In order to get reliable results, each edge on one slice was identified by its proximity to the edges in neighbor slice images.

Sample 5C

The radiographs and tomography slice images of sample 5C are given in Fig. B.4. This sample shows great volume expansion after seven hours of hydration at 25 ^{o}C. This agrees with the observation from 4C. The gold balls used as fiducial markers were originally below the tip of the needle, but have widely spread over the entire sample during the expansion in the hydration process. These fiducial markers cause severe artifacts in the image as they have significantly larger X-ray absorption (attenuation) than the surrounding materials. That makes the quality of this tomography dataset too poor to be used for segmentation of the remaining C_3S and hydration product. However, the borders between the sample and air can still be perceived if a gamma correction reconstruction algorithm is used. The overall dimensions and volume of the sample after hydration can still be obtained as given in Table 5.2.

nXRF maps of the sample 4C after rotating 90^{o} from Fig 4.9

The unexpectedly high Ca/Si of region D of C_3S in Fig 4.9, Sample 4C was investigated further by rescanning with nXRF after a 90° rotation of the sample relative to that in Fig 4.9. The Ca, Si, Ca/Si and segmentation maps were established in the same manner as Fig 4.9 and are shown in Fig B.5. The segmentation of the phases was established using the same manner as Fig 4.9. Since each pixel counts the materials through the depth for the elemental concentrations, the phases distributed along the horizontal direction of the perpendicular maps in Fig B.5 could correspond to the possible phases in the depths of the pixels in the maps of Fig 4.9. The responsible sections for regions C and D from Fig 4.9 are shown in the segmentation map. It reveals that the section of region D has some areas of CH adjacent to the regions of C_3S along the horizontal direction but the section of region C does not. It is quite possible that the pixels in region D of C_3S of Fig 4.9 include not only C_3S phase but also some proportion of CH, which could make the Ca/Si high.

References

[1S] M. Aboustait, Q. Hu, R. Frazier, Y. Zhang, B. Tabb, T. Ley, J. Hanan, Innovative prediction of fly ash performance in concrete, Oklahoma Transportation Center Report (2013).

[2S] Q. Hu, M. Aboustait, M.T. Ley, J.C. Hanan, V. Rose, R.P. Winarski, Combined three-dimensional structural and chemistry imaging with nanoscale resolution, Acta Mater. 77 (2014) 173-182.

[3S] Y. Liu, F. Meirer, P.A. Williams, J. Wang, J.C. Andrews, P. Pianetta, TXM-Wizard: a program for advanced data collection and evaluation in full-field transmission X-ray microscopy, J. Synchrotron Rad. 19 (2012) 281-287.

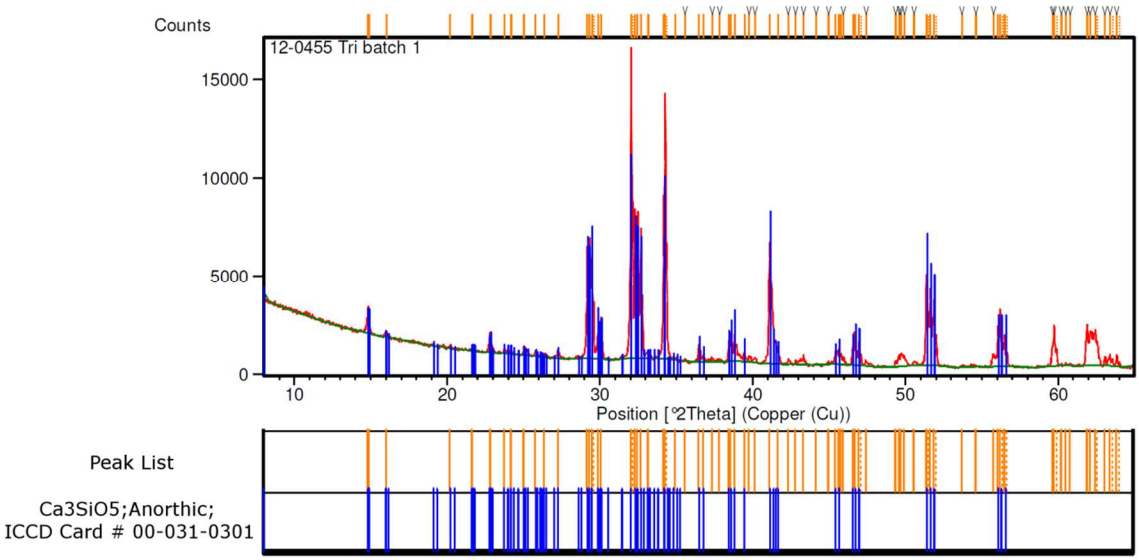

Fig B.1 – XRD analysis of triclinic C_3S powders.

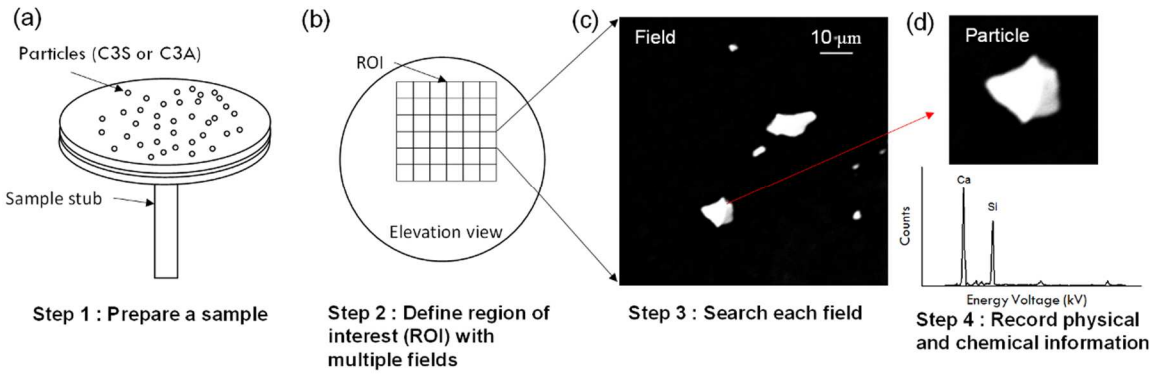

Fig B.2 – An overview of the ASEM method that outlines the sample preparation, visual analysis and chemical analysis of the particles.

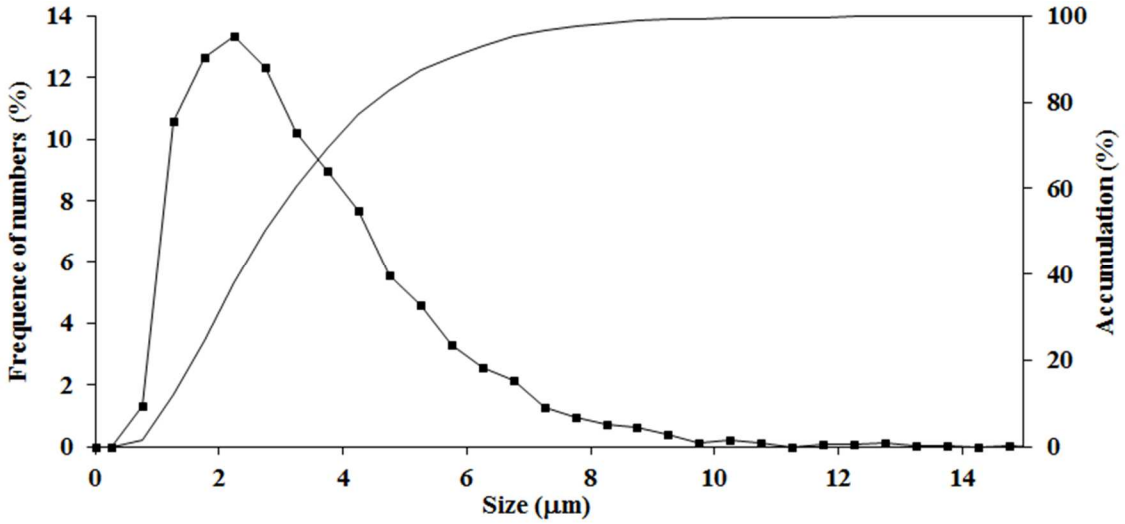

Fig B.3 – The particle size distribution by ASEM analysis.

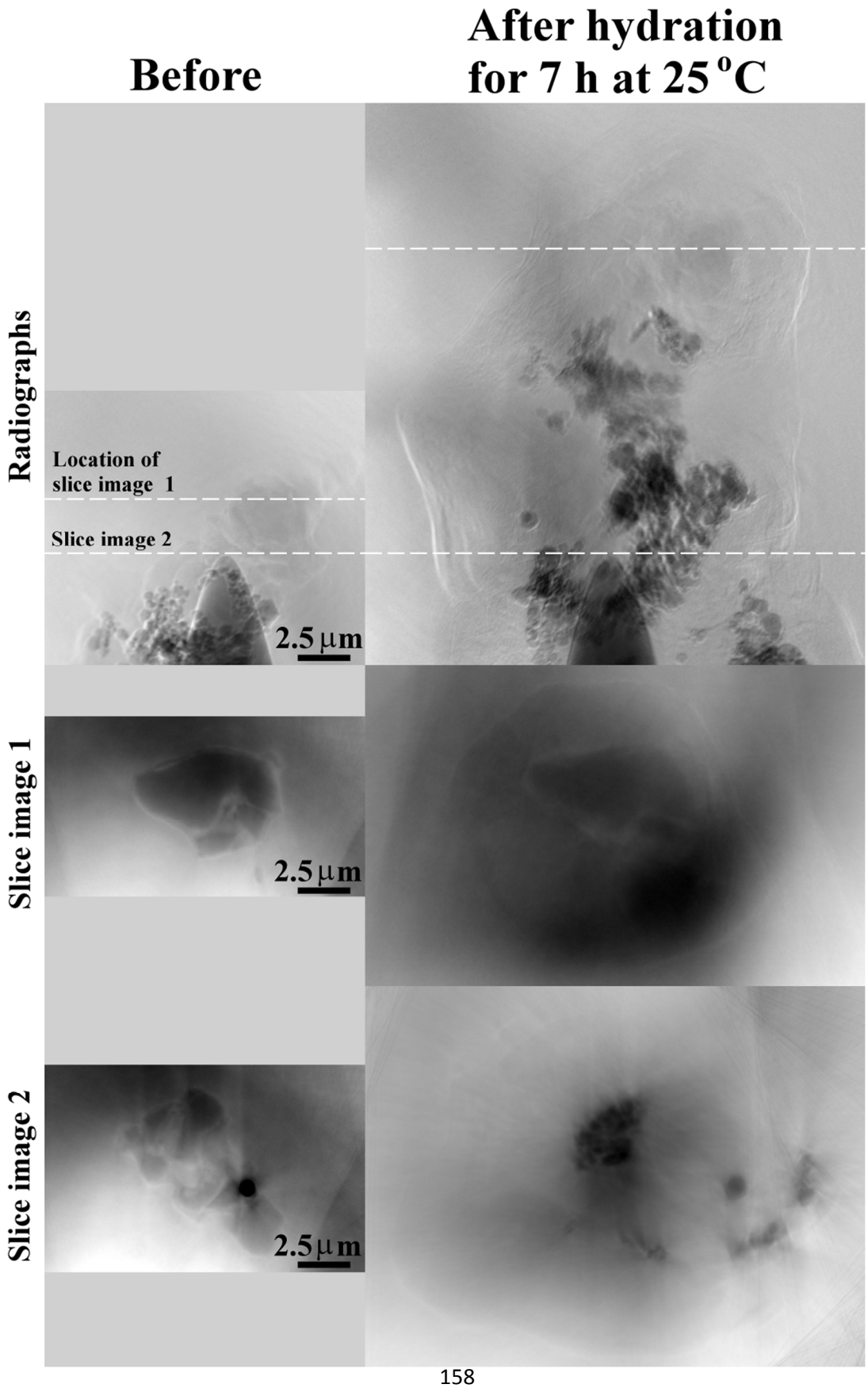
Before
After hydration for 7 h at 25 °C
Radiographs
Location of slice image 1
Slice image 2
2.5 μm
Slice image 1
2.5 μm
Slice image 2
2.5 μm

Fig B.4 – Radiographs and tomography slices for sample 5C with hydration period of seven hours at 25 ^{o}C.

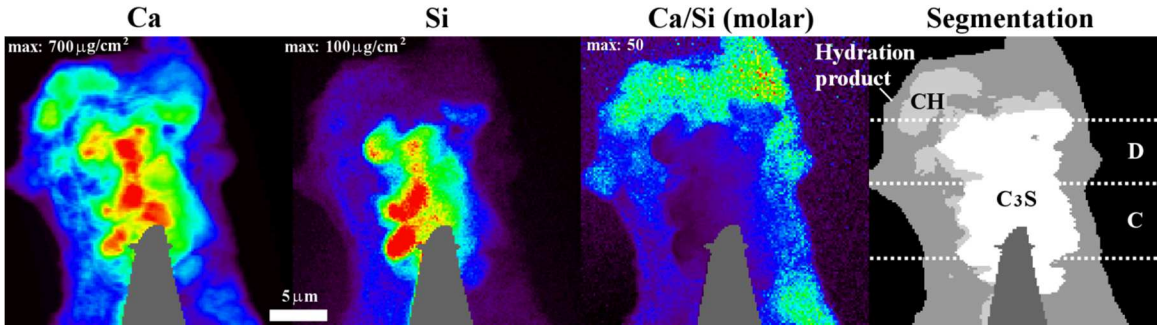

Fig B.5 – The nXRF maps of Sample 4C after rotating 90º from Fig 4.9.

Appendix-C

The 3D registration of Individual particles

To align the 3D datasets from two scans for one particle, three translation factors (x,y,z) and three rotation factors (Θx. Θy, Θz) need be determined. By assuming the majority of features on the particle, such as overall boundary and volume, still remain unchanged, these factors can be determined by examining different combinations of these factors and applying them on the datasets of "After" in order to match the dataset of "Before". The match of two data sets after applying those movement factors is verified by comparing the 2D projections of the modified 3D dataset of "After" with "Before" . The 2D projection is produced by mapping the 3D datasets as the summation of voxels along a certain orientation, which is similar to the radiograph with the details provided in the previous publication. First, the match is achieved by making the 2D projection of two datasets at 0 degree orientation. Then, these movement factors are validated using 90 degree orientation for 2D projection.

nCT datasets for Particle 5,6,7

The nCT datasets for Particle 5, 6 and 7 are presented Fig C.1, C.2 and C.3, with the same manner as Fig 5.4.

The distribution of depth of reaction along the norm of the surface

A second approach was developed by measuring the depth of reaction along the norm to the surface. In order to calculate the norm direction for any voxel on the surface, the neighbor voxels round it have to be included for approximating the tangential surface. If the adjacent voxels within 1 voxel distance are only used, the calculation of norm will usually result a singularity that makes majority of the surface not available for finding the norm. To find the norm for the most voxels on the surface, the neighbor voxels of the surface within 3 voxels distance are included for the calculation.

The distributions of reaction depth for seven particles are given in Fig C.4, and their means and standard deviations are given in Table C.2 together with the results from the first approach. In comparing with the first approach, the second one shows similar shapes of distributions for most particles. The average and standard deviation is usually higher than the first approach. It should be mentioned that the depth for Particle 3 is quite different from the first approach. That is because the high degree of reaction on this particle would make the distance of modified region along the norm direction go through the entire particle, making the measurement not representative as depth of reaction.

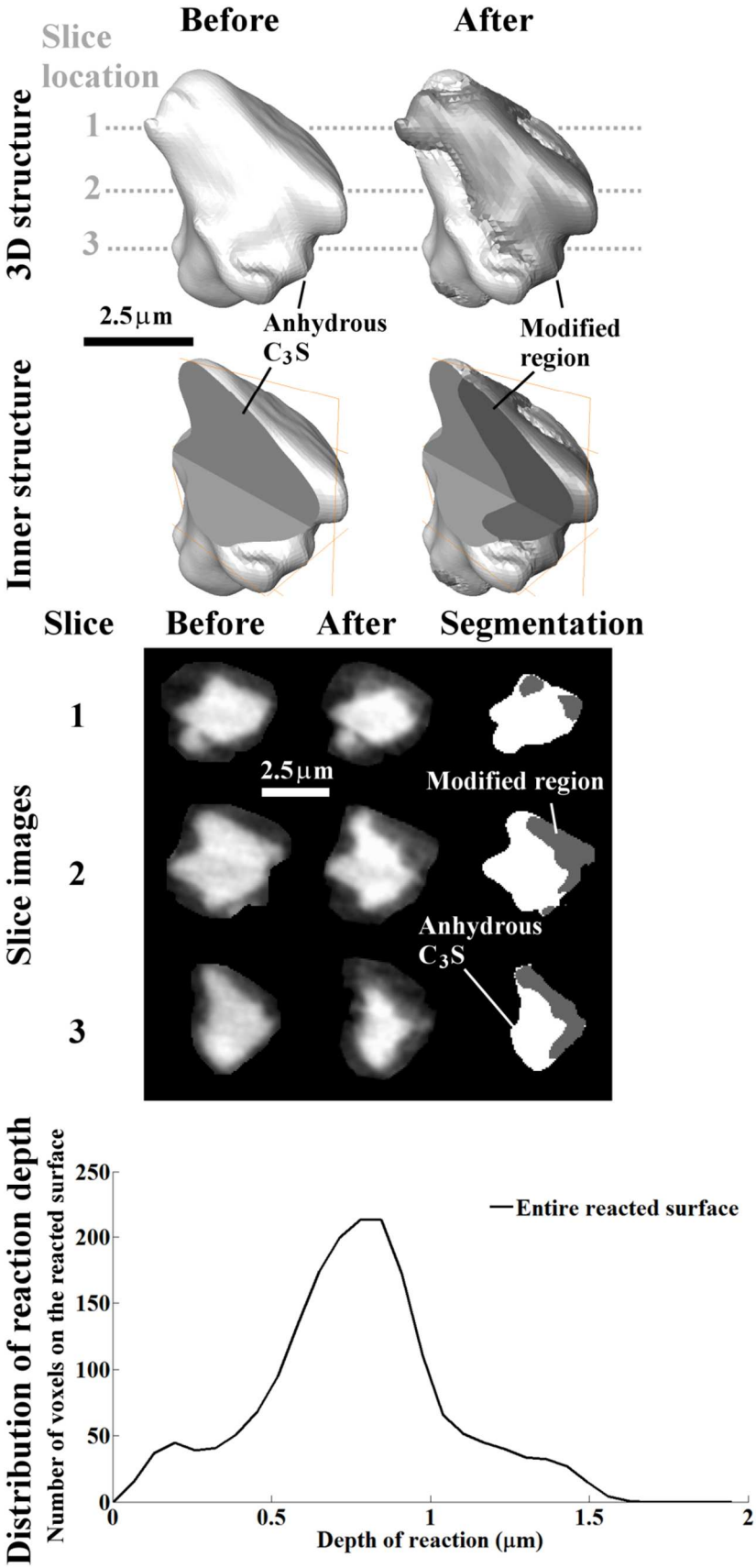
Before
After
Slice location
1
2
3
3D structure
2.5μm
Anhydrous C3S
Modified region
Inner structure
Slice
Before
After
Segmentation
Slice images
1
2
3
2.5μm
Modified region
Anhydrous C3S
Distribution of reaction depth
Number of voxels on the reacted surface
250
200
150
100
50
0
0
0.5
1
1.5
2
Depth of reaction (μm)
Entire reacted surface

Fig C.1 – The nCT datasets for Particle 5

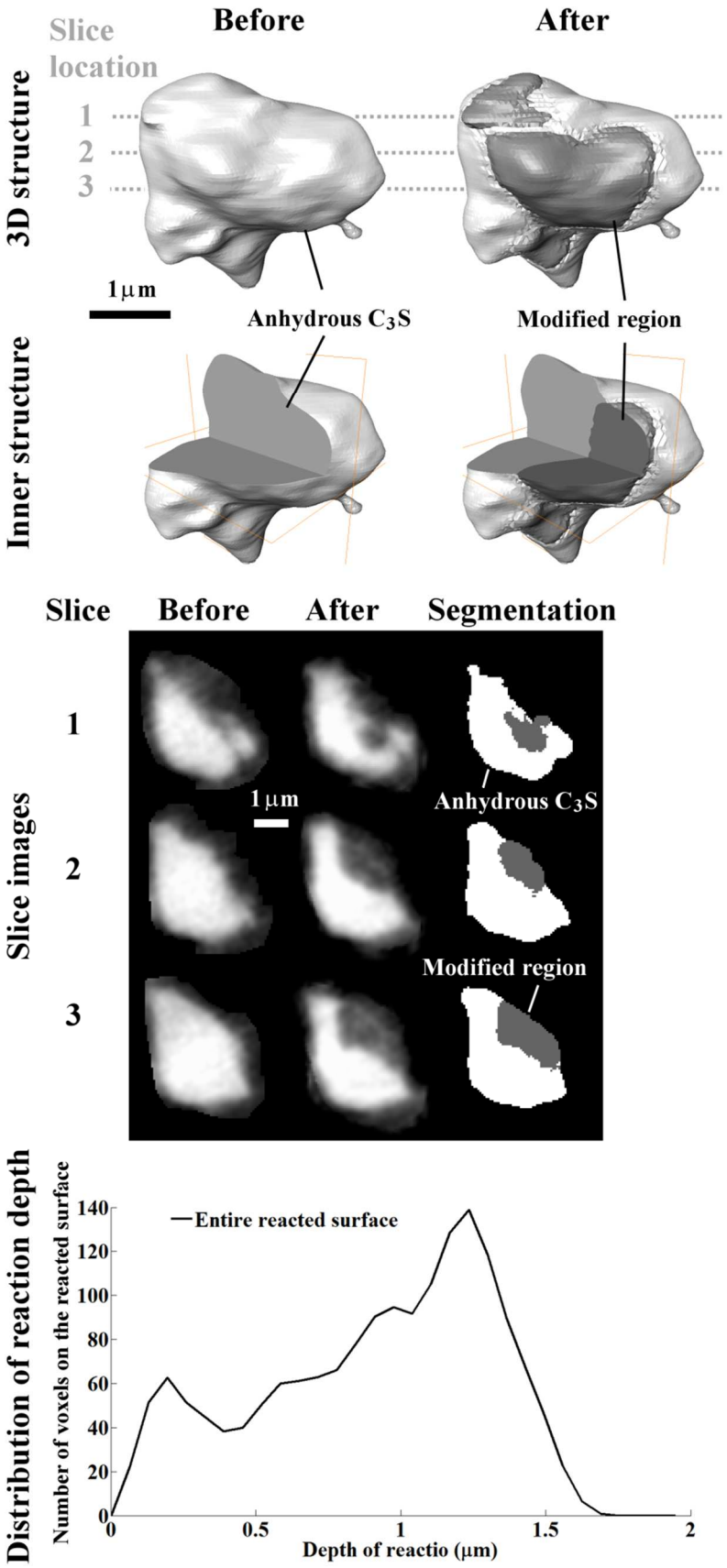
Before
After
Slice location
1
2
3
3D structure
1μm
Anhydrous C3S
Modified region
Inner structure
Slice
Before
After
Segmentation
Slice images
1
2
3
1μm
Anhydrous C3S
Modified region
Distribution of reaction depth
Number of voxels on the reacted surface
Entire reacted surface
140
120
100
80
60
40
20
0
0
0.5
1
1.5
2
Depth of reactio (μm)

Fig C.2 – The nCT datasets for Particle 6

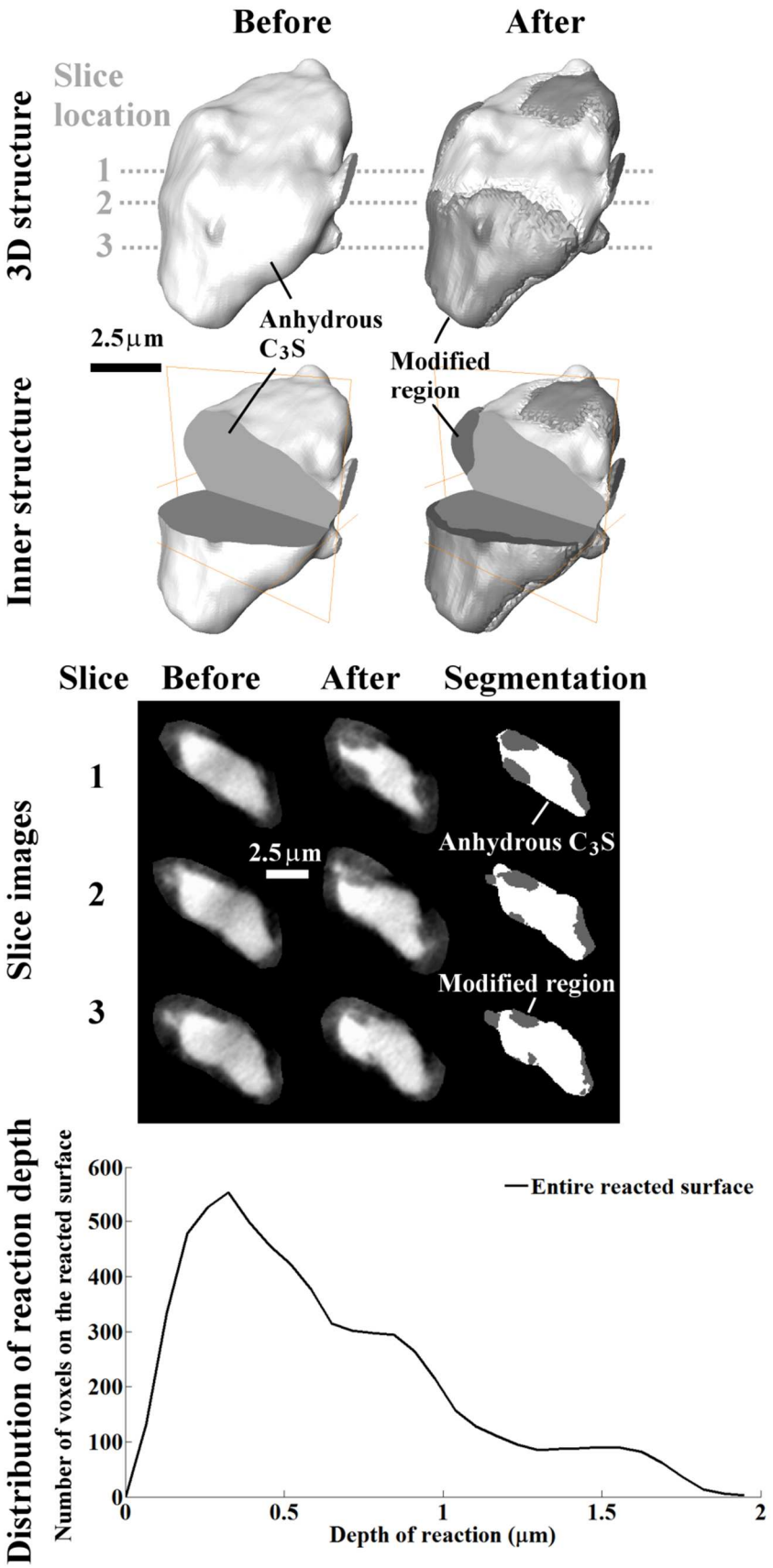
Before
After
3D structure
Slice location
1
2
3
Anhydrous C3S
2.5μm
Modified region
Inner structure
Slice
Before
After
Segmentation
Slice images
1
2
3
2.5μm
Anhydrous C3S
Modified region
Distribution of reaction depth
Number of voxels on the reacted surface
600
500
400
300
200
100
0
0
0.5
1
1.5
2
Depth of reaction (μm)
Entire reacted surface

Fig C.3 – The nCT datasets for Particle 7

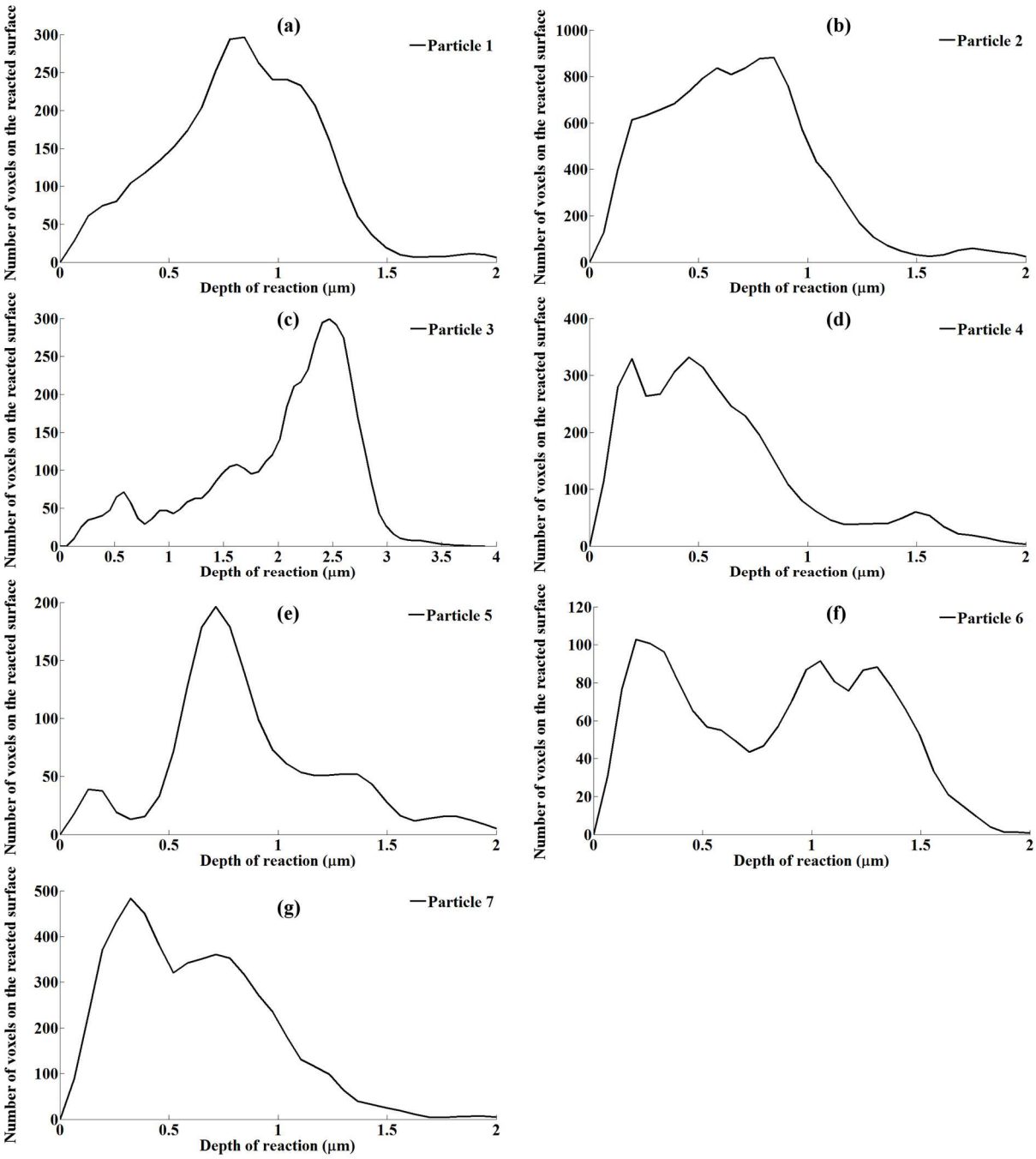

Fig C.4 – The distributions of reaction depth for particles 1 to 7 given in (a) – (g), using the measurement along the orientation perpendicular to the surface.

Table C.1 – The comparisons of mean and standard deviation of the reaction depths measured between first and second approaches.

Particles	Depth of reaction (μm)			
	First approach		Second approach	
	Mean	STD	Mean	STD
1	0.61	0.29	0.8	0.34
2	0.64	0.35	0.64	0.35
3	1.4	0.3	1.97	0.69
4	0.52	0.4	0.55	0.39
5	0.72	0.29	0.83	0.38
6	0.59	0.4	0.79	0.47
7	0.59	0.4	0.58	0.34

VITA

QINANG HU

Candidate for the Degree of

Doctor of Philosophy

Thesis: DIRECT THREE DIMENSIONAL OBSERVATION OF THE MICROSTRUCTURE AND CHEMISTRY OF C_3S

Major Field: Civil Engineering

Biographical:

Education:

Completed the requirements for the Doctor of Philosophy in Civil Engineering at Oklahoma State University, Stillwater, Oklahoma in December, 2015.

Completed the requirements for the Master of Science in Civil Engineering at Oklahoma State University, Stillwater, Oklahoma in 2011.

Completed the requirements for the Bachelor of Science Engineering Mechanics at China University of Mining and Technology (Beijing), Beijing, China, in 2009.

Experience:

Member of American Concrete Institute (ACI)
Member of American Ceramic Society (ACers)